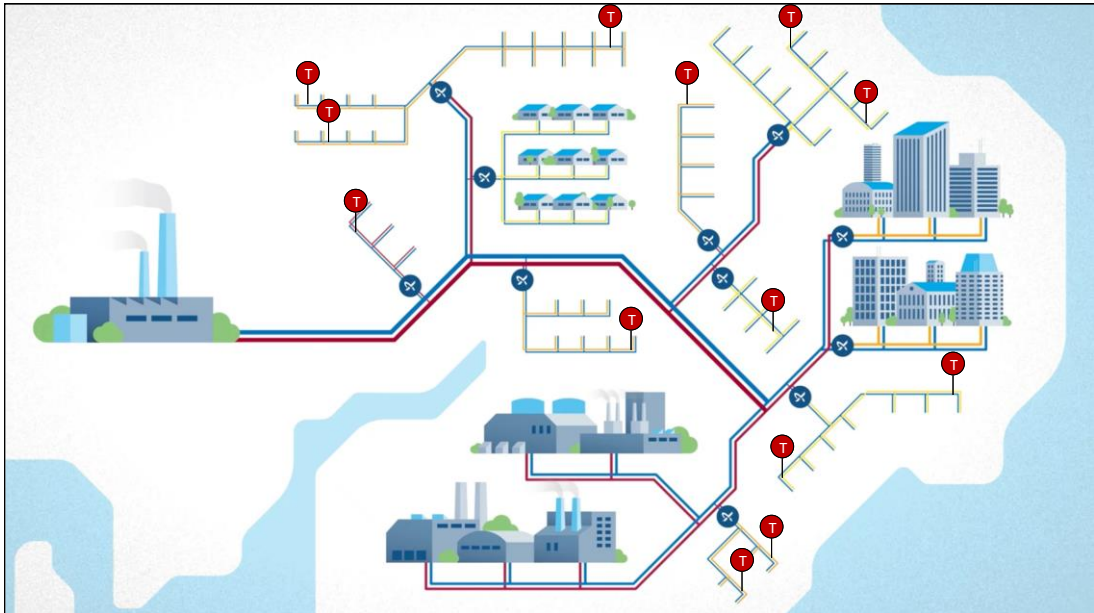

Design of Robust Temperature Control for Low Temperature Zones in District Heating Grids

- Master's Thesis -



Project Report
MCE4-1026

Aalborg University
Department of Energy Technology



AALBORG UNIVERSITY
STUDENT REPORT

Tenth Semester
Department of Energy Technology
Pontoppidanstræde 111
9220 Aalborg
<https://www.et.aau.dk/>

Title:

Design of Robust Temperature Control for Low Temperature Zones in District Heating Grids

Project:

Master's Thesis

Project Period:

From 01/02-2022 to 30/05-2022

Project Group:

MCE4-1026

Participants:

Ida Agerbo Rindom
Jacob Ørsnes Hvims

Supervisor:

Henrik Clemmensen Pedersen

Number of Pages: 116

Appendices: 12

Synopsis:

To improve the incorporation of renewable energy sources in the district heating grid, low temperature zones are utilized. However, in some low temperature zones, the distance to the temperature sensor causes a significant transport delay, resulting in decreased control performance. This study investigates how a robust temperature controller can be designed to reduce the impact of the transport delay and thereby improve the temperature tracking.

The report proposes three variations of a Smith Predictor Control scheme to compensate for the flow dependent transport delay. The delay compensation term used in the schemes show to be sensitive to change in the system dynamics. A Proportional Integral controller is designed to ensure robust stability despite parameter variations and seasonal changes. An uncertain plant model, which includes parameter variation for the pipe lengths and - diameter, is used in this context.

The proposed Smith Predictor Control schemes are compared to a classical control solution to verify if the temperature tracking performance has been improved when the system is exposed to temperature disturbances. Based on the simulation results it is concluded that the Smith Predictor Control schemes do not improve the temperature tracking performance as the compensation term in the control schemes cannot predict the disturbances. Therefore another solution is required to improve the temperature tracking.

Resumé

For bedre at kunne integrere grønne energikilder i fjernvarmenettet er det ønsket at sænke fremløbstemperaturen i fjernvarmenettet. For at sikre at forbrugernes varmebehov stadig kan opfyldes, er lavtemperaturzoner en essentiel del af overgangen til at kunne sænke fremløbstemperaturen. I nogle temperaturzoner kan afstanden fra blandingspunktet og hen til temperatursensoren dog medføre en betydelige transportforsinkelse af fremløbsvandet, hvilket har indvirkning på den kontrol løsning, der bruges til at styre fremløbstemperaturen i temperaturzonerne.

Formålet med denne rapport er derfor at undersøge, hvordan en regulatorstruktur kan blive designet, således at betydningen af afstanden hen til sensoren minimeres, og kontrolsystemet dermed bedre kan følge temperaturreferencen til trods for forstyrrelser i systemet. Derudover er det essentielt, at regulatorstrukturen er robust overfor parameter - og årstidsvariationer.

Rapporten foreslår tre variationer af en Smith Predictor Control struktur, som har til formål at kompensere for transportforsinkelsen ud til sensoren, og dermed gøre det muligt at designe en mere aggressiv regulator. En analyse af kompenseringsmekanismen i de tre Smith Predictor Control variationer viser, at deres evne til at kompensere for transportforsinkelsen er følsom overfor ændringer i systemets dynamiske adfærd. Regulatoren, som Smith Predictor Control strukturerne benytter sig af, er designet til sikre at kontrolsystemet er robust stabilt overfor parameter - og årstidsvariationer. Robustheden er analyseret ved brugen af en usikkerhedsmodel, som er designet for et sommer - og vinter scenarie, hvor længden og diameteren af rørstykkerne varieres.

De foreslåede Smith Predictor Control variationer sammenlignes med en klassisk regulatorstruktur for at vise, om de er bedre til at følge en konstant temperaturreference, når systemet udsættes for temperaturforstyrrelser. Baseret på simuleringresultaterne konkluderes det, at de undersøgte Smith Predictor Control strukturer ikke er i stand til at forbedre kontrolsystemets evne til at følge temperaturreferencen efter som, at kompenseringsmekanismen i Smith Predictor Control strukturerne ikke kan forudsige temperaturforstyrrelserne. Som følge af dette er det nødvendigt med en anden kontrolløsning til at mindske temperaturfejlen.

Preface

This report has been written by a group of 4th semester students from the Master of Science in Energy Engineering with specialisation in Mechatronic Control Engineering at Aalborg University. Information used in the report has been gathered from scientific articles, books, reports and other relevant sources. Analyses in the report have been conducted using MATLAB, Simulink, and Maple. Illustrations in the report have been made using diagrams.net.

The authors would like to thank Grundfos for giving the opportunity to collaborate on the Master's Thesis. A special thanks to Brian Kongsgaard Nielsen for providing us with information and guidance throughout the project.

Reader's Guide:

In the equations and in the text "." is used as a decimal separator. Literature citation is done following the Vancouver method, where the cite is referred to by a bracketed number [1], [2], [3] etc., and the literature is organised chronologically in reference to the literature's occurrence in the report.

Ida Agerbo Rindom

Jacob Ørsnes Hvims

By signing this document, each group member confirms that everyone has participated equally in the project work and that everyone are collectively responsible for the contents of the report.

Contents

Resumé	v
Preface	vii
Nomenclature	xi
1 Introduction	1
2 Problem Analysis	3
2.1 System Description	3
2.2 Control Problem	5
3 Problem Statement	7
4 District Heating Grid Model	9
4.1 Model Derivation	11
4.1.1 Temperature Determination	12
4.1.2 Volume Flow Determination	16
4.1.3 Pressure Determination	19
4.1.4 Pump Equations	19
4.2 Model Validation	20
5 Control Strategy Introduction	25
5.1 Test Scenarios	25
5.2 Benchmark	26
5.2.1 Nota Bene	27
6 Linear Model	29
6.1 System Model Simplification	29
6.2 Linear Model Derivation	31
6.3 Linear Model Investigation	33
6.4 Linear - and Nonlinear Model Comparison	35
7 Temperature Estimation	37
7.1 SPC Schemes Description	39
7.2 Estimation Results	43
8 Control Design	47
8.1 Uncertain Plant Model	47
8.2 Controller Design for $T_{4,10}$	50

8.3	Controller Design for $T_{4,1}$	54
9	Temperature Tracking Results	61
9.1	Result Explanation	62
9.2	Final Thoughts	68
10	Conclusion	69
	Bibliography	71
	Appendices:	
A	Efficiency Analysis	75
B	Determination of Flow Type	77
C	Model Parameters	79
D	Dynamic Model Equations	81
D.1	Control Volume Equations	82
E	Thermal Resistances	93
F	Volume Flow Gradient Derivation	97
G	Test Scenarios Parameter Choice	99
H	Linear Model Validation for the Summer Scenario	101
I	Filter Design	103
I.1	Filters for Simulation Model	103
J	Parameter Sensitivity Analysis	107
J.1	Pressure Influence	109
K	Weight Functions	111
L	Simulation Result Figures	113

Nomenclature

Greek Symbols:

β	Bulk modulus	[Pa]
Δ_I	Stable transfer function	[-]
λ	Friction coefficient	[-]
ν	Kinematic viscosity	$[\frac{m^2}{s}]$
ω	Frequency	[rad/s]
ω_c	cut-off frequency	[rad/s]
ω_I	Rational weight function	[-]
ω_p	Angular pump velocity	$[\frac{rad}{s}]$
Π	Set of possible perturbed plant models	[-]
ρ	Density	$[\frac{kg}{m^3}]$

Symbols:

A	State matrix	[-]
B	Input matrix	[-]
C	Output matrix	[-]
x	State vector	[-]
y	output vector	[-]
<i>A</i>	Cross-sectional area	[m ²]
<i>a</i>	Pump parameters	[-]
<i>c</i>	Velocity of pressure wave	[m/s]
<i>c_p</i>	Specific heat capacity	$[\frac{J}{kg \cdot K}]$
<i>D</i>	Diameter of casing	[m]
<i>d</i>	Hydraulic diameter	[m]
<i>f_{bp}</i>	Amount of bypass flow	[%]
<i>g</i>	Acceleration of gravity	$[\frac{m}{s^2}]$
<i>G(s)</i>	Transfer function	[-]
<i>H</i>	Head	[m]
<i>k</i>	Thermal conductivity	[W/(m · K)]
<i>K_I</i>	Integral gain	[-]
<i>K_P</i>	Proportional gain	[-]
<i>K_v</i>	Valve constant	[m ³ /(s · Pa)]
<i>L</i>	Kalman gain	[-]
<i>L</i>	Length	[m]
<i>l_I</i>	Relative uncertainty	[-]
<i>m</i>	Mass	[kg]
<i>n</i>	Number of houses	[-]
<i>p</i>	Pressure	[Pa]
<i>Q</i>	Volume flow	$[\frac{m^3}{s}]$

q	Heat flow	$[\frac{J}{s}]$
R	Heat transfer resistance	$[\frac{K}{W}]$
R	Weighting parameters	$[-]$
Re	Reynolds number	$[-]$
T	Complementary sensitivity function	$[-]$
T	Period time	$[s]$
T	Temperature	$[K]$
t	Time	$[s]$
t_d	Transport delay	$[s]$
u	Velocity	$[\frac{m}{s}]$
V	Volume	$[m^3]$
w	White noise	$[-]$
x_{valve}	Valve opening	$[-]$
z	Disturbance states	$[-]$
u	Input vector	$[-]$

Abbreviations:

BW	Bandwidth
CV	Control volume
GM	Gain margin
PM	Phase margin
SPC	Smith Predictor Control

Introduction 1

During the 20Th century the district heating system has gone through a big development. Having used steam as the heat carrier in the period 1880-1930 today's district heating systems now use pressurised water with temperatures below 100 °C to supply households and industries with energy used for space heating and heating of domestic water [1]. Today's district heating systems still utilize fossil fuels to heat the supply water, however the incorporation of renewable energy systems, heat storage, and usage of industry surplus energy is improving and becoming a bigger part of the district heating systems [1]. I.e. numbers from the Energy Agency in Denmark shows that 72 % of the danish district heating was supplied by renewable energy sources in 2020 [2].

To meet the goal of the European Union to become carbon neutral by 2050 [3], it is of high relevance that today's district heating systems are further improved [1]. In order to do so it is essential to lower the supply water temperature. Besides having the effect of decreasing the thermal losses in the pipelines, lower supply temperatures will improve the integration between the district heating grid and renewable energy sources like solar thermal heat and geothermal heat as well as industrial waste heat [4].

However, lowering the supply water temperature requires that the consumer's needs still can be fulfilled. As a result it is important to prepare the industry and residential areas for the temperature change as older heat exchange systems may require a higher temperature to fulfill the demand. For the district heating grid to meet the future demands of lower grid temperatures, low temperature zones are established where the supply water temperature is actively lowered using a pump system. The low temperature zones makes it possible to ensure that a specific area can handle lower grid temperatures in the future [5].

However, maintaining the temperature for the low temperature zones at a fixed temperature can be challenging due to system delay time and disturbances. As a consequence the temperature may oscillate undesirably which stresses the pipes [5]. As a result, the purpose of this report is to investigate a way to improve the control performance to allow for a more steady temperature tracking.

Problem Analysis 2

In this chapter the low temperature zone in the district heating system, used for analysis throughout the rapport, is specified and the control problem is described.

2.1 System Description

A district heating grid consists of a large pipe network which connects a centralised power plant or a number of distributed heating units with the industry and residential areas [1]. An example of a district heating grid is visualized in Figure 2.1.

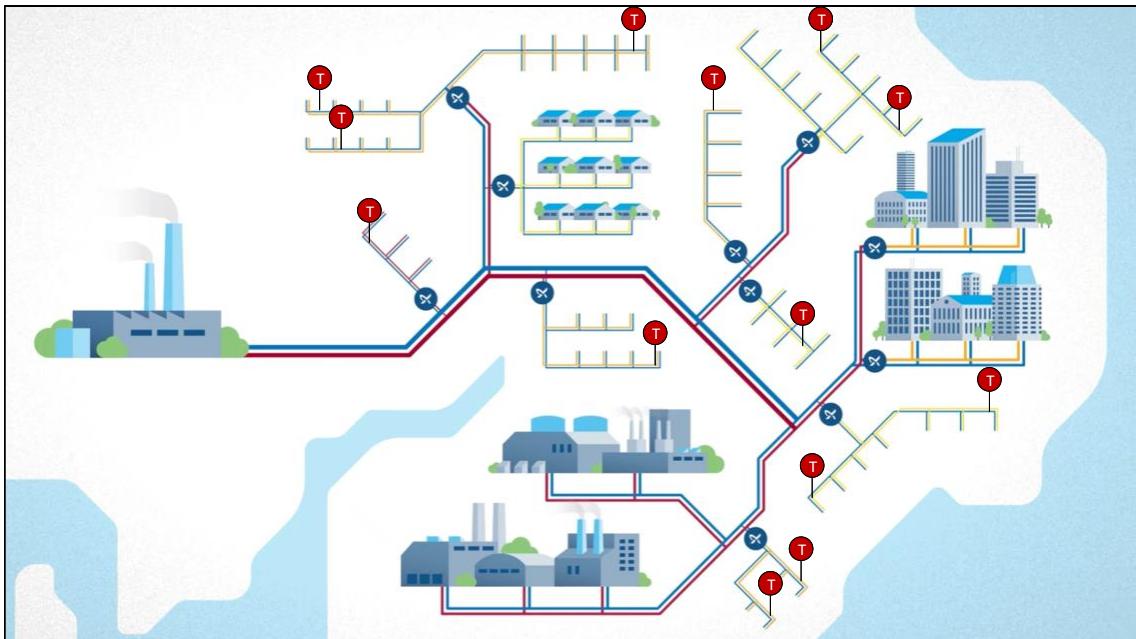


Figure 2.1. Illustration of a district heating grid [5]

In the figure it is visualized how the power plant to the left produces and distributes warm district heating water to a large consumer area consisting of both industrial buildings, high-rise buildings, and households of different sizes. The cooled district heating water is next sent back to the power plant where it is reheated and distributed to the consumers again. In the figure it is seen that the pipelines in some areas are illustrated with a yellow - and blue pipeline instead of a red - and

blue pipeline. A yellow line indicates that the water temperature has been lowered for the specific area. As a result these areas are referred to as low temperature zones and, as described in the introduction, these zones are introduced to convert the district heating grid to lower temperatures [5]. The temperature lowering is achieved by using a pump which is shown in the figure by a blue circle marked with a Grundfos logo. The low temperature zones are an important element in the conversion of the district heating grid to lower temperatures, as a low temperature zone makes it possible to isolate a specific area from the rest of the grid. It is then possible to make changes to specific houses and buildings in the area and then use the pump solution to verify if a lower temperature is sufficient to fulfill the consumer demand. This way it is possible to do all the necessary testing before a potential temperature lowering is made at the district heating plant.

Grid Simplification

A low temperature zone will in most cases consist of a multi-branched network with a high number of consumers. To simplify the network of the consumers and the further analysis, all consumers in a given area are combined into one total consumer. The simplified district heating grid of a low temperature zone is represented in Figure 2.2.

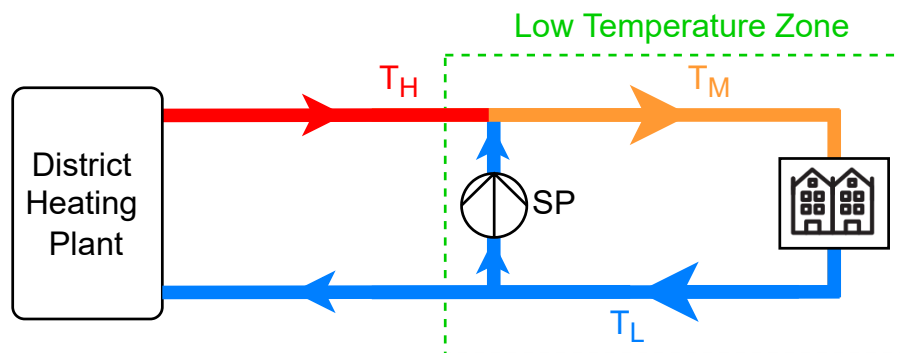


Figure 2.2. Simplified district heating grid with a low temperature zone

The simplified grid illustrates the high temperature district heating water, T_H , coming from the power plant. A shunt pump, SP , which in fact is a centrifugal pump, connects the low temperature return water, T_L , with the high temperature supply water. This means it is possible to lower the temperature of the supply water by actively controlling the velocity of the shunt pump. The mixed district heating water, T_M , is sent to the consumers, in the figure visualized by two houses, where energy from the district heating water is transferred to the consumers' domestic water and through the radiators to be used for space heating. Some of the low temperature water is then returned to be recycled by the shunt pump and the other part is transported back to the power plant where the water is reheated.

2.2 Control Problem

Grundfos has developed a control solution such that the water temperature T_M can be adjusted by controlling the volume flow through the shunt pump. The closed loop control solution utilizes information from a temperature sensor which is placed after the mixing point. As illustrated in Figure 2.3 the mixing point defines the point where the high temperature water is combined with the low temperature water. As a result a uniform distribution of the resulting temperature is obtained some distance after this point.

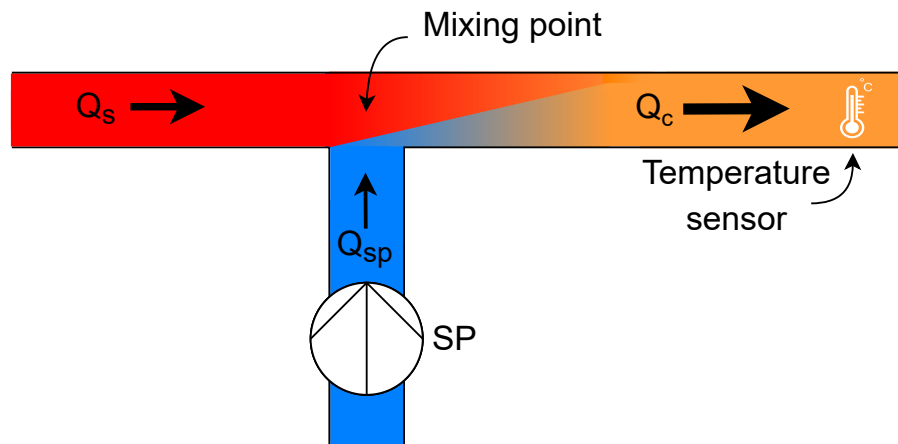


Figure 2.3. Close up of simplified grid visualizing mixing point and temperature sensor, where Q_s , Q_c , and Q_{sp} is supply flow, consumer flow, and flow through the shunt pump, respectively

The distance from the mixing point to the temperature sensor can vary and this gives rise to a transport delay, which is dependent on the fluid velocity and the distance. In some cases the temperature sensor is placed around 30 m from the mixing point [5], thus the transport delay is equal to 300 s if a volume flow of 0.1 m/s is considered, which can occur in summer periods [5].

In addition to the transport delay, disturbances of different kinds are also present in the system. I.e. the shunt pump may experience a fluctuating load pressure, defined as the pressure difference across the shunt pump, which will affect the volume flow through the shunt pump. Furthermore, the water temperature before the mixing point as well as the water temperature in the return pipe may vary throughout the day, causing the mixed water temperature to be disturbed. The combination of transport delay and disturbances of different kinds makes it difficult to obtain good temperature tracking performance, as the transport delay naturally limits the controller performance and hence reduces the systems ability to reject disturbances.

An obvious solution to help the problem of long delay time is to place the temperature sensor closer to the mixing point. However, it will not be ideal to place the sensor directly in the mixing point, as the measurement will be poor due to an

unequal distribution of the low and high temperature water. As a result the sensor should be placed after the mixing point where a good trade off between transport delay and measurement quality is achieved. However, unless there is an easy way to mount the temperature sensor closer to the mixing point, i.e. if there is a well near the mixing point which gives access to the pipe with the mixed temperature water, then it may not always be affordable to move the sensor [5]. Other times a customer who wants Grundfos' pump solution may have strict requirements of where the temperature sensor should be placed and if the shunt pump has to be placed some distance away from the sensor due to certain circumstances, then the transport delay must be accepted. The fact is that a significant transport delay cannot always be avoided and therefore it is desired from Grundfos' point of view to have a control solution that can ensure accurate temperature control nonetheless [5].

On the basis of this, the purpose of this report is to investigate how a control structure can be designed to compensate for the varying transport delay and ensure a low temperature tracking error of the mixed water temperature despite seasonal variations and temperature - and pressure disturbances. The developed control strategy will be compared to a classical feedback control solution developed in the report.

Problem Statement 3

Based on the introduction and the problem analysis the following problem statement is formulated:

How can a robust temperature control solution be designed to reduce the impact of the transport delay and allow for better disturbance rejection and hence obtain a more steady supply water temperature in a low temperature zone, despite seasonal changes and system variations?

To answer the problem statement following steps will be taken:

- Derive a nonlinear model of the simplified district heating grid
- Validate the nonlinear model by simulation
- Develop a robust classical feedback control solution
- Develop a robust control solution which reduces the impact of the transport delay
- Comparison of tracking performance between the classical control solution and the new designed control structure

District Heating Grid

Model 4

In this chapter a mathematical model of the simplified district heating grid will be derived, and the model behavior is presented using the simulation results.

The purpose of the mathematical model is to describe how the pressure differs across the shunt pump, and how the temperature changes at the location of the temperature sensor when the volume flows and inlet temperatures to the mixing point change. It is relevant to model the pressure difference across the shunt pump, as the volume flow through the pump is affected by this. As a result a change in the load pressure will act as a flow disturbance which can affect the control performance.

To formulate the mathematical model the simplified district heating grid has been divided into ten control volumes. This division is visualized in Figure 4.1.

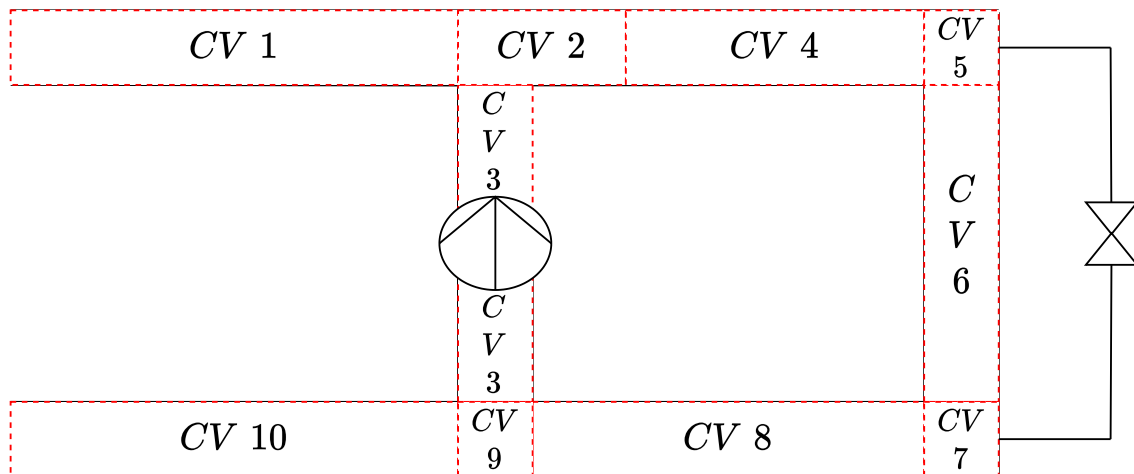


Figure 4.1. System grid visualizing the span of each control volume

As it appears each control volume represents a specific area in the grid. More specifically it applies that:

- Control volume 1 consists of the supply pipe from the district heating power plant to the mixing point.
- Control volume 2 consists of the pipe section spanning from the mixing point to the placement of the temperature sensor.

- Control volume 3 includes the shunt pump and the pipe section between the return pipe and the supply pipe.
- Control volume 4 consists of the pipe section going from the temperature sensor to the consumers.
- Control volume 5 represents the endpoint of the supply pipe (at the last consumer) where a small percentage of the volume flow is led through a bypass valve to mix with the return volume flow at control volume 7.
- Control volume 6 consists of the consumers, combined as one total consumer, where energy from the district heating water is transferred to the domestic water of the consumers and used for house heating via the radiators.
- Control volume 7 represents the starting point of the return pipe (at the last consumer) where the bypass flow is mixed with cooled water from the consumers.
- Control volume 8 consists of the pipe section going from the consumers to the separation point where one part of the return water is led back to the power plant and the other part is led through the shunt pump.
- Control volume 9 consists of the small volume where the return water is separated.
- Control Volume 10 consists of the pipe section going from the separation point and back to the district heating power plant.

Bypass Section

As mentioned a bypass section is included in the district heating grid. In a physical district heating grid this bypass section is placed after the last consumer at the end of the road. Having the bypass section allows the water to keep circulating in an area despite a low consumer demand. Being able to keep water flowing in the pipes assures that warm district heating water relatively fast can be delivered to the consumer [5]. Besides the practical advantage of having a bypass flow, the bypass flow will inevitably affect the temperature of the return water as water returning from the consumers will be mixed directly with supply water.

The bypass section has been included in the system model to analyse if the introduction of a low temperature zone can help to decrease the thermal losses in the grid and thereby improve the energy efficiency. This analysis can be found in Appendix A. From the analysis it is concluded that the interplay between the shunt pump and the bypass flow cannot help increase the energy efficiency.

4.1 Model Derivation

For the derivation of the model itself the grid diagram presented in Figure 4.2 will be used. Despite the different visualization of the control volumes, each control volume still represents the same area as it appears in Figure 4.1.

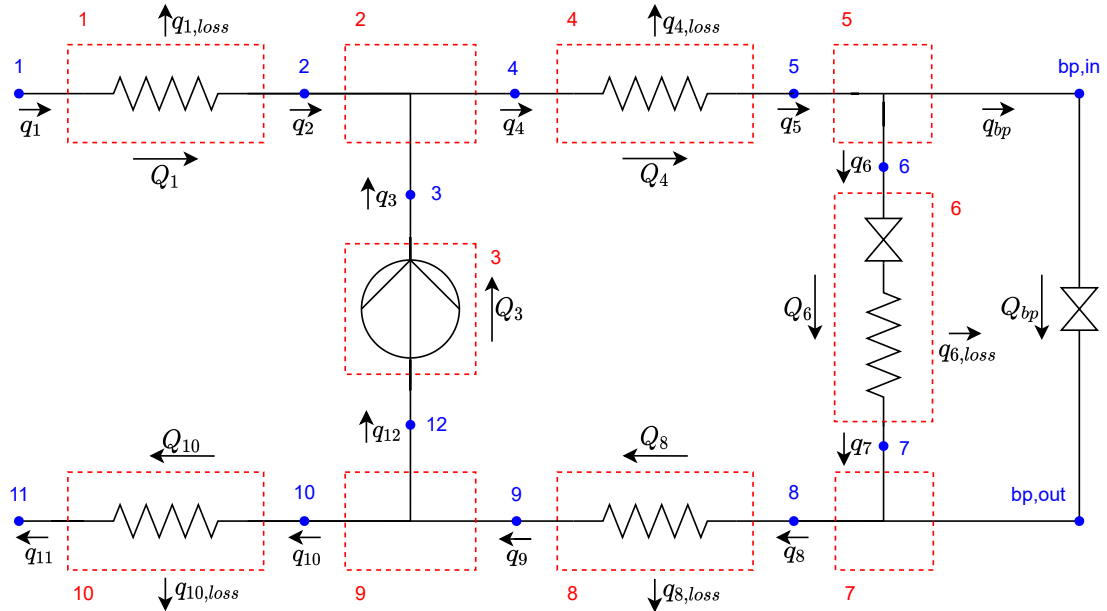


Figure 4.2. System grid with nodes and control volumes indicated

Between each control volume a node has been defined. The model will seek to describe the pressure and temperature in each node. For some of the control volumes a symbol of a resistor is included. The resistor indicates that heat is lost to the surroundings.

To describe the pressure and temperature in every node, equations for pressure change, volume flow change, and heat flow have been derived for each control volume. In this section a general form of the used equations is presented, where the subscripts i and j are used to denote nodes and control volumes respectively. The complete system model with all equations for each control volume can be found in Appendix D.

The boundary conditions for the system are pressure p_1 , p_{11} , supply temperature T_1 , ground temperature T_g , ambient temperature at consumer T_a and reference room temperature for radiator thermostat T_r^* .

Assumption

The assumptions used when deriving the system model are:

- As the temperature gradually decreases along a physical pipe, the average temperature between the inlet and the outlet of a control volume is used to determine heat loss to the surroundings for that specific control volume.
- The flow in the pipes is considered to be turbulent as calculations show that for a pipe diameter of 0.06 m the flow velocity will have to be below 0.05 m/s before the flow is close to become laminar. As such low velocities are not expected in the district heating grid the volume flow is considered turbulent at all times. Calculations that support this statement can be found in Appendix B
- Due to the small size of control volume 2, 3, 5, 7, and 9 heat loss to the surroundings are considered negligible. For the same reason the pressure loss is considered negligible across control volume 2, 5, 7, and 9.

4.1.1 Temperature Determination

To determine the temperature in node 2-12 the principle of energy conservation is considered. From this principle it follows that heat flow added to a control volume must be equal to heat flow leaving the control volume either through the outlet of the control volume or through losses [6].

$$\sum q_{j,in} = \sum q_{j,out} \quad (4.1)$$

- $q_{j,in}$ - Heat flow into control volume j [W]
 $q_{j,out}$ - Heat flow out of control volume j [W]

The specific equation describing the energy conservation will vary for the different types of control volumes. I.e. the equation for control volume 1 and 2 will be different as control volume 2 has multiple inlets and no heat loss to the surroundings. Control volume 1, 4, 8, and 10 are identical and the equation to describe the conservation of energy for these control volumes are given by Equation (4.2).

$$q_i = q_{i+1} + q_{j,loss} + q_{j,w} \quad (4.2)$$

Equation (4.3) - (4.6) are used to describe each term respectively. Note, when applying the equations below, and equations described in Subsection 4.1.2 and 4.1.3, for a specific control volume, it applies that $i = j$.

$$q_i = Q_j \cdot \rho_w \cdot c_{p,w} \cdot T_i \quad (4.3)$$

$$q_{i+1} = Q_j \cdot \rho_w \cdot c_{p,w} \cdot T_{i+1} \quad (4.4)$$

$$q_{j,loss} = \frac{1}{R_j} \cdot \left(\frac{T_i + T_{i+1}}{2} - T_g \right) \quad (4.5)$$

$$q_{j,w} = c_{p,w} \cdot m_j \cdot \dot{T}_{i+1} \quad (4.6)$$

q_i	-	Heat flow in node i [W]
$q_{j,loss}$	-	Heat flow loss in control volume j [W]
Q_j	-	Volume flow through control volume j [m ³ /s]
T_i	-	Temperature in node i [K]
T_g	-	Ground temperature [K]
ρ_w	-	Density of water [kg/m ³]
c_w	-	Specific heat capacity of water [J/(K · kg)]
R_j	-	Pipe thermal resistance in control volume j [K/W]
m_j	-	Mass of water in control volume j [kg]
\dot{T}_i	-	Temperature gradient in node i [K]

Inserting Equation (4.3) - (4.6) into (4.2) makes it possible to isolate \dot{T}_{i+1} and determine T_{i+1} through integration. The equation to describe the conservation of energy for control volume 6 is similar to Equation (4.2). However the loss term denoted $q_{6,loss}$, representing the consumer demand, utilizes another thermal resistance and ambient temperature. This is further described in subsection "Room Temperature".

Temperature T_4

To describe the temperature at the temperature sensor, T_4 , a steady state heat flow equation in combination with a transport delay will be utilized. This is done to obtain a more accurate description of this temperature, as a change at the mixing point will not cause T_4 to change immediately due to the travel time of the water.

To derive an expression for T_4 Equation (4.7) is used to describe the energy of conservation for control volume 2.

$$q_2 + q_3 = q_4 \quad (4.7)$$

where

$$q_2 = Q_1 \cdot \rho_w \cdot c_{p,w} \cdot T_2 \quad (4.8)$$

$$q_3 = Q_3 \cdot \rho_w \cdot c_{p,w} \cdot T_3 \quad (4.9)$$

$$q_4 = Q_4 \cdot \rho_w \cdot c_{p,w} \cdot T_4 \quad (4.10)$$

Isolating for T_4 results in Equation (4.11).

$$T_4 = \frac{Q_1 \cdot \rho_w \cdot c_{p,w} \cdot T_2 + Q_3 \cdot \rho_w \cdot c_{p,w} \cdot T_3}{Q_4 \cdot \rho_w \cdot c_{p,w}} \quad (4.11)$$

In order to delay the temperature T_4 a flow dependent transport delay is introduced. For this purpose Simulink's "Variable Transport Delay" block is used. To describe the variable transport delay, t_d , Equation (4.12) is used.

$$t_d = \frac{L_2 \cdot A_2}{Q_4} - t_{tr} \quad (4.12)$$

- t_d - Delay time [s]
- L_2 - Length of pipe in control volume 2 [m]
- A_2 - Cross-sectional area of the pipe in control volume 2 [m²]
- t_{tr} - Transition time [s]

Here the transition time is a number defined to take into account that T_4 will change ahead of the calculated transport delay time, as it is expected that water with a higher temperature will affect water with a lower temperature as the water is flowing. In addition to this a low pass filter is used to smooth out the transition further and to avoid the peak seen in Figure 4.4. The peak arises from Q_3 that can change instantaneously and cause the heat flow, q_3 , to spike.

Figure 4.3 illustrates how the outlet temperature from Equation (4.11) is implemented and delayed using a combination of a variable transport delay and a low pass filter. Note, onwards in the report, when denoting T_4 , this will refer to the temperature value after the low pass filter.

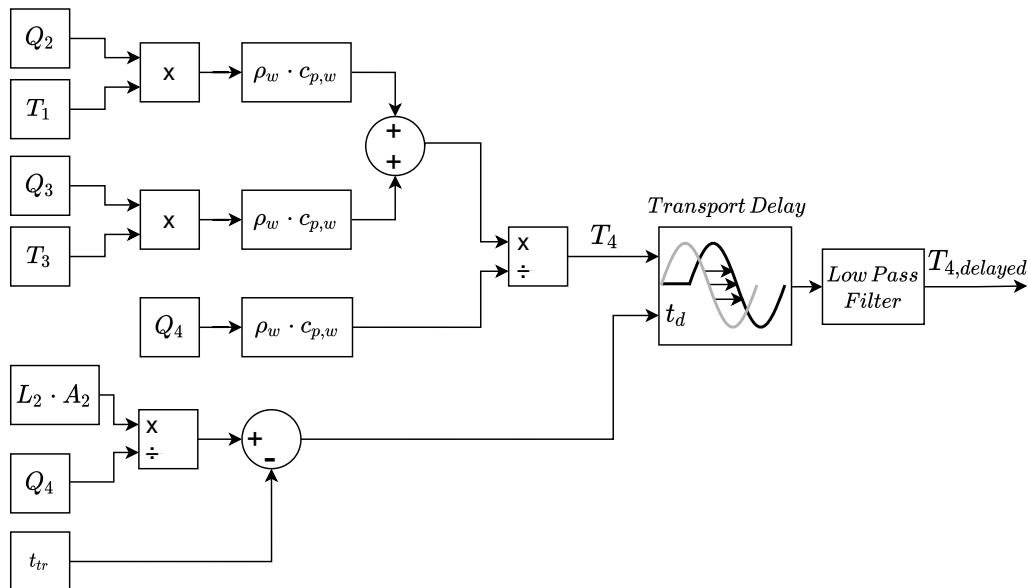


Figure 4.3. Calculation of T_4 with transport delay and low pass filter

Figure 4.4 illustrates the effect of the transition time and low pass filter. A step input has been given to the pump at $t = 20$ s. From the figure it is apparent how the transport delay is decreased using the transition time and how the dynamic is smoothed out using the low pass filter. Without the filter the temperature is still slowly decreasing which is solely due to the dynamic behavior of the volume flow.

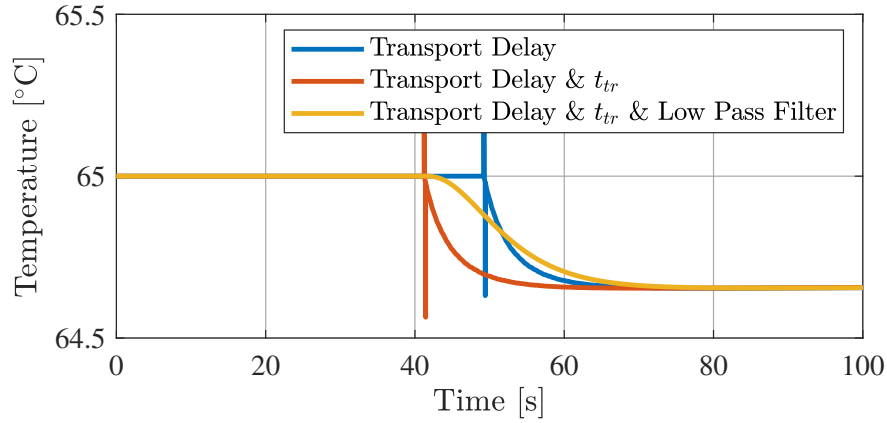


Figure 4.4. Influence of transition time and low-pass filter on dynamic behavior of T_4

Room Temperature

To obtain the temperature of the water leaving the consumer, T_7 , it is necessary to know the room temperature at the consumer, T_r . To determine T_r the principle of energy conservation is used to define an equation for the heat entering through a radiator and leaving the consumer through the walls in the house. Figure 4.5 depicts the energy flow for the consumer house.

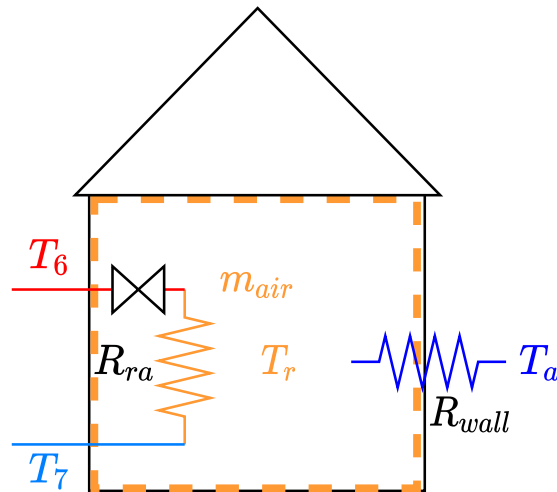


Figure 4.5. Consumer house with constants and variables denoted

For the consumer house the conservation of energy states:

$$q_{6,loss} = q_r + q_a \quad (4.13)$$

where it applies that:

$$q_{6,loss} = \frac{1}{R_{ra}} \cdot \left(\frac{T_6 + T_7}{2} - T_r \right) \quad (4.14)$$

$$q_r = c_{p,air} \cdot m_{air} \cdot \dot{T}_r \quad (4.15)$$

$$q_a = \frac{1}{R_{wall}} \cdot (T_r - T_a) \quad (4.16)$$

R_{ra}	-	Thermal resistance of radiator [K/W]
T_r	-	Room temperature [K]
q_r	-	Heat flow into the consumer house [W]
q_a	-	Heat flow to the surroundings [W]
$c_{p,air}$	-	Specific heat coefficient of air [J/(kg · K)]
m_{air}	-	Mass of air in the consumer house [kg]
\dot{T}_r	-	Room temperature gradient [K/s]
R_{wall}	-	Thermal resistance of house wall [K/W]

The room temperature T_r is determined by inserting Equation (4.14) - (4.16) into (4.13) and isolating for T_r through integration of \dot{T}_r . A description of how the thermal resistances R_{ra} and R_{wall} as well as pipe thermal resistances, R_j , are determined, can be found in Appendix E. Furthermore, the equations derived to describe the outlet temperature of the remaining control volumes can be found in Appendix D.

4.1.2 Volume Flow Determination

For control volumes 1, 4, 6, 8, and 10 the volume flow gradient is determined using Newton's Second Law. As the pressure remains unchanged through control volume 2, 5, 7, and 9 no change in volume flow is occurring and the volume flow gradient equals zero. For control volume 3 the volume flow is determined by the shunt pump which is described in Subsection 4.1.4.

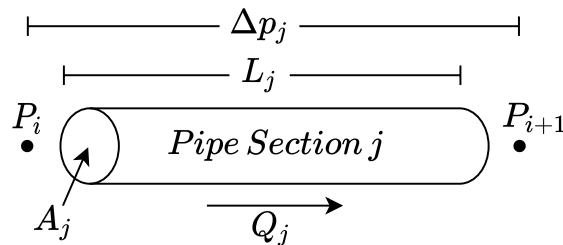


Figure 4.6. Pipe section j with constants and variables denoted

Using Newton's Second Law it is possible to describe the volume flow change across a pipe section j , visualized in Figure 4.6, as presented in Equation (4.17) [7]. The

derivation of Equation (4.17) can be found in Appendix F.

$$\dot{Q}_j = \frac{(p_i - p_{i+1} - \Delta p_j) \cdot A_j}{L_j \cdot \rho_w} \quad (4.17)$$

- \dot{Q}_j - Volume flow gradient through control volume j [m^3/s^2]
- p_i - Pressure in node i [Pa]
- Δp_j - Pressure loss across control volume j [Pa]
- A_j - Cross-sectional area of control volume j [m^2]
- L_j - Length of pipe in control volume j [m]

Knowing the volume flow gradient it is possible to determine the volume flow through integration of the gradient. The volume flow will be used to determine the pressure in each node.

For control volume 1, 4, 6, 8, and 10 the pressure loss Δp is determined by Equation (4.18).

$$\Delta p_j = \lambda \cdot \frac{L_j}{d_j} \cdot \rho_w \cdot \frac{u_j^2}{2} \quad \text{where} \quad u_j = \frac{Q_j}{A_j} \quad (4.18)$$

From Appendix B it is proved that it is reasonable to consider the volume flow to be turbulent at all times. As a result the friction coefficient λ is determined as:

$$\lambda = 0.3164 \cdot \frac{1}{Re^{\frac{1}{4}}} \quad \text{where} \quad Re = \frac{d_j \cdot u_j}{\nu} \quad (4.19)$$

- λ - Friction coefficient [-]
- Re - Reynolds number [-]
- u_j - Mean water velocity in control volume j [m/s]
- ν - Kinematic viscosity of water at 55 °C [m^2/s]

A kinematic viscosity of water at 55 °C is chosen as the temperature across the system is expected to span between 30-80 °C.

For control volume 6 the pressure loss is defined based on the pressure loss across the valve which is placed right before control volume 6 as depicted in Figure 4.7.

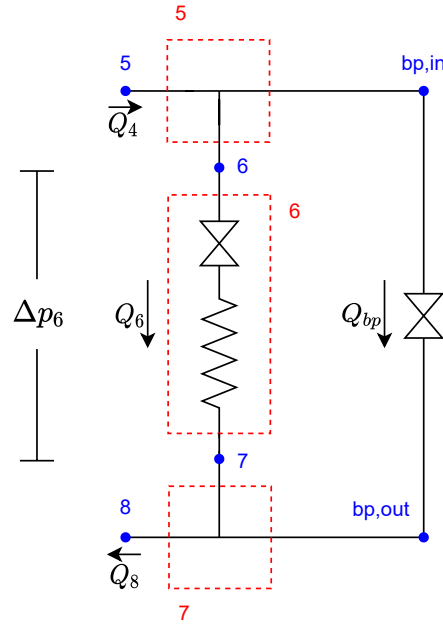


Figure 4.7. Control volume 5, 6, and 7

To determine the pressure loss across the valve, the orifice equation as well as an equation for the valve opening will be used, and these are presented in Equation (4.20) and (4.21).

$$Q_6 = K_v \cdot x_{valve} \cdot \sqrt{\Delta p_6} \quad (4.20)$$

$$x_{valve} = G_{PI} \cdot (T_r^* - T_r) \quad (4.21)$$

- K_v - Valve constant [$\text{m}^3/(\text{s} \cdot \text{Pa})$]
- x_{valve} - Valve opening [-]
- T_r^* - Room temperature reference [$^{\circ}\text{C}$]

The valve opening stated in Equation (4.21) is determined based on a reference room temperature T_r^* and the actual room temperature together with a Proportional Integral (PI) controller. The PI controller serves to emulate a person manually changing the valve opening such the correct room temperature is obtained. The PI controller is tuned to give a non oscillating response. Inserting the expression for the valve opening into Equation (4.20) it is possible to determine the pressure loss by isolating for Δp_6 .

4.1.3 Pressure Determination

To determine the pressure in node 2-10 and node 12 the continuity equations is used as presented in Equation (4.22).

$$\dot{p}_i = \frac{\beta}{\sum \frac{V_{j,in}}{2} + \sum \frac{V_{j,out}}{2}} \cdot (\sum Q_{j,in} - \sum Q_{j,out}) \quad (4.22)$$

- \dot{p}_i - Pressure gradient in node i [Pa/s]
- β - Bulk modulus of water [Pa]
- V_j - Volume of control volume j [m³]
- $Q_{j,in}$ - Volume flow into control volume j [m³/s]
- $Q_{j,out}$ - Volume flow out of control volume j [m³/s]

Through integration of the pressure gradient the pressure is obtained for the given node. As control volume 2, 5, 7, and 9 are considered loss free pressure 2, 3, and 4 are identical, pressure 5, 6, and bp, in are identical, pressure 7, 8, and bp, out are identical, and pressure 9, 10, and 12 are identical.

4.1.4 Pump Equations

The pump used to regulate the temperature in the low temperature zone is a centrifugal pump. The volume flow delivered by a centrifugal pump can be derived from the equation describing the head of the pump. Head is defined as the height to which the pump can raise a fluid if a vertical pipe is connected at the discharge zone. For a centrifugal pump the head can be given by Equation (4.23) [8].

$$H = -a_{h2} \cdot Q_{sp}^2 + a_{h1} \cdot Q_{sp} \cdot \omega_p + a_{h0} \cdot \omega_p^2 \quad (4.23)$$

- H - Head [m]
- Q_{sp} - Volume flow through centrifugal pump [m³/s]
- ω_{sp} - Angular velocity of centrifugal pump [rad/s]
- a_{h0} - Coefficient dependent on pump characteristic [s²/m]
- a_{h1} - Coefficient dependent on pump characteristic [s²/m³]
- a_{h2} - Coefficient dependent on pump characteristic [s²/m⁸]

The head of a pump is also given by equation (4.24)[8].

$$H = \frac{\Delta p_{sp}}{\rho_w \cdot g} \quad \text{where} \quad \Delta p_{sp} = p_{out} - p_{in} = p_3 - p_{12} \quad (4.24)$$

- Δp_{sp} - Pressure difference across centrifugal pump [Pa]
- p_{out} - Centrifugal pump outlet pressure [Pa]
- p_{in} - Centrifugal pump inlet pressure [Pa]
- g - Acceleration of gravity [m/s²]

The volume flow delivered by the centrifugal pump is determined by substituting Equation (4.24) into Equation (4.23) and isolating for Q_{sp} . As a result Equation (4.25) is obtained.

$$Q_3 = Q_{sp} = \frac{a_{h1} \cdot \omega_{sp} + \sqrt{4 \cdot a_{h0} \cdot a_{h2} \cdot \omega_{sp}^2 + a_{h1}^2 \cdot \omega_{sp}^2 - 4 \cdot \frac{p_3 - p_{12}}{\rho_w \cdot g} \cdot a_{h2}}}{2 \cdot a_{h2}} \quad (4.25)$$

This concludes the derivation of the dynamical model of the district heating grid. All system equations and model constants can be found in Appendix D and C respectively.

4.2 Model Validation

In this section the model simulation results are showcased to verify that the model behavior and dynamics are sensible. The model will not be compared to real measurement data as this is not practical. A real consumer area is more complicated than the district heating grid analysed in this report and as a result there will be dynamical behaviors that are difficult to incorporate into the system model. Therefore the essence of this section is to verify that the modelled system behaves as expected. As the unmodelled dynamics are essential for the further analysis, these will be included later as disturbances based on data from a real low temperature zone.

For the model simulation the boundary conditions, consisting of the pressure at node 1 and 11, the supply temperature, the ambient temperature in the ground and outside the houses, and the bypass flow, are given, and a room temperature reference is defined.

$$\begin{aligned} p_1 &= 3.5[\text{bar}] & p_{11} &= 1.5[\text{bar}] & T_1 &= 80[^\circ\text{C}] & T_g &= 3.6[^\circ\text{C}] \\ T_a &= 1.6[^\circ\text{C}] & T_r^* &= 20[^\circ\text{C}] & Q_{bp} &= 1/20 \cdot Q_4[\text{L/s}] \end{aligned}$$

For the PI controller used to control the valve opening the gains are:

$$K_P = 5 \cdot 10^{-3} \qquad K_I = 8.9 \cdot 10^{-6}$$

The model is initialized with steady state considerations for the temperature, volume flow, and pressure throughout the circuit. The result of the simulation is shown in Figure 4.8 for temperature, pressure, and volume flow. Here it should be noted that the volume flow through control volume 4 and 8 are equal, and the volume flow through control volume 1 and 10 are equal.

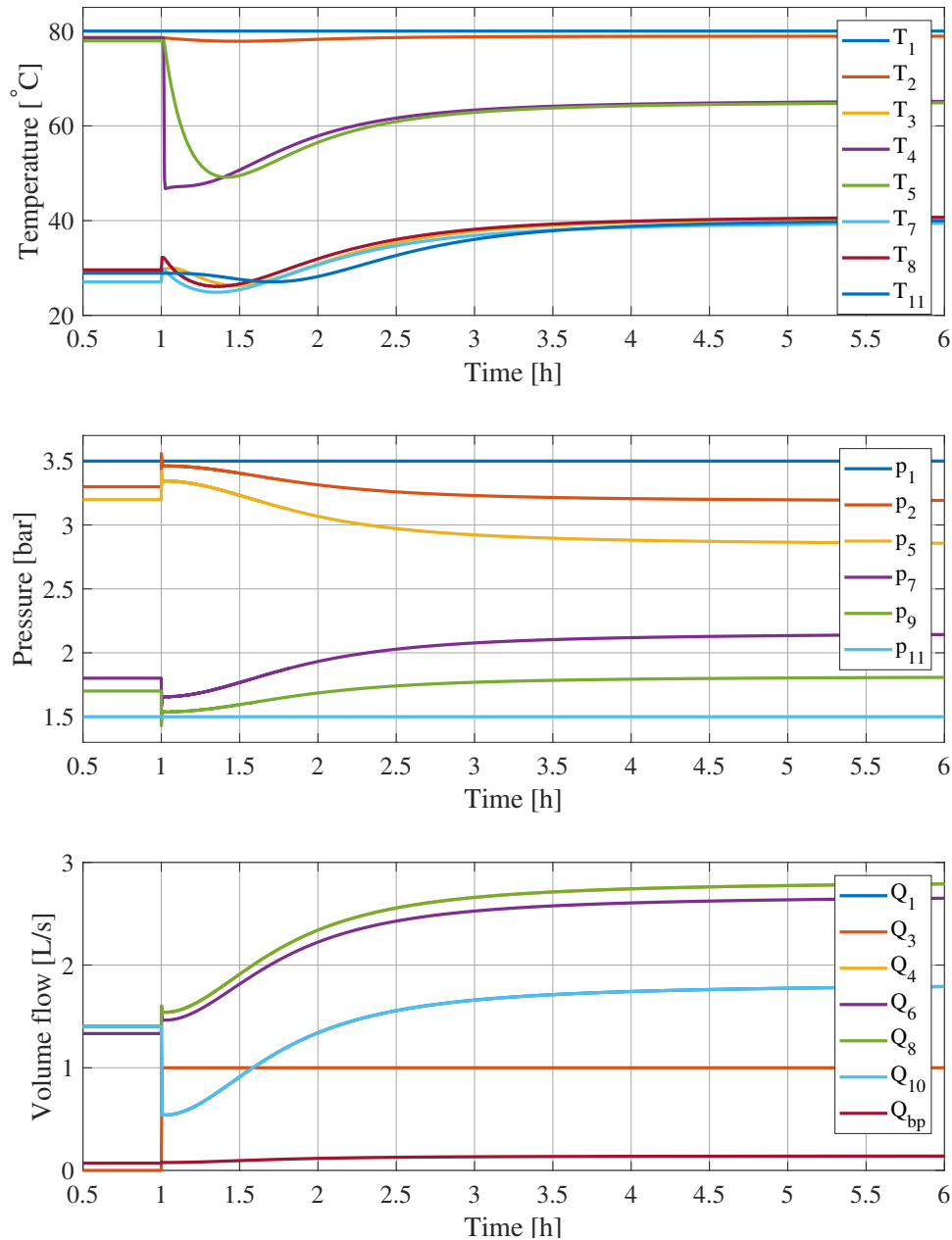


Figure 4.8. Temperature, pressure, volume flow, and heat flow throughout the system

From time $t=0$ to $t=1$ h, Figure 4.8 shows the circuit with the shunt pump initialized to deliver a volume flow equal to 1×10^{-7} L/s ≈ 0 . Here it can be observed that the temperature and pressure drop throughout the circuit due to heat loss in the pipes and pressure loss in the fluid lines and over the radiator valve respectively.

After time $t = 1$ h the shunt pump is set to deliver a volume flow of 1.0 L/s. Due to the transport delay, the temperature T_4 is not immediately decreasing when the shunt pump is stepped and the supply water is mixed with the return water. This is visualized in Figure 4.9.

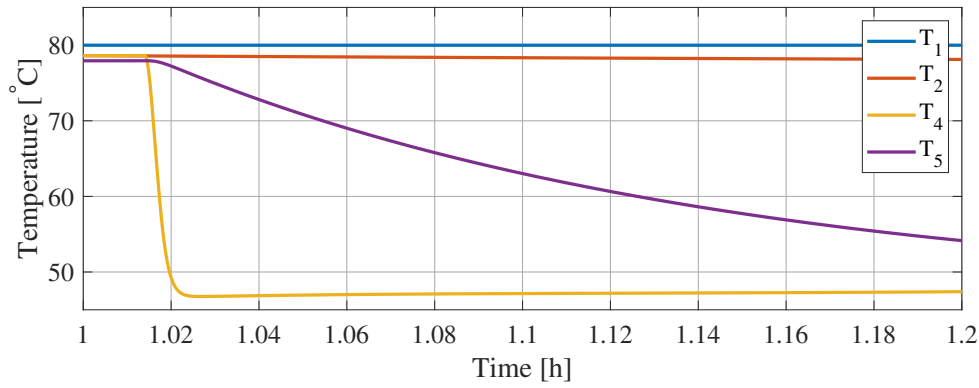


Figure 4.9. Zoom on temperature response of T_4

In Figure 4.10 heat flow at the consumer, room temperature and valve dynamic are presented.

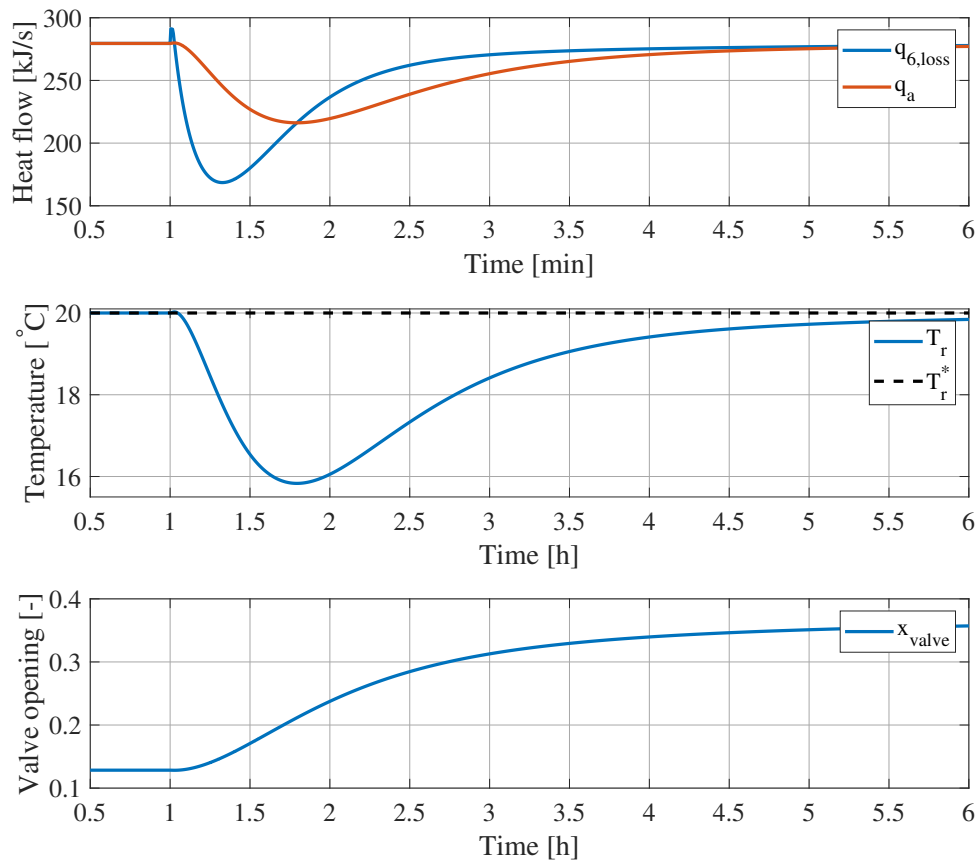


Figure 4.10. Heat flow in and out of the lumped house, room temperature, and radiator valve opening

Due to a decrease in T_5 the heat transfer through the radiator to the consumer, $q_{6,loss}$, decreases. This results in the room temperature T_r decreasing as the heat leaving the consumer through the house wall, q_a , is greater than the heat entering the consumer house through the radiator. To maintain the reference room temperature the valve

opening is increased using the PI controller which increases the volume flow through the consumer. This has the desired effect of increasing the room temperature to the reference of 20 °C. In Figure 4.8 it is visualized how the volume flow along the grid increases due to the change in valve opening.

In Figure 4.11 the heat loss throughout the grid is shown and in Figure 4.12 the volume flows and temperatures around the consumer and bypass are visualized.

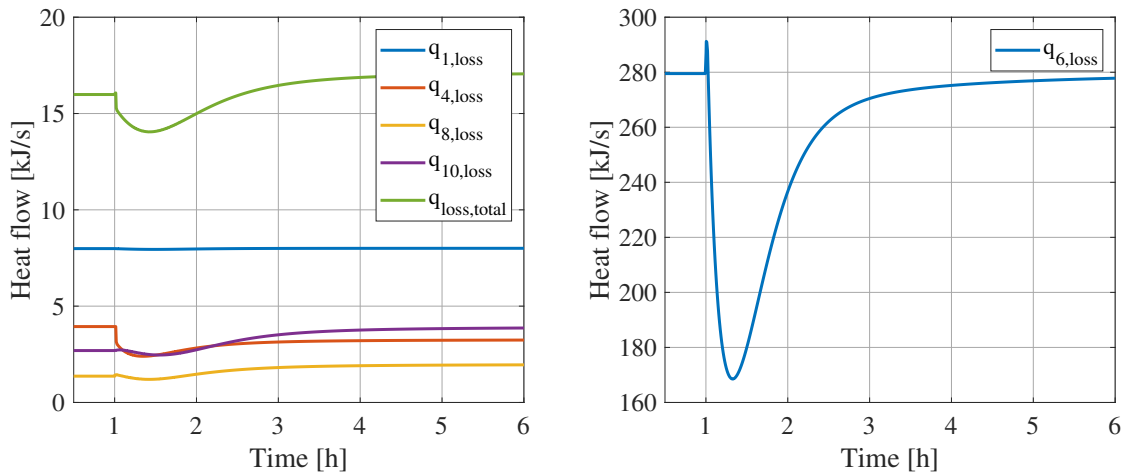
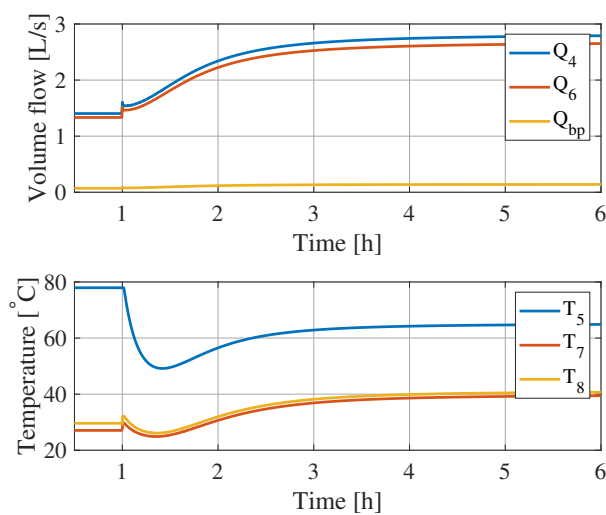
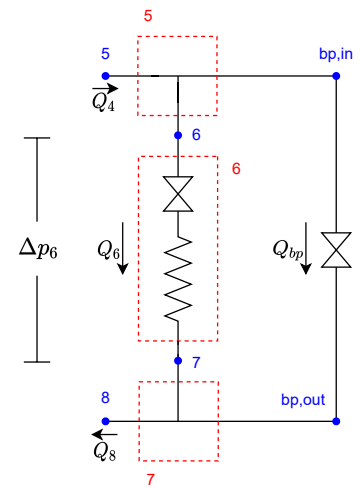


Figure 4.11. Heat loss in control volume 1, 4, 8, and 10, and heat flow out to the consumer in control volume 6



(a) Temperature and volume flow



(b) Sketch of CV6 and bypass valve

Figure 4.12. Control volume 6 and bypass valve

From Figure 4.11 it is seen how the thermal heat loss in control volume 4 has decreased due to a lower temperature in node 4 and 5 after stepping the shunt pump. However this decrease in heat loss is not high enough to lower the total thermal heat loss. This is a consequence of the temperature T_8 increasing as seen in

Figure 4.12 and hence increasing the thermal heat loss along control volume 8 and 10.

From the simulation results it is seen that the system behaves realistically and shows the expected tendencies such as temperature and pressure drop as well as energy and mass being conserved. Therefore it is concluded that the system model can be utilized as a representative model for a low temperature zone in a district heating grid. However, the specific parameters used for the model can vary for different low temperature zones of the district heating grid, and a sensitivity analysis needs to be performed in a later chapter to gain knowledge on how the model parameters influence the system dynamics.

Control Strategy

Introduction

5

In this chapter the control problem is shortly restated and a control structure to improve the disturbance rejection of the system is proposed. The test scenarios which the designed control solutions will be tested for are stated and lastly the control benchmark is defined.

Relying solely on the temperature measurement after the mixing point to generate an error signal for the temperature controller means that the controller itself must be designed very conservatively to avoid instability occurring in the case of a significant transport delay. However utilizing a conservative controller decreases the control system's ability to reject disturbances. The states which acts as a disturbance to the control system are the pump load pressure and the supply - and return temperature T_2 and T_9 . Each state variation will impact the mixing temperature and hence affect the temperature at the temperature sensor, T_4 . It is undesired to have the water temperature after the mixing point oscillate unnecessarily as it causes wear on the pipes. As a result, it is relevant to optimize the control structure such a better disturbance rejection can be achieved, thus reducing the pipe wear and ensuring a more steady heat supply to the consumers.

To accomplish an improved disturbance rejection this report proposes variances of a Smith Predictor Control (SPC) structure. As will be explained in more detail in Chapter 7, SPC makes it possible to compensate for the transport delay and hereby increase the bandwidth of the system to potentially allow for better temperature tracking. The SPC schemes will be based on information from a linear system model. Therefore a linear model will be derived in Chapter 6.

5.1 Test Scenarios

It is desired for the control solution to ensure stability in different seasons and under varying district heating grid configurations. Especially change in season has a large impact on the system dynamics. During summer the fluid velocity can be around 0.1 m/s whereas the velocity may be around 1 m/s in winter periods. This will affect the transport delay significantly and therefore it is relevant to investigate how the performance differs for different scenarios. Two test scenarios have been defined.

Test scenario 1 represents a winter day in January and test scenario 2 represents a summer day in July. Table 5.1 shows the boundary conditions for each scenario. The explanation for the choice of the boundary condition values can be found in Appendix G.

Table 5.1. Boundary conditions for test scenario 1 and - 2

	Test Scenario 1 "Winter day"	Test Scenario 2 "Summer day"
Parameter Description	Value	Value
Air temperature [T_{air}]	1.6 °C	16.9 °C
Ground temperature [T_g]	3.6 °C	15.1 °C
Room temperature reference [T_{ref}]	20 °C	20 °C
Supply temperature [T_1]	80 °C	70 °C
Supply pressure [p_1]	3.5 bar	3 bar
Return pressure [p_{11}]	1.5 bar	1.5 bar
Consumer inlet temperature [T_6]	65 °C	55 °C
Consumer outlet temperature [T_7]	40 °C	35 °C
Consumer power [$q_{6,loss}$]	279.51 kW	34.94 kW
Fluid velocity [u]	1 m/s	0.16 m/s
Bypass flow [f_{bp}]	5%	5%

5.2 Benchmark

In order to verify the potential temperature tracking improvement using the proposed control structure, a benchmark has been defined. For the benchmark, the temperature T_4 is controlled using a classical feedback loop where T_4 is fed back in order to generate an error signal for a PI controller to react on. The benchmark will consist of the tracking result for the *standard* winter scenario and the *upper worst case* summer scenario, which are defined in Chapter 8. Figure 5.1 shows the tracking result for the *standard* winter scenario, where the temperature reference is held constant at 65 °C. Variations in T_2 and T_9 , obtained from measurements in a low temperature zone [9], have been added to the simulation to show how the control system's tracking ability is affected by temperature disturbances.

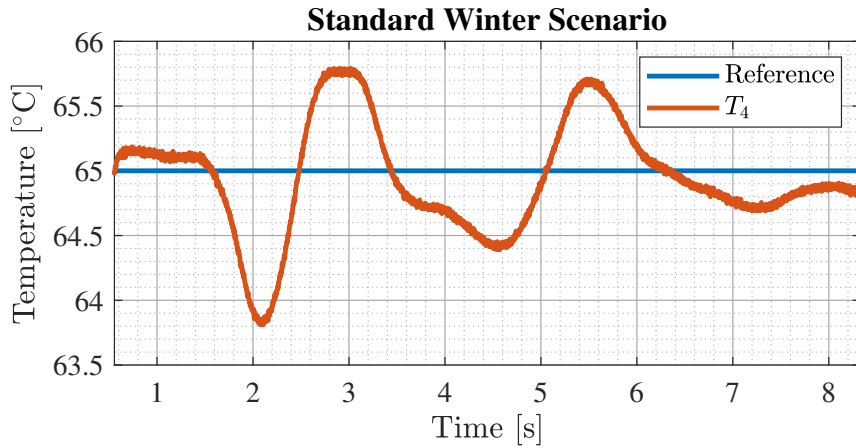


Figure 5.1. Benchmark for the *standard* winter scenario

From the simulation results, it follows that the RMS error equals 0.414°C and the maximum absolute error equals 1.190°C . For the *upper worst case* summer scenario the RMS error equals 0.109°C and the maximum absolute error equals 0.387°C . This sets the benchmark for the proposed control structure.

5.2.1 Nota Bene

As described, only temperature variations have been added to the simulation model for the benchmark. This will also be the case when the final simulation results are shown in Chapter 8. As mentioned, variations in load pressure act as a disturbance to T_4 through the volume flow. Therefore it is relevant to include load pressure variations in the simulation model as well. This has also been the intention, however, it was discovered late in the project work that the implementation of the pressure disturbance on p_2 and p_9 had a canceling effect in the simulation model, making the pressure disturbance insignificant. Implementing the disturbances correctly results in the simulation result seen in 5.2.

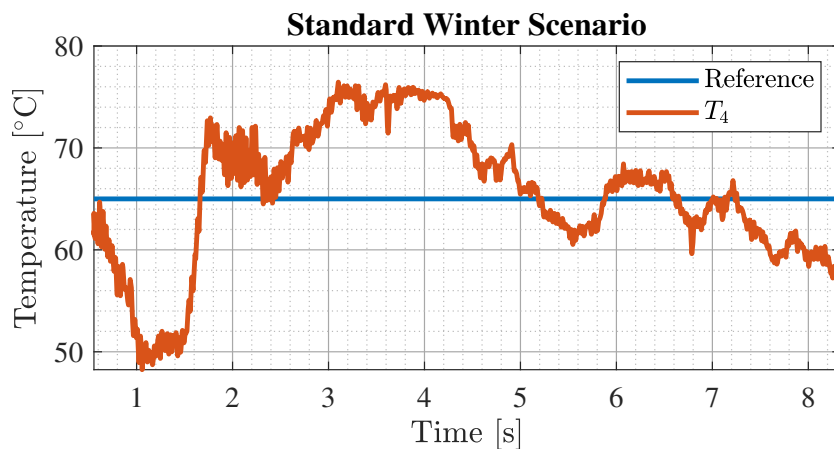


Figure 5.2. System tracking performance with pressure distances implemented for standard winter scenario

From the figure it is apparent how the pressure disturbances have made a significant impact on the tracking performance. The control performance using a classical control loop is not acceptable and therefore it is relevant to suppress the negative effect of the pressure variations. Methods do exist to accomplish this and Grundfos' uses one in their own control solution. In order to complete the design of a new control structure it is relevant to include the pressure variation compensation technique as part of the control structure. However due to lack of time when the mistake was discovered, the inclusion of the compensation technique is avoided and the pressure disturbances is neglected for the further analysis. Nonetheless it is believed that the further analysis is highly relevant as it investigate the possibilities of improving the disturbance rejection further if compensation for the pressure disturbances has already been done.

Linear Model 6

In this chapter, the nonlinear model will be simplified before deriving a linear model for the system. The frequency response of the derived linear model is presented, and the dynamical behavior of linear model is compared to the nonlinear model.

6.1 System Model Simplification

The nonlinear system model is simplified to reduce the complexity of the linear system. The simplification is made by combining control volume 4, 5, 6, 7, and 8 into one control volume, and neglecting the bypass valve. Constructing one control volume is assumed valid as the volume flow in the control volumes have similar dynamical behaviour. Neglecting the bypass valve is acceptable as the bypass volume flow is small relative to the volume flow in control volume 4 and 8. The simplified system model is visualized in Figure 6.1, where the volume flow through the combined control volume is denoted Q_c for *consumer* flow.

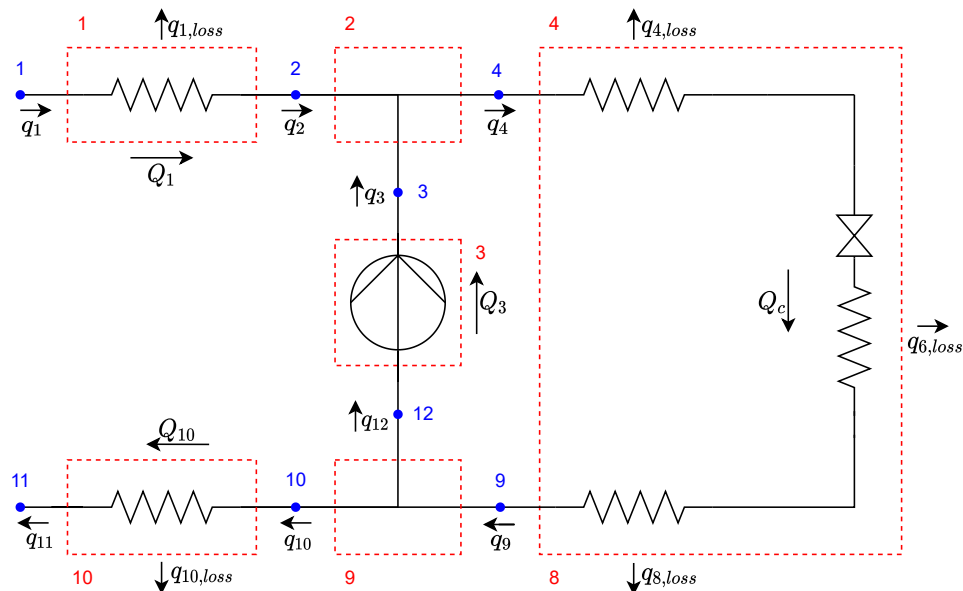


Figure 6.1. Simplified system model

For the linear model, the effect of the transport delay will be obtained by dividing

control volume 2 into multiple control volumes, as illustrated in Figure 6.2. The temperature at the outlet of each minor control volumes will be described with the differential equation stated in Equation 6.1.

$$\dot{T}_{4,i} = \frac{1}{C_{p,w} \cdot \frac{m_{CV2}}{n}} \cdot (q_{4,i-1} - q_{4,i}) \quad (6.1)$$

Here i is the index for a specific minor control volume, and n is the number of minor control volumes, which control volume 2 has been split into.

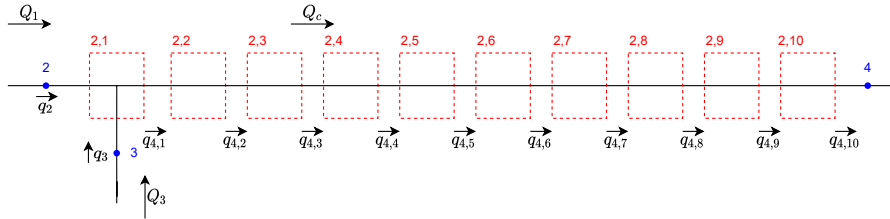


Figure 6.2. Control volume 2 divided into multiple control volumes

To determine the number of control volumes which control volume 2 needs to be split up into, the step response is shown in Figure 6.3 for one, three, five, seven, and ten minor control volumes, and compared to the ideal transport delay. In the figure, the ideal transport delay is marked with the black line, and the step response will approach this line as the number of control volumes increases.

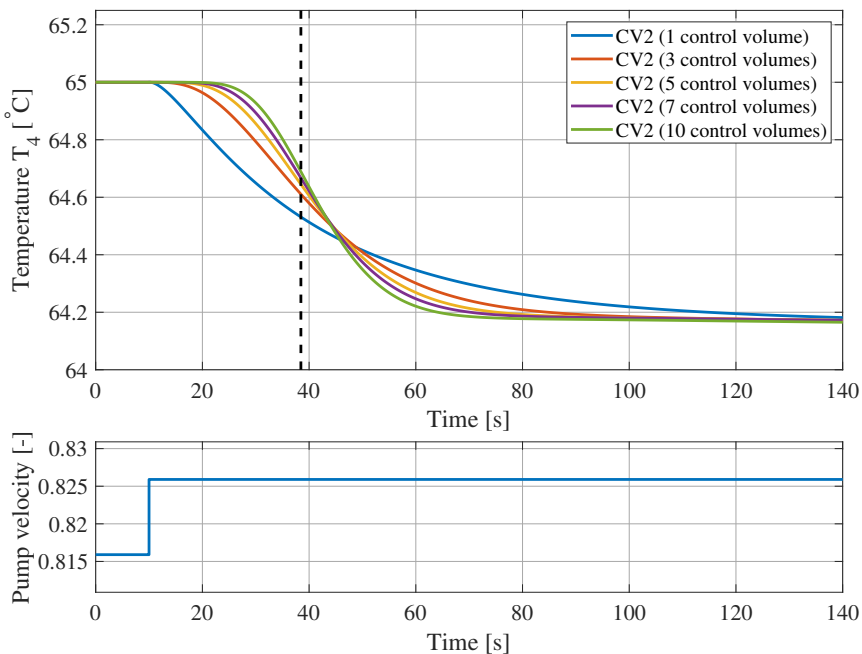


Figure 6.3. Step response when control volume 2 divided into multiple control volumes. The black dotted line indicates the transport delay, $d_{2,t} = L_2 \cdot A_2 / Q_c$

Based on the figure, it is seen that the impact of extra control volume decrease as the number of minor control volumes increases. Therefore it is assumed that ten control volumes for control volume 2 is a sufficient approximation to describe the transport delay for the temperature at node 4.

6.2 Linear Model Derivation

A linear model is derived by linearizing the equations of the simplified nonlinear system. Below the dynamic equations for the simplified system are defined.

Volume Flow

The volume flow equations are described in Section 4.1.2, and for the simplified model they are presented as:

$$\begin{aligned}\dot{Q}_1 &= \frac{A_1}{L_1 \cdot \rho_w} \cdot (p_1 - p_2 - \Delta p_1(Q_1)) \\ &= f_1(p_2, Q_1)\end{aligned}\tag{6.2}$$

$$\begin{aligned}\dot{Q}_c &= \frac{A_4}{(L_4 + L_6 + L_8) \cdot \rho_w} \cdot (p_2 - p_9 - \Delta p_6(Q_c) - \Delta p_4(Q_c) - \Delta p_8(Q_c)) \\ &= f_2(p_2, p_9, Q_c)\end{aligned}\tag{6.3}$$

$$\begin{aligned}\dot{Q}_{10} &= \frac{A_{10}}{L_{10} \cdot \rho_w} \cdot (p_9 - p_{11} - \Delta p_{10}(Q_{10})) \\ &= f_3(p_9, Q_{10})\end{aligned}\tag{6.4}$$

Pressure

For the simplified system model, the pressure p_2 and p_9 are described as:

$$\begin{aligned}\dot{p}_2 &= \frac{\beta}{\frac{V_{CV1}}{2} + V_{CV2} + \frac{V_{CV4}}{2}} \cdot (Q_1 + Q_3(p_2, p_9, \omega_{sp}) - Q_c) \\ &= f_4(Q_1, Q_c, \omega_{sp}, p_2, p_9)\end{aligned}\tag{6.5}$$

$$\begin{aligned}\dot{p}_9 &= \frac{\beta}{\frac{V_{CV8}}{2} + \frac{V_{CV10}}{2}} \cdot (Q_c - Q_3(p_2, p_9, \omega_{sp}) - Q_{10}) \\ &= f_5(Q_{10}, Q_c, \omega_{sp}, p_2, p_9)\end{aligned}\tag{6.6}$$

Temperature

In the simplified model, the temperatures of interest are described with differential equations as:

$$\begin{aligned}\dot{T}_2 &= \frac{1}{c_{p,w} \cdot m_{CV1}} \cdot \left(q_1(Q_1) - q_{1,loss}(T_2) - q_2(Q_1, T_2) \right) \\ &= f_6(Q_1, T_2)\end{aligned}\quad (6.7)$$

$$\begin{aligned}\dot{T}_3 &= \frac{1}{c_{p,w} \cdot m_{CV3}} \cdot \left(q_{12}(p_2, p_9, \omega_{sp}, T_9) - q_3(p_2, p_9, \omega_{sp}, T_3) \right) \\ &= f_7(p_2, p_9, \omega_{sp}, T_3, T_9)\end{aligned}\quad (6.8)$$

$$\begin{aligned}\dot{T}_{4,1} &= \frac{1}{c_{p,w} \cdot \frac{m_{CV2}}{10}} \cdot \left(q_2(Q_1, T_2) + q_3(p_2, p_9, \omega_{sp}, T_3) - q_{4,1}(Q_c, T_{4,1}) \right) \\ &= f_8(Q_1, Q_c, \omega_{sp}, p_2, p_9, T_2, T_{4,1}, T_3)\end{aligned}\quad (6.9)$$

$$\begin{aligned}\dot{T}_{4,i} &= \frac{1}{c_{p,w} \cdot \frac{m_{CV2}}{10}} \cdot \left(q_{4,i-1}(Q_c, T_{4,i-1}) - q_{4,i}(Q_c, T_{4,i}) \right) \\ &= f_9(Q_c, T_{4,i-1}, T_{4,i})\end{aligned}\quad (6.10)$$

$$\begin{aligned}\dot{T}_9 &= \frac{1}{c_{p,w} \cdot (m_{CV4} + m_{CV6} + m_{CV8})} \cdot \left(q_{4,10}(Q_c, T_{4,10}) - q_9(Q_c, T_9) - q_{loss}(T_{4,10}, T_9) \right) \\ &= f_{10}(Q_c, T_{4,10}, T_9)\end{aligned}\quad (6.11)$$

for $i = [2..10]$. The heat loss in the combined control volume used for Equation (6.11), denoted q_{loss} , is the sum of the heat loss $q_{4,loss}$, $q_{6,loss}$, and $q_{8,loss}$.

It applies that the nonlinear dynamic equations presented above can be described in a general form as:

$$\dot{\mathbf{x}}(t) = \mathbf{f}(\mathbf{x}(t), u(t)) \quad (6.12)$$

$$\mathbf{y}(t) = \mathbf{h}(\mathbf{x}(t), u(t)) \quad (6.13)$$

where $\mathbf{x}(t)$ is the state vector presented in Equation (6.14), $u(t)$ is the input vector ($u(t) = [\omega_{sp}]$), and $\mathbf{y}(t)$ is the output vector.

$$\mathbf{x}(t) = \begin{bmatrix} Q_1 & Q_c & Q_{10} & p_2 & p_9 & T_2 & T_3 & T_{4,1} & T_{4,2} & T_{4,3} & \dots \\ \dots & T_{4,4} & T_{4,5} & T_{4,6} & T_{4,6} & T_{4,7} & T_{4,8} & T_{4,9} & T_{4,10} & T_9 \end{bmatrix} \quad (6.14)$$

A linear state space model is obtained by finding the Jacobian matrix of $\mathbf{f}(\mathbf{x}(t), u(t))$ with respect to $\mathbf{x}(t)$ and $u(t)$ at the equilibrium point, where $\dot{\mathbf{x}}(t) = \mathbf{f}(\mathbf{x}^*, u^*) = 0$.

This results in the matrices \mathbf{A} and \mathbf{B} as written in Equation (6.15) and (6.16).

$$\mathbf{A} = \left. \frac{\partial \mathbf{f}(\mathbf{x}(t), u(t))}{\partial \mathbf{x}(t)} \right|_{\mathbf{x}^*, u^*} \quad (6.15)$$

$$\mathbf{B} = \left. \frac{\partial \mathbf{f}(\mathbf{x}(t), u(t))}{\partial u(t)} \right|_{\mathbf{x}^*, u^*} \quad (6.16)$$

In the same manner, the Jacobian matrix of $\mathbf{h}(\mathbf{x}(t), u(t))$ is used to find the matrices \mathbf{C} and \mathbf{D} as:

$$\mathbf{C} = \left. \frac{\partial \mathbf{h}(\mathbf{x}(t), u(t))}{\partial \mathbf{x}(t)} \right|_{\mathbf{x}^*, u^*} \quad (6.17)$$

$$\mathbf{D} = \left. \frac{\partial \mathbf{h}(\mathbf{x}(t), u(t))}{\partial u(t)} \right|_{\mathbf{x}^*, u^*} \quad (6.18)$$

where all the entries in the matrix \mathbf{D} are zero, and is therefore removed. Thus the linear model can be presented as:

$$\dot{\mathbf{x}}(t) = \mathbf{A} \cdot \mathbf{x}(t) + \mathbf{B} \cdot u(t) \quad (6.19)$$

$$\mathbf{y}(t) = \mathbf{C} \cdot \mathbf{x}(t) \quad (6.20)$$

6.3 Linear Model Investigation

The linear model is evaluated at a linearization point, also denoted the equilibrium point, where all the derivatives are zero.

$$\dot{Q}_1 = \dot{Q}_c = \dot{Q}_{10} = \dot{p}_2 = \dot{p}_9 = \dot{T}_2 = \dot{T}_3 = \dot{T}_{4,i} = \dot{T}_9 = 0$$

Based on the boundary conditions, which are p_1 , p_{11} , T_g , T_a , f_{bp} , T_1 , T_4 , and T_r , the equilibrium point can be calculated with the nonlinear equations presented in Equation (6.2) to (6.11). The boundary conditions are based on the two test scenarios, a winter day and a summer day, which are described in Chapter 5. The Bode diagram of the temperature $T_{4,1}$ and $T_{4,10}$ for the *standard* winter - and summer scenarios are shown in Figure 6.4, for where it can be seen that the test scenarios have a significant influence on the system gain and phase. The increased gain and earlier phase drop for the summer scenario is especially caused by the lower fluid velocity which is a result of the lower consumer demand. Based on the volume flow in the equilibrium point, the resultant transport delay can be calculated with Equation (4.12) to 29.36 s and 172.51 s for the *standard* winter - and summer scenario respectively.

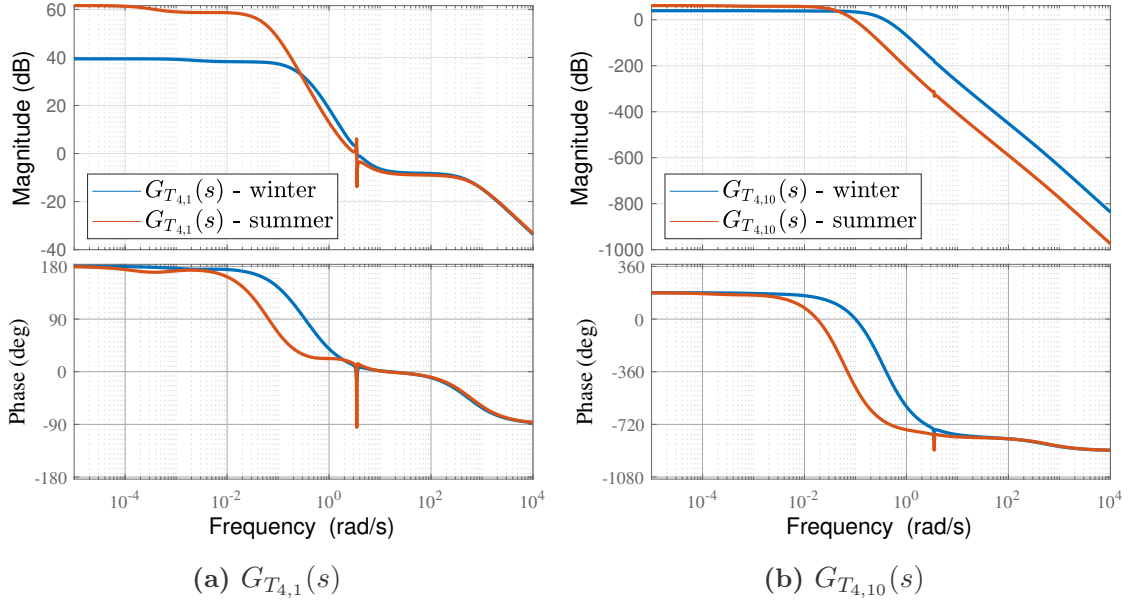


Figure 6.4. Bode diagram for $G_{T_{4,1}}(s)$ and $G_{T_{4,10}}(s)$ in test scenario 1 and 2

From Figure 6.4 it is seen that the phase starts in 180 deg, which indicates that the system has a sign shift. As a result a positive change in the pump velocity will yield a negative change in the output temperature.

In Figure 6.4a it can be seen that a spike occurs at approximately 3.5 rad/s. The spike is most likely a consequence of the pressure dynamic, as this frequency corresponds to that of a pressure wave traveling back and forth in the pipeline. To illustrate this, the following calculation of a pressure wave is made:

$$c = \sqrt{\frac{\beta}{\rho_w}} \approx 1536 \text{ [m/s]} \quad (6.21)$$

$$T = \frac{2 \cdot L}{c} \approx 2 \text{ [s]} \quad (6.22)$$

$$\omega = \frac{1}{T} \cdot 2 \cdot \pi \approx 3.14 \text{ [rad/s]} \quad (6.23)$$

Here c is the velocity of the pressure wave given as the speed of sound in a fluid and T is the round trip time, describing the time it takes for a pressure wave to travel back and forth [7]. Using the sum of the pipe section lengths, it is seen that the frequency for the pressure wave and the spike seen in the Bode diagram are approximately the same.

6.4 Linear - and Nonlinear Model Comparison

The designed linear model is compared to the nonlinear model in Figure 6.5 for the winter scenario to validate that the linear simplified model is a representative simplification of the nonlinear model. A similar comparison between the linear - and nonlinear model for the summer scenario can be found in Appendix H.

For the comparisons it should be noted that the equilibrium point for the linear - and nonlinear model is not exactly the same, due to the simplification of the model equations. For the winter scenario this means the offset in the pressure p_2 is 1.1×10^3 Pa and the offset in volume flow Q_c is -58×10^{-3} L/s. Therefore, the linear - and nonlinear model are set to start at the equilibrium point of the nonlinear model in order to compare the dynamic response when the pump velocity is stepped.

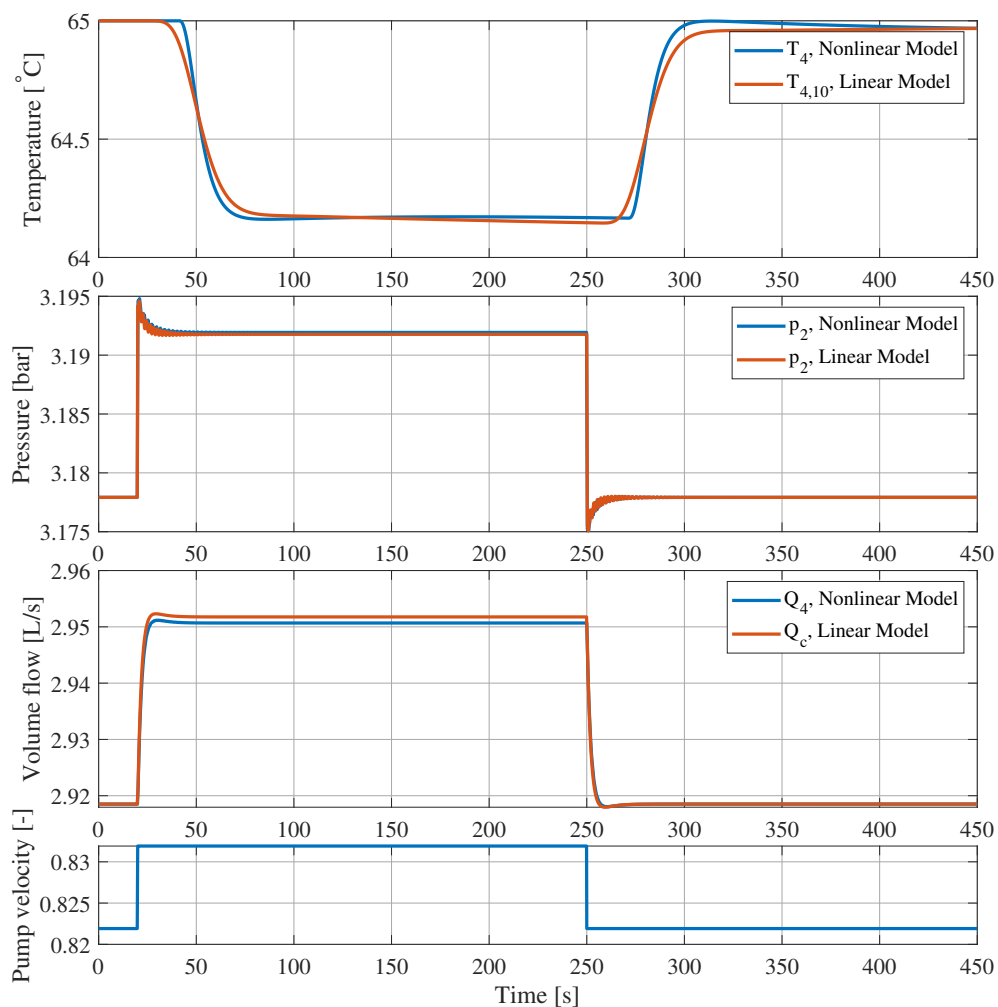


Figure 6.5. Comparison of linear - and nonlinear model

From the temperature plot in Figure 6.5 it is seen that the dynamic response of T_4 is similar for the linear - and nonlinear model. As stated in Section 4.1.1 the temperature transition in the nonlinear model is modelled using a combination of

an ideal flow dependent delay and a low pass filter. The used filter is given in Equation 6.24.

$$G_{f,winter} = \frac{0.0625}{s^2 + 0.5 \cdot s + 0.0625} \quad (6.24)$$

Furthermore the flow dependent delay is given by Equation 6.25

$$t_{d,winter} = \frac{L_2 \cdot A_2}{Q_4} - t_{tr} \quad (6.25)$$

where $t_{tr} = 8$ s. $G_{f,winter}$ and t_{tr} are chosen such that the transition of T_4 in the nonlinear model lies between the response of $T_{4,10}$ in the linear model and the transition of T_4 using an ideal delay.

From Figure 6.5 it is seen that the dynamic response for the pressure and volume flow to the consumer for the linear - and nonlinear model also share similar behavior. Zooming in on the pressure dynamic, shown in Figure 6.6, it can be noticed that the pressure in the linear model is oscillating with a frequency of ≈ 3.5 rad/s, which is the frequency seen to cause a spike in the Bode diagram in Figure 6.4. Furthermore the oscillating dynamic for the pressure is different for the linear - and nonlinear model. This is due to the control volume simplification made for the linear model.

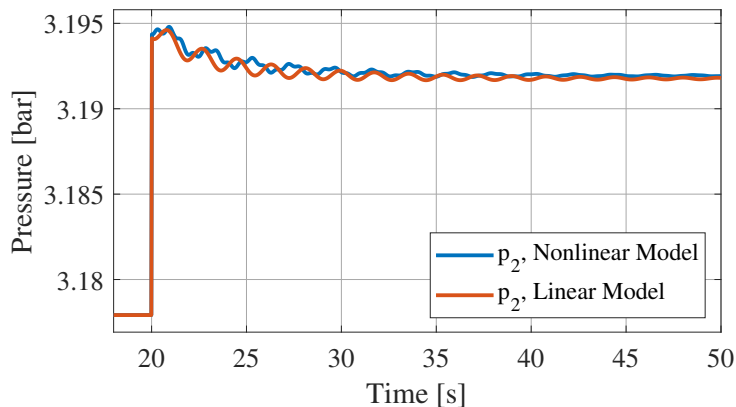


Figure 6.6. Comparison of the pressure, p_2 , of linear - and nonlinear model

From the comparison of the linear - and nonlinear model for the *upper worst case* summer scenario, presented in Appendix H, a larger temperature variation is seen due to the lower fluid velocities. This is simply the consequence of the different modelling methods used to describe the temperature transition.

Despite these temperature variations the linear model is deemed a sufficient representation of the nonlinear model, as the linear model in general show similar transient behaviour for the summer - and winter scenario.

Temperature Estimation 7

In this chapter variations of the Smith Predictor Control (SPC) scheme is proposed with the purpose of generating a non delayed feedback temperature value. This is done in the effort to design the controller used in the SPC scheme more aggressively and potentially allow for better disturbance rejection and hence a lower tracking error.

The time delay caused by the distance between the mixing point and sensor placement and fluid velocity means it is necessary to design the controller more conservatively compared to a case where the time delay is not present. This is due to the fact that the time delay adds negative phase to the system's frequency response. A more conservatively tuned controller will result in decreased disturbance rejection which is undesired for the analysed system. To reduce the impact of the time delay, and thereby making it possible to design the controller more aggressively without causing instability, a Smith Predictor Control (SPC) scheme can be used[10]. The main idea behind the SPC scheme can be visualized in Figure 7.1. Note that the Laplace variable s is left out of the notation in this chapter for simplicity.

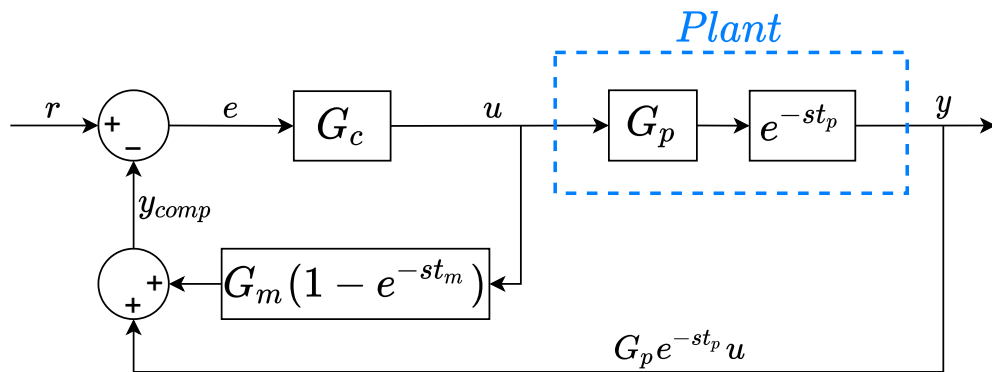


Figure 7.1. Smith Predictor Control scheme

From the block diagram it applies that r is the reference signal, e is the error signal, u is the input signal, y is output signal and y_{comp} is the compensated output signal. The plant is denoted by a transfer function G_p multiplied with a delay term where t_p is the plant delay time. G_p represents the plant dynamics without any delay caused by the nature of the system. G_c is a controller of choice designed to ensure stability. $G_m(1 - e^{-st_m})$ is a compensation term consisting of a model of the delay free plant, G_m , and a delay term with a time delay t_m . The compensation term makes it possible to remove the delay from the output signal assuming that $G_m = G_p$ and $t_p = t_m$.

This is clarified in the derivation below.

$$\begin{aligned}
 y_{comp} &= G_p \cdot e^{-s \cdot t_p} \cdot u + G_m \cdot (1 - e^{-s \cdot t_m}) \cdot u \\
 &= G_p \cdot e^{-s \cdot t_p} \cdot u + G_m \cdot u - G_m \cdot e^{-s \cdot t_m} \cdot u \\
 &= G_m \cdot u
 \end{aligned}$$

From the derivation it states that $y_{comp} = G_m \cdot u$, thus the delay is successfully removed from the feedback signal. However as mentioned, this assumes that the compensation term describes the output perfectly. If G_m is based on a working point and t_m is constant the compensation term will lack precision if system states, parameters, and delay time changes. The same applies if disturbances are present in the system[10]. As a result it is essential to account for compensation mismatch when designing the controller G_c .

As the control solution developed for the described district heating system must function under varies system variations the use of different compensation terms have been analysed. In this report three variations of the SPC scheme are designed and in Chapter 9 the tracking result of the three schemes are showcased to verify how they compare with the classical control solution. The three schemes are described in detail in Section 7.1, but in short it applies that:

- Scheme 1 utilizes the linear model to describe G_m and $G_m \cdot e^{-s \cdot t_m}$.
- Scheme 2 makes use of a Kalman Filter to estimate $T_{4,1}$ and $T_{4,10}$.
- Scheme 3 is based on the original scheme where $G_m = G_{T_{4,1}}$, but t_m is updated.

As clarified each scheme is based on knowledge from the linear model. Note that the working point in the linear model is based on the *upper worst case* summer scenario which is defined in Section 8.1 in Chapter 8. This working point results in the highest delay time. In the following section, each scheme is described in more detail.

7.1 SPC Schemes Description

Scheme 1

For the first SPC scheme the compensation term is based purely on knowledge of the linear model developed in Chapter 6. Due to the design of the linear state space model, it is possible to derive a transfer function between ω_{sp} and $T_{4,1}$, where the delay is greatly reduced, and a transfer function between ω_{sp} and $T_{4,10}$, where the full delay is included. Thus the needed terms to develop the compensation term are directly obtained from the linear model. This means that:

$$G_m = G_{4,1} \quad (7.1)$$

$$G_m \cdot e^{-s \cdot t_m} = G_{4,10} \quad (7.2)$$

Figure 7.2 depicts the block diagram for SPC scheme 1. Here $T_{2,d}$ and $T_{9,d}$ are disturbance signals and $T_{4,n}$ is a noise signal obtained from real measurements in a low temperature zone [9]. Furthermore, G_{LPF} is a low pass filter used to filter out the noise from T_4 . In Appendix I the design of G_{LPF} is found, and it is explained how filters have been designed to construct the disturbance signals and the noise signal used in the simulation model.

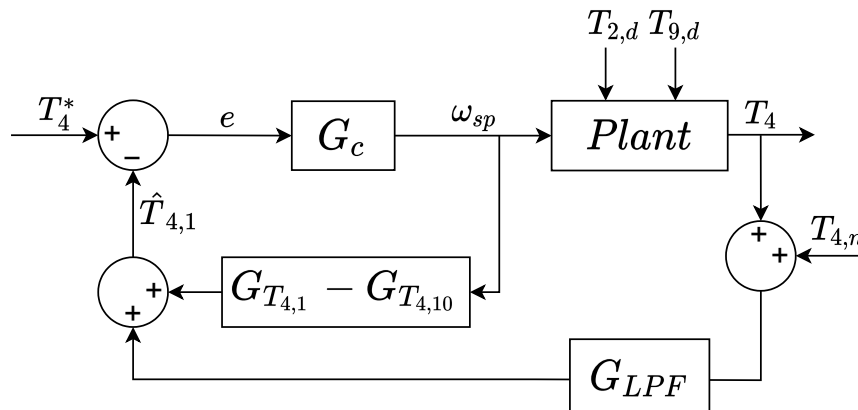


Figure 7.2. Block diagram of SPC scheme 1

Scheme 2

The second SPC scheme utilizes a Kalman Filter to estimate the temperature $T_{4,1}$ and $T_{4,10}$. Therefore the Kalman Filter becomes the compensation term. Compared to the compensation term in scheme 1 the Kalman Filter makes it possible to adjust the value for $T_{4,1}$ and $T_{4,10}$ based on the measured temperature T_4 . As a result the use of a Kalman Filter is proposed in the effort to obtain better delay compensation when the system dynamics deviate from the dynamic behavior in the working point. The simplified block diagram of this SPC scheme can be visualized in Figure 7.3.

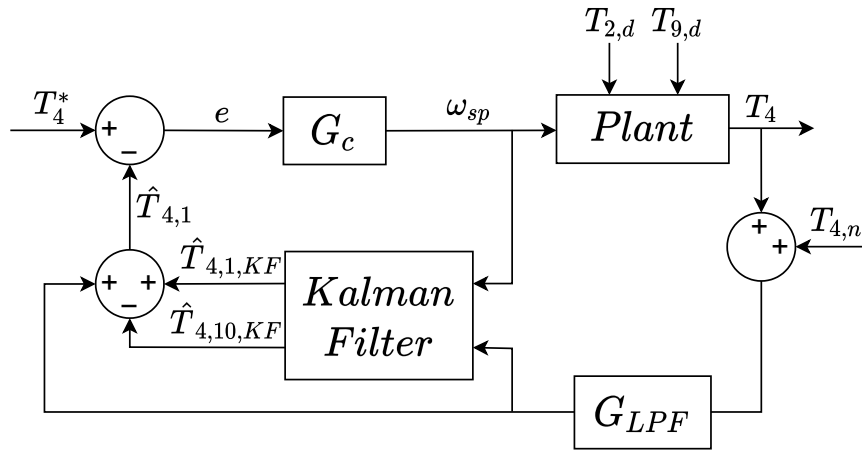


Figure 7.3. Block diagram of SPC scheme 2

Kalman Filter Design

The Kalman Filter used in scheme 2 is a linear Kalman Filter. This type of Kalman Filter is chosen, as it can be designed based on the linear system model as well as take into account the disturbances which are present in the system. As a result of this the Kalman Filter will be based on an augmented state space model which includes the state space system model and a state space disturbance model. In Equation (7.3) and (7.4) the state - and output equation of the system model is stated where a disturbance term \mathbf{d} is added to the state equation.

$$\dot{\mathbf{x}} = \mathbf{A} \cdot \mathbf{x} + \mathbf{B} \cdot u + \mathbf{d} \quad (7.3)$$

$$\mathbf{y} = \mathbf{C} \cdot \mathbf{x} \quad (7.4)$$

The disturbance \mathbf{d} is the output of the state space disturbance model which likewise can be described by a state - and output equation as stated in Equation (7.5) and (7.6).

$$\dot{\mathbf{z}} = \mathbf{A}_d \cdot \mathbf{z} + \mathbf{B}_d \cdot \mathbf{w} \quad (7.5)$$

$$\mathbf{d} = \mathbf{C}_d \cdot \mathbf{z} \quad (7.6)$$

It applies that \mathbf{w} is a Gaussian white noise signal and is the input to the disturbance model and \mathbf{z} is the states of the disturbance model [11]. The disturbance model is based on filters where each filter is designed to let through frequencies in a white noise signal which corresponds to the frequencies that are present in the given disturbance signal. With the disturbance model it is possible to add disturbance to all system states x . For this case disturbance is added to the temperature states T_2 and T_9 . The filter designs are based on raw temperature measurements, where the filters have been designed to pass through low frequencies in the data and attenuate high frequency noise from the temperature sensors. Visualization of the filter design can be found in Appendix I.

The transfer functions of the filters are stated below.

$$G_{T_2,dist} = \frac{0.04}{s + 0.04} \quad \& \quad G_{T_9,dist} = \frac{0.003}{s + 0.003} \quad (7.7)$$

The designed filters are next converted to the state space representation, stated in Equation (7.5) and (7.6).

Equation (7.8) and (7.9) show the state - and output equation respectively of the augmented state space model.

$$\begin{bmatrix} \dot{\mathbf{x}} \\ \dot{\mathbf{z}} \end{bmatrix} = \underbrace{\begin{bmatrix} \mathbf{A} & \mathbf{C}_d \\ 0 & \mathbf{A}_d \end{bmatrix}}_{\bar{\mathbf{A}}} \cdot \begin{bmatrix} \mathbf{x} \\ \mathbf{z} \end{bmatrix} + \underbrace{\begin{bmatrix} \mathbf{B} \\ 0 \end{bmatrix}}_{\bar{\mathbf{B}}} u + \underbrace{\begin{bmatrix} 0 \\ \mathbf{B}_d \end{bmatrix}}_{\bar{\mathbf{G}}} \cdot \mathbf{w} \quad (7.8)$$

$$y = \underbrace{\begin{bmatrix} \mathbf{C} & 0 \end{bmatrix}}_{\bar{\mathbf{C}}} \cdot \begin{bmatrix} \mathbf{x} \\ \mathbf{z} \end{bmatrix} \quad (7.9)$$

The Kalman Filter is designed based on the augmented state space model and is described by Equation (7.10), where \mathbf{L} is the Kalman gain and $\hat{\mathbf{x}}$ is the estimated states [11].

$$\dot{\hat{\mathbf{x}}} = \bar{\mathbf{A}}\hat{\mathbf{x}} + \bar{\mathbf{B}}u + \mathbf{L}(y - \bar{\mathbf{C}}\hat{\mathbf{x}}) \quad (7.10)$$

In order to implement Equation (7.10) the Kalman gain needs to be determined. The Kalman gain can be determined based on the algebraic Ricatti Equation (7.11) and (7.12) [11].

$$\mathbf{L} = (\mathbf{P}_0 \bar{\mathbf{C}}^T + \mathbf{G}\mathbf{R}_{\mathbf{w}\mathbf{v}})R_v^{-1} \quad (7.11)$$

$$\bar{\mathbf{A}}\mathbf{P}_0 + \mathbf{P}_0\bar{\mathbf{A}}^T + \mathbf{G}\mathbf{R}_{\mathbf{w}}\mathbf{G}^T - (\mathbf{P}_0\bar{\mathbf{C}}^T + \mathbf{G}\mathbf{R}_{\mathbf{w}\mathbf{v}})\mathbf{R}_{\mathbf{w}}^{-1}(\mathbf{P}_0\bar{\mathbf{C}}^T + \mathbf{G}\mathbf{R}_{\mathbf{w}\mathbf{v}}) = 0 \quad (7.12)$$

Determining \mathbf{L} requires the weighting parameters $\mathbf{R}_{\mathbf{w}}$ and R_v to be defined as this makes it possible to calculate \mathbf{P}_0 from Equation (7.12). $\mathbf{R}_{\mathbf{w}\mathbf{v}}$ and $\mathbf{R}_{\mathbf{v}\mathbf{w}}$ are also weighting parameters that can be designed, however they are neglected for this case as they do not contribute to a better estimation of $T_{4,1}$ and $T_{4,10}$. It applies that R_v is a scalar while $\mathbf{R}_{\mathbf{w}}$ is a diagonal matrix with the number of entries corresponding to the number of system states. Depending on the desired estimation result $\mathbf{R}_{\mathbf{w}}$ and R_v must be defined differently. In terms of choosing the parameter values, the following applies:

- If R_v is large relative to $\mathbf{R}_{\mathbf{w}}$ the system model is trusted more compared to the measurement.
- If R_v is small relative to $\mathbf{R}_{\mathbf{w}}$ the measurement is trusted more compared to system model [11].

For this case it is desired to have faith in the model but still trust the measurement to an extent such that the estimated states seek towards the measured temperature. When tuning the Kalman gain all \mathbf{R}_w entry values are set to 1 and R_v is adjusted. The chosen value for R_v is 200. At a lower R_v value the system comes close to turn unstable, and at $R_v = 50$ the system turns unstable when trying to track the reference temperature.

The final block diagram of SPC scheme 2 is visualized in Figure 7.4.

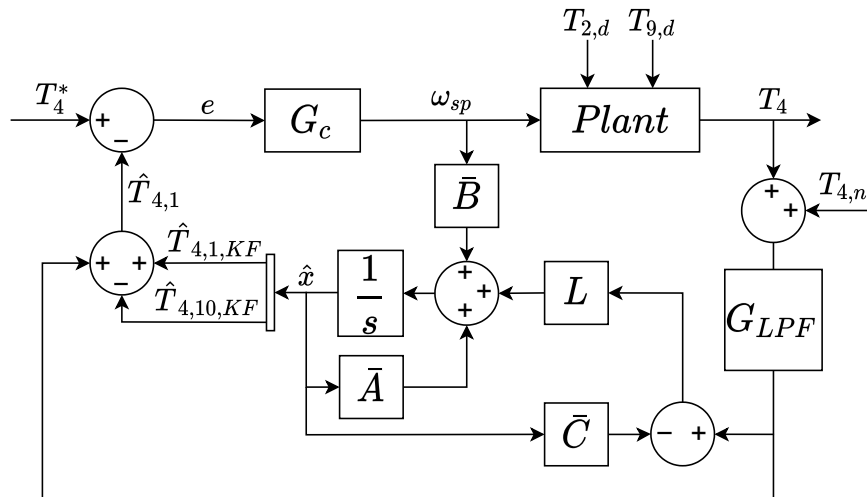


Figure 7.4. Complete block diagram of SPC scheme 2

Scheme 3

The third SPC scheme utilizes the original SPC structure. In this context $G_{T_{4,1}}$ is used to represent G_m . For the delay term e^{-st_m} it is assumed that the delay time t_m can be updated in real time using information from a volume flow sensor, possibly located in the same location as the temperature sensor. Knowledge about the distance between the mixing point and the temperature sensor as well as the pipe diameter is also assumed for this. In the simulation the time delay is implemented using the "Variable Transport Delay" block where the delay time is determined using Equation (7.13).

$$t_m = \frac{L_2 \cdot A_2}{Q_{4,meas}} \quad (7.13)$$

Figure 7.5 depicts the block diagram for SPC scheme 3.

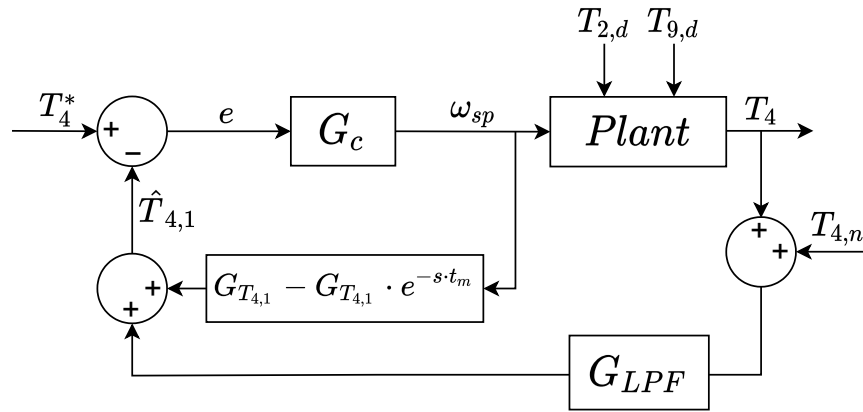


Figure 7.5. Block diagram of SPC scheme 3

7.2 Estimation Results

When investigating the compensation ability of the three SPC schemes a step input is given directly to the shunt pump and then $y_{comp} = \hat{T}_{4,1}$ is compared to the temperature measurement T_4 . Each scheme is tested for two scenarios being the *upper worst case* summer scenario ($t_d \approx 375$ s) and the *standard* winter scenario ($t_d \approx 30$ s). Disturbances, noise, and the filter, G_{LPF} , are removed from the system to fully see the compensation ability of the different schemes. For each scenario the shunt pump is given a positive step of 0.1 % of its original value. Note that the step for the different cases are given at different times. This is done in order to ensure that $\hat{T}_{4,1}$ equals the temperature reference value before the step is initialized.

Figure 7.6, 7.7, and 7.8 show the compensation result for scheme 1, 2, and 3 respectively.

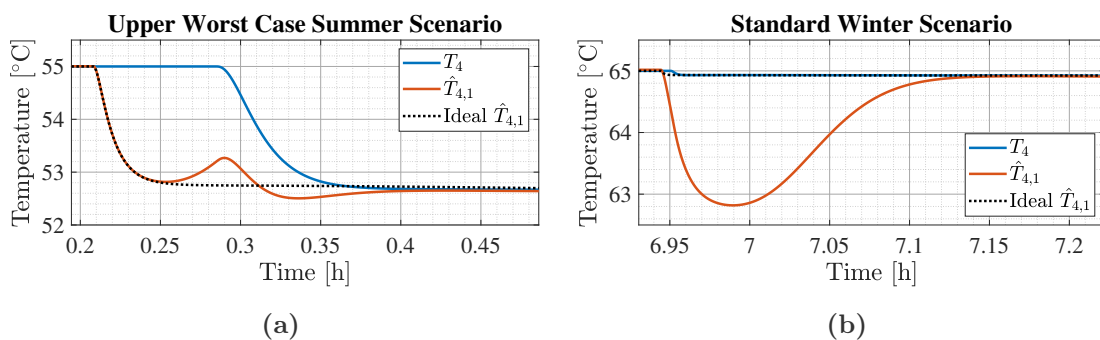


Figure 7.6. Scheme 1 compensation ability

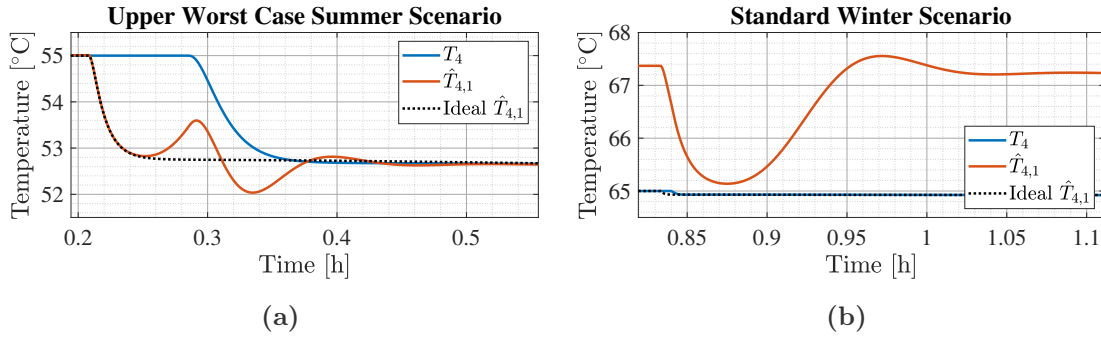


Figure 7.7. Scheme 2 compensation ability

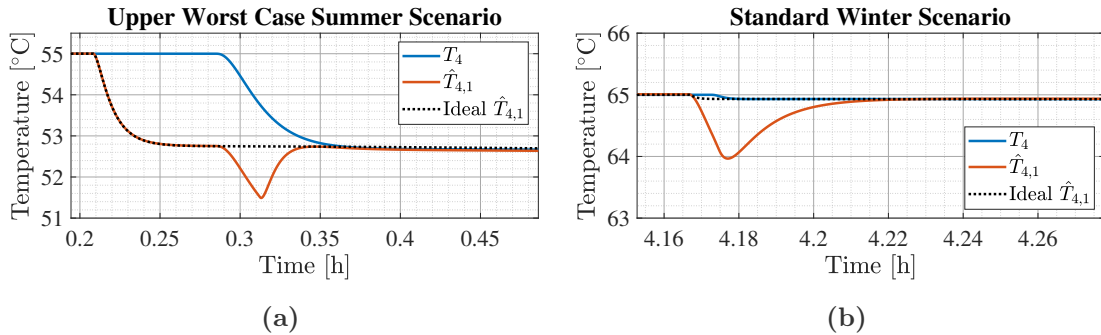


Figure 7.8. Scheme 3 compensation ability

For the summer scenario, it can be observed that neither of the three compensation terms manage to remove the delay perfectly. This is despite the fact that the working point for the linear model is based on this scenario. However the only way to obtain perfect compensation with scheme 1 and hence achieve the ideal $\hat{T}_{4,1}$, would be to have a linear model of $G_{T_{4,10}}$ that matches the response of T_4 perfectly. As seen from the linear/nonlinear model comparison in Appendix H, this is not the case. An important factor in this context is the use of a filter in combination with a transition time to create a smooth temperature transition in the nonlinear model, also illustrated by the plot of T_4 in Figure 7.6a. The chosen curve smoothness may be more or less representative of how a real temperature transition looks like. Therefore the delay compensation may be worse or better in reality. This applies to all three schemes for the summer scenario. For scheme 2 the estimated temperature $\hat{T}_{4,1}$ oscillates more compared to $\hat{T}_{4,1}$ obtained with scheme 1. This is a result of the Kalman Filter trying to correct both of its estimated values, $\hat{T}_{4,1,KF}$ and $\hat{T}_{4,10,KF}$, to follow the measured temperature T_4 . Using scheme 3 the delay compensation is perfect until $t = 0.29$ h where there is a mismatch between the nonlinear model and the compensation term. This is a result of the compensation term using an ideal delay which does not take into account the smooth temperature transition.

For the winter scenario, the compensation result is significantly worse. As all compensation terms are based on the linear model for the *upper worst case* summer

scenario, this result is expected, as the system gain varies a lot, when far away from the working point. However, it is clear that scheme 2 is noticeable worse than scheme 1 and 3. It can be observed in Figure 7.7b that the Kalman filter is not able to estimate the temperature $T_{4,1}$ accurately, resulting in a significant offset. However, it is possible to make the estimation ability of the Kalman Filter better and hence obtain a smaller offset, if the Kalman Filter is tuned to trust the measurement more. However as explained previously this makes the system become unstable in the summer scenario. Based on the summer - and winter results for scheme 2, it can be stated that the estimation ability of the Kalman Filter is highly dependent on the dynamics of the nonlinear system being similar to the dynamics of the linear system. Comparing scheme 1 and scheme 3 it appears that scheme 3 manages to achieve the most accurate delay compensation which is a consequence of the delay time being updated. Despite scheme 3 showing to be the best solution in terms of compensating for the delay, the final tracking results will have to be analysed to determine if it is the best control strategy of the three, as the tracking scenario is different and also includes disturbances.

Control Design 8

In this chapter two controllers are derived. The first controller will be used in the classical control solution and is designed based on $T_{4,10}$ being the output temperature. The second controller will be used in the developed SPC schemes. For this controller ideal delay compensation is assumed, which allows the controller to be designed based on $T_{4,1}$ being the output temperature. An uncertain plant model is derived as a tool to analyse the effect of the system variations and to verify that both control designs ensure robust stability for the set of possible plant perturbations.

8.1 Uncertain Plant Model

In Appendix J a parameter sensitivity analysis has been performed, to show how the system dynamics are influenced by parameter variations. A multiplicative uncertainty model is derived in this section to analyse the combined effect of the parameter variations. Based on the parameter sensitivity analysis, it has been observed that the length and diameter of the pipelines have the most significant influence on the system dynamic and are therefore included as uncertain parameters for the uncertainty model. The uncertain parameters include the pipe length for control volume 1, 4, 8, and 10 and the diameter for every control volume except control volume 6. The uncertainty range for the parameters is denoted in Table 8.1. The uncertainty range for the lengths is based on values which are meant to be realistic despite the simplicity of the district heating grid. For the diameter the uncertainty range is based on considerations of obtaining a realistic fluid velocity and the possible selection of pipeline diameters from Logstor [12]. From Appendix J it has also been noted that the boundary conditions for the pressure can affect the system gain. These are however kept constant due to pump limitations, but it should be kept in mind that a given control solution is not necessarily robust stable if the boundary conditions differ significantly.

The uncertainty model will be used as a tool to measure the stability when designing the controllers. Onwards the entire set of possible perturbed plant models will be denoted Π , a particular perturbed plant model will be denoted $G_P(s)$ and the nominal plant model will be denoted $G(s)$. The magnitude plots for the uncertain plant model describing the temperature $T_{4,1}$ and $T_{4,10}$ are shown in Figure 8.1, and

in Table 8.1 three particular perturbed plant models are presented. The particular plant model $G_{P,1}(s)$ denotes the *standard* plant model. $G_{P,2}(s)$ and $G_{P,3}(s)$ denotes an *upper* - and *lower worst case* model, which are the particular perturbed plant models that deviates the most from the nominal plant model in terms of magnitude. The nominal model is based on the mean value for the length of the pipes, and the diameter is chosen to give approximately the smallest absolute magnitude difference between the nominal plant and $G_{P,2}(s)$ and $G_{P,3}(s)$ at low frequencies. This is done in order to have a relative uncertainty of less than 100% at low frequencies.

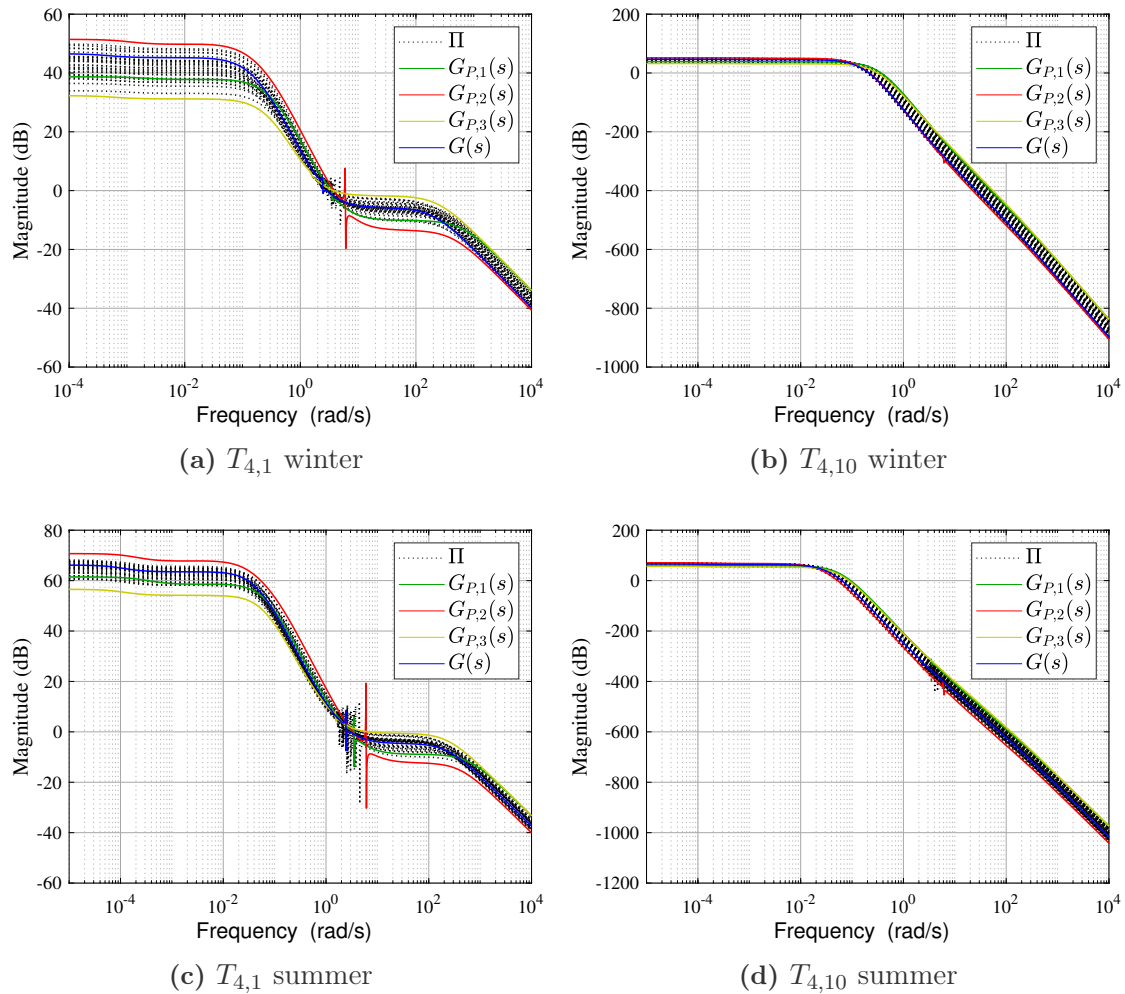


Figure 8.1. Bode diagram of for the uncertain plant model, where Π illustrates the set of possible perturbed plant models, $G_{P,1}(s)$, $G_{P,2}(s)$, $G_{P,3}(s)$ present particular perturbed plant models, and $G(s)$ denotes the nominal plant model

Table 8.1. Uncertain parameter variations and particular perturbed plant models

Uncertain parameter	Nominal value	Minimum value	Maximum value	$G_{P,1}(s)$	$G_{P,2}(s)$	$G_{P,3}(s)$
L_1 & L_{10}	625 m	250 m	1000 m	500 m	250 m	1000 m
L_4 & L_8	625 m	250 m	1000 m	250 m	250 m	1000 m
d	76.6 mm	60.3 mm	88.9 mm	60.3 mm	88.9 mm	60.3 mm

The variations based on the parameter uncertainty is presented with a multiplicative uncertainty. This is illustrated with the block diagram in Figure 8.2, where Δ_I is any stable transfer function which, at each frequency, has a magnitude equal to or less than 1 [13].

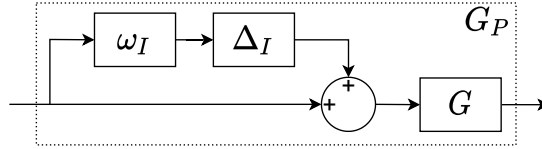


Figure 8.2. Plant with multiplicative uncertainty

The set of possible perturbations can be described by a single lumped complex perturbation, Δ_I , and a weight, $\omega_I(s)$, that creates a disc around the nominal plant at each frequency [13]. The weight is designed to include all possible perturbations by ensuring that the magnitude of the weight function is larger than the worst case relative uncertainty at all frequencies. The expression for the relative uncertainty is written in Equation(8.1) and the requirement for the weight function is expressed in Equation (8.2). The designed weight function for test scenario 2 (a summer day) is illustrated in Figure 8.3 for the temperature $T_{4,1}$. In the figure it can be observed that spikes are present, causing a high relative uncertainty in the frequency span of 2-6 rad/s. These spikes are induced by the pressure dynamic, as described in Section 6.2. The designed weight function for $T_{4,10}$ in the summer scenario is visualized in Appendix K along with the expression for the designed weight functions.

$$l_I(j\omega) = \max_{G_p \in \Pi} \left| \frac{G_p(j\omega) - G(j\omega)}{G(j\omega)} \right| \quad (8.1)$$

$$|\omega_I(j\omega)| \geq l_I(j\omega) \quad \forall \omega \quad (8.2)$$

- $l_I(s)$ - Relative uncertainty [-]
- $\omega_I(s)$ - Rational weight [-]
- $G(s)$ - Nominal plant [-]
- $G_P(s)$ - Particular perturbed plant model [-]
- Π - Set of possible perturbed plant model [-]
- ω - Frequency [rad/s]

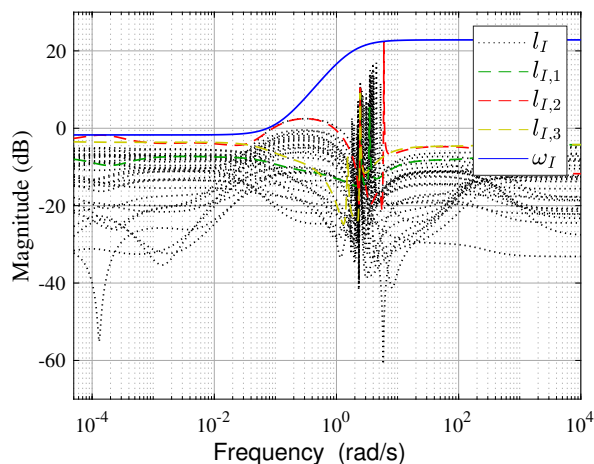


Figure 8.3. Weight function for $T_{4,1}$ - A summer day

The designed weight function, along with the nominal plant and the controller designed in the next section will be used to determine if the system is robust stable. Robust stability is defined as the system being stable about the nominal plant and up to the worst case model uncertainty. The robustness can be checked by Equation (8.3), which equates the upper bound on the complementary sensitivity function, T . This means that the absolute value of the product between the complementary sensitivity function and the rational weight must be less than 1 at all frequencies, indicating that the magnitude of T must be designed to decrease before the weight crosses 0 dB.

$$|\omega_I(j\omega) \cdot T(j\omega)| < 1 \quad \forall \omega \quad (8.3)$$

$$T(s) = \frac{G(s) \cdot G_c(s)}{1 + G(s) \cdot G_c(s)} \quad (8.4)$$

The complimentary sensitivity function is given in Equation (8.4), where $G_c(s)$ is the feedback controller and $G(s)$ is the nominal plant. Based on the robustness requirement, a robust controller for the temperature $T_{4,10}$ is designed in Section 8.2, and a robust controller to be used in the presented SPC schemes is designed in Section 8.3. Both controller designs will be based on the summer scenario as this case will require the most conservative control design, due to the transport delay being most significant for this scenario.

8.2 Controller Design for $T_{4,10}$

The purpose of this section is to design a robust stable controller for the temperature $T_{4,10}$, despite the parameter variations introduced by the uncertainty model and the

defined working point for the summer - and winter day. The block diagram for the control structure is shown in Figure 8.4.

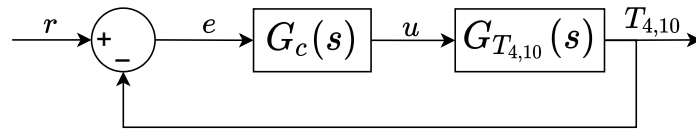


Figure 8.4. Block diagram for the classical control solution

The Bode diagram for the transfer function $G_{T_{4,10}}(s)$ is shown in Figure 8.5 for the nominal plant and the three particular perturbed plant models in the summer scenario. The controller will be designed for the worst case summer scenario, and the controller design is made to obtain a required phase - and gain margin to account for mismatch between the linear - and nonlinear model and to take into account that there may exist uncertainties not included in the uncertainty model. When looking at the Bode diagram in Figure 8.5 it may not be obvious which transfer function defines the worst case scenario. As a result the gain - and phase margin for each transfer function are investigated. Based on this it is noted that the transfer function $G_{P,2}(s)$ defines the worst case scenario as this transfer function results in the lowest margins. As a result this particular perturbed system will need the most conservative controller.

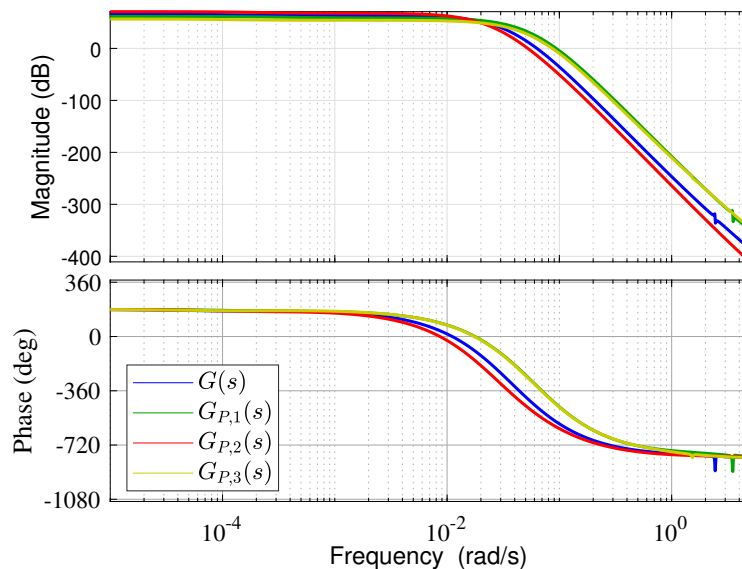


Figure 8.5. Bode diagram of temperature $T_{4,10}$ in the summer scenario for the nominal model and the tree specified perturbed plant models

However, designing the controller for $G_{P,2}(s)$ will yield a *slower* dynamic response for the *standard* summer scenario and for the perturbed winter day scenarios, as the

system gain in these cases are lower, resulting in a lower bandwidth. This is evident in Table 8.3, where the obtained bandwidth for the perturbed winter day scenarios is approximately ten times lower.

It can be observed from the Bode diagram in Figure 8.5 that the parameter variations affect both the gain and phase of the system. It can be noted that the *lower* - and *upper worst case* plant have a DC gain of 56.5 dB and 70.7 dB respectively.

The controller that has been designed for the plant $G_{P,2}(s)$ is a PI controller as it can help increase the low frequency gain as well as increase the bandwidth of the system. The form of the PI controller is written in Equation (8.5)

$$G_c(s) = K_P \cdot \frac{s + \omega_c}{s} \quad (8.5)$$

The PI controller has been tuned to obtain a phase margin of approximately 45 deg and a gain margin of at least 6 dB for $G_c(s) \cdot G_{P,2}(s)$, as these relative stability margins are commonly used limits [14]. Since there is a sign shift in the system, meaning that a positive change in input will result in a negative change in output, the controller is designed with negative gains. In Figure 8.6 the plant $G_{P,2}(s)$, the designed controller $G_c(s)$, and the result open loop system is visualized. Note that both controller and plant has been gained with -1 to better visualize the frequency response.

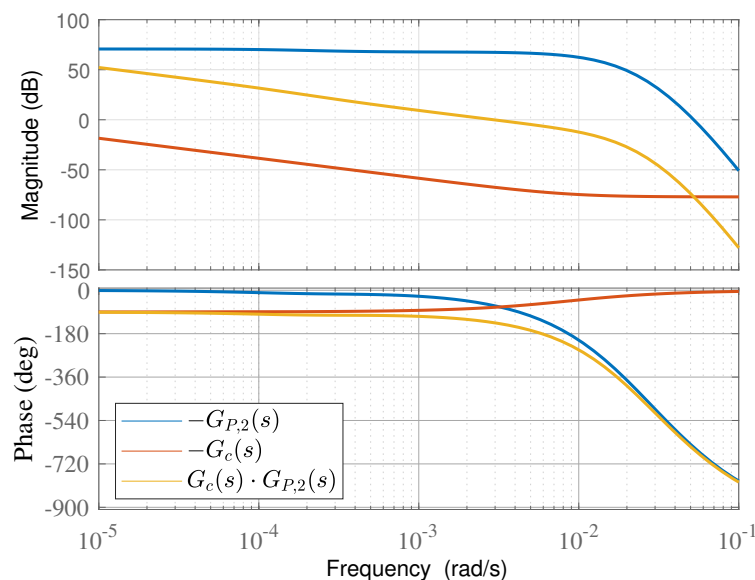


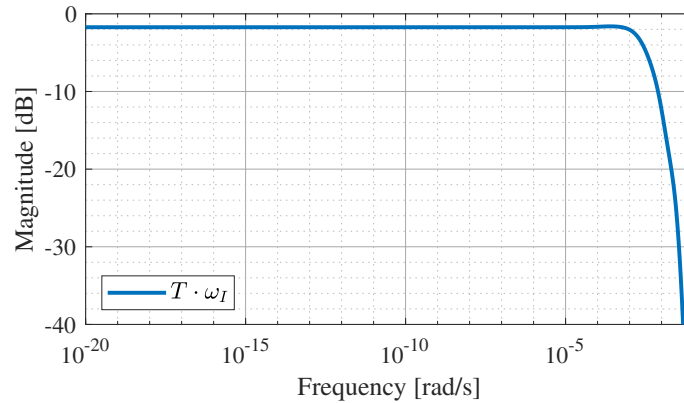
Figure 8.6. Bode diagram for $G_{P,2}(s)$, the designed PI controller, $G_c(s)$, and the resultant open loop system

The controller gains are listed in table 8.2.

Table 8.2. Controller gains

K_P	K_I	ω_c
-1.4×10^{-4}	-11.9×10^{-4}	8.5×10^{-3} rad/s

The system stability is checked with Equation (8.3) and the system is visually shown to be robust stable in Figure 8.7, where the maximum absolute value of $\omega_I \cdot T$ is calculated to be 0.83 (-1.61 dB).

**Figure 8.7.** Robust stability: $|\omega_I \cdot T|_\infty = 0.83$ (-1.61 dB)

The step response for the summer - and winter day scenario is shown in Figure 8.8. It is seen that the settling time is highly affected by the scenario, with a maximum settling time of approximately 1.5 h for the summer scenario compared to 18 h for the winter scenario. This variation is due to the significant difference in gain for the two scenarios, which affects the bandwidth of the system. With the designed controller, the bandwidth (BW), phase margin (PM), and gain margin (GM) are listed in Table 8.3 for the defined particular perturbed plant models for both the winter - and summer test scenario.

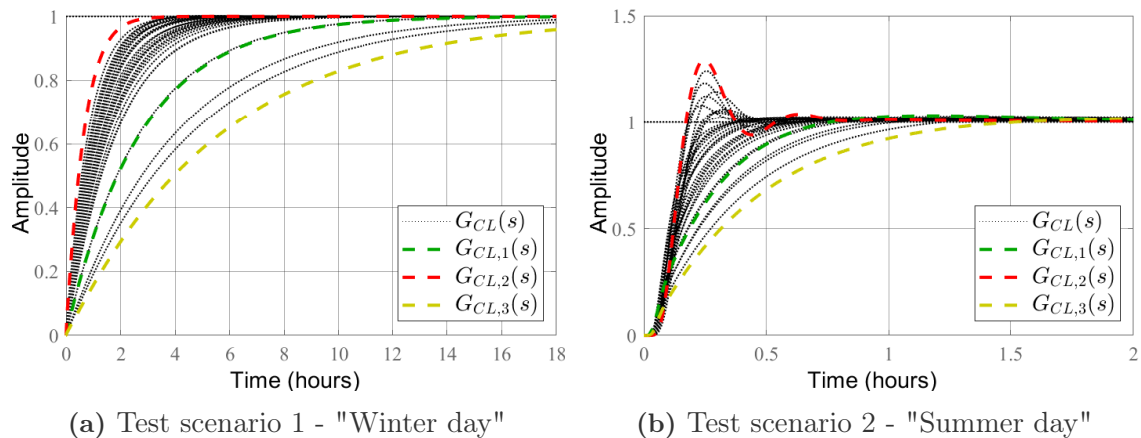
**(a)** Test scenario 1 - "Winter day"**(b)** Test scenario 2 - "Summer day"**Figure 8.8.** Step response for the closed loop system with the designed controller in the two test scenarios

Table 8.3. Stability margins and bandwidth

(a) Test scenario 1 - "Winter day"

	GM	PM	BW
$G_c(s) \cdot G(s)$	35.30 dB	87.26 deg	2.56×10^{-4} rad/s
$G_c(s) \cdot G_{P,1}(s)$	42.90 dB	90.19 deg	1.02×10^{-4} rad/s
$G_c(s) \cdot G_{P,2}(s)$	30.60 dB	87.44 deg	4.51×10^{-4} rad/s
$G_c(s) \cdot G_{P,3}(s)$	49.61 dB	89.65 deg	0.49×10^{-4} rad/s

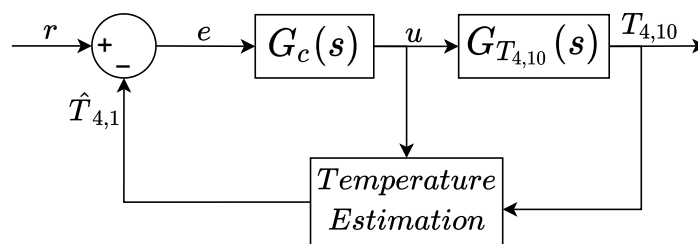
(b) Test scenario 2 - "Summer day"

	GM	PM	BW
$G_c(s) \cdot G(s)$	12.49 dB	71.10 deg	29.79×10^{-4} rad/s
$G_c(s) \cdot G_{P,1}(s)$	19.81 dB	80.49 deg	12.21×10^{-4} rad/s
$G_c(s) \cdot G_{P,2}(s)$	6.22 dB	45.66 deg	66.75×10^{-4} rad/s
$G_c(s) \cdot G_{P,3}(s)$	24.30 dB	84.67 deg	6.72×10^{-4} rad/s

This concludes the design of the classical control solution which will function as a benchmark. In Chapter 5 the control system's ability to track a constant temperature reference with disturbances and noise is showcased.

8.3 Controller Design for $T_{4,1}$

In this section the controller to be used in the presented SPC schemes is designed. Figure 8.9 shows a simplified block diagram of the SPC schemes, where the temperature $\hat{T}_{4,1}$ is the estimation of the intermediate temperature $T_{4,1}$.

**Figure 8.9.** Simplified block diagram for SPC schemes

Under the assumption that the estimation of the temperature $T_{4,1}$ is ideal, meaning that perfect delay compensation is achieved, a controller can in theory be designed to regulate $T_{4,1}$ instead of $T_{4,10}$. This means for the control design the block diagram in Figure 8.9 can be changed to the block diagram seen in Figure 8.10.

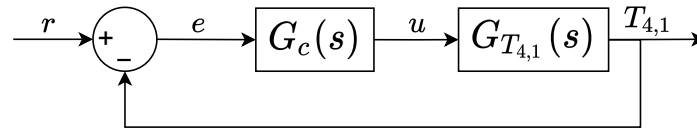


Figure 8.10. Block diagram for control structure assuming ideal temperature estimation

Since the temperature $T_{4,1}$ has a shorter time delay, the control system can be designed to have a higher bandwidth compared to the control system for the temperature $T_{4,10}$. The Bode diagram of the system is shown in Figure 8.11 for the nominal plant model and the particular perturbed plant models specified in Table 8.1.

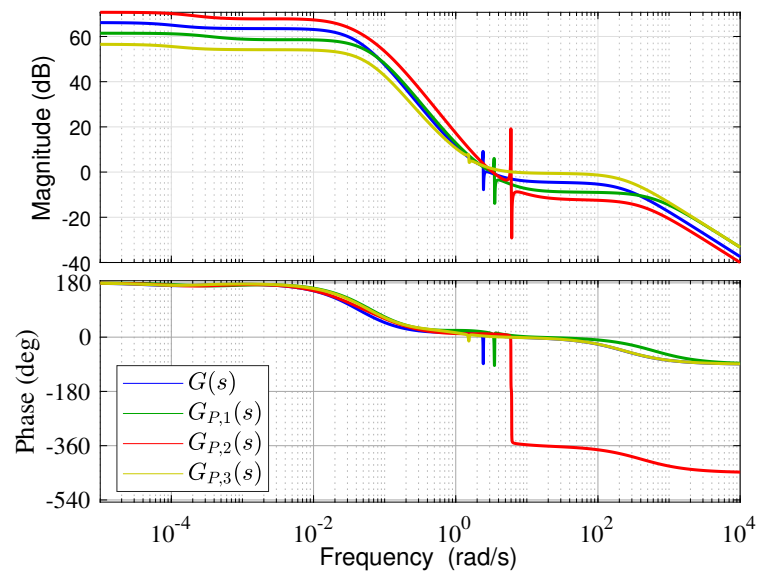


Figure 8.11. Bode diagram of temperature $T_{4,1}$ in the summer scenario for the nominal model and the tree specified perturbed plant models

From the figure it can be seen that the system shows similar dynamics with a second order system when solely looking at the dynamics up to a frequency of $\approx 1 \times 10^1$ rad/s. Note that the variations in DC gain are the same as those stated for $T_{4,10}$ in the summer scenario. To define the worst case plant the disk margin for the perturbed plants has been investigated as the worst case plant cannot be defined by purely looking at the gain - and phase margins. In Table 8.6 the disk margins are noted for the plants multiplied with the designed controller and from here it is observed that the plant $G_{P,2}(s)$ has the disk margin and therefore defines the worst case scenario. As a result the controller design will be based on $G_{P,2}(s)$.

Since the delay time is reduced by designing the controller for $T_{4,1}$, it is possible to design the controller more aggressively. However, as shown in Section 7.2 the prediction ability is not ideal for either of the SPC schemes. Therefore to ensure that the system remains stable, despite the compensation terms not describing the delay time accurately, the controller will be designed to ensure stability in case of additional delay time. For the control design process, it is required that the closed loop system remains stable if the delay time is approximately 100 s larger than the delay time for the *upper worst case* summer scenario.

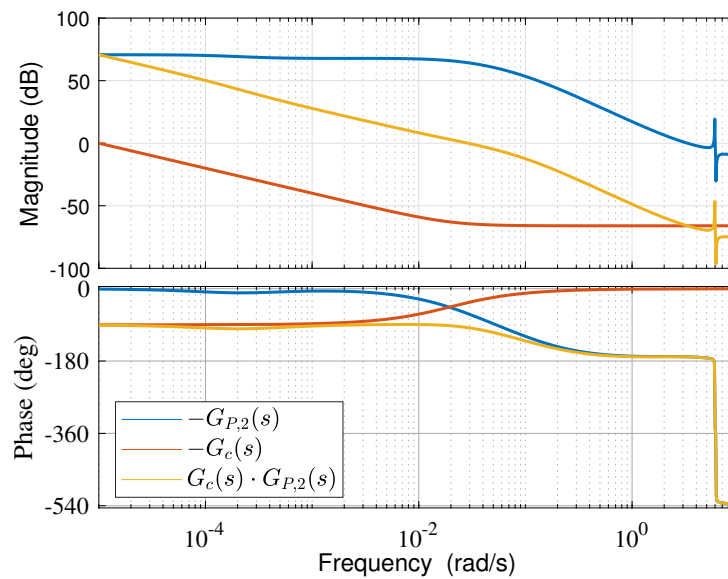


Figure 8.12. Bode diagram for $G_{P,2}(s)$, the designed PI controller, $G_c(s)$, and the resultant open loop system

The Bode diagram for the *upper worst case* plant model, designed controller, and resultant open loop system is shown in Figure 8.12. Note again that the plant and controller have been gained with -1 to account for the sign shift in the system. A PI controller has been designed as it is sufficient to fulfill the control requirement. As seen from the Bode diagram, the system has plenty of margin left so the bandwidth can easily be made larger if desired, however this will violate the control requirement. Without violating the control requirement the system bandwidth has been improved by a factor of five using the PI controller. The gains of the designed PI controller are listed in Table 8.4.

Table 8.4. Controller gains

K_P	K_I	ω_c
-5.0×10^{-4}	-1.0×10^{-5}	2.0×10^{-2} rad/s

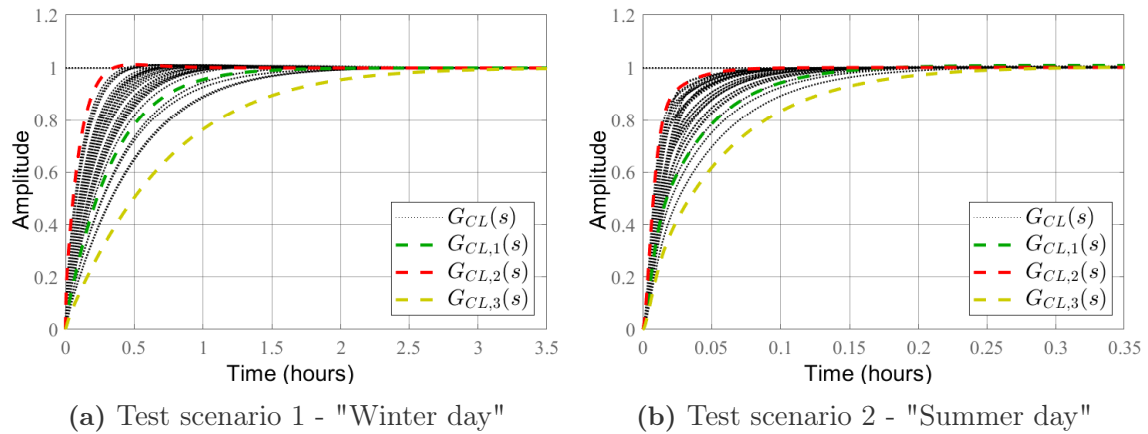


Figure 8.13. Step response for the closed loop system with the designed controller in the two test scenarios

The step response for the two test scenarios is shown in Figure 8.13, where it can be seen that the settling time is improved compared to the step response for the temperature $T_{4,10}$ shown in Figure 8.8. With the designed controller, a maximum settling time of approximate 2.5 h for test scenario 1 and 0.2 h for test scenario 2 is obtained.

In Figure 8.14 the robustness requirement is visually shown for the summer day scenario and is fulfilled. The relative stability margins and bandwidth obtained with this controller are listed in Table 8.5.

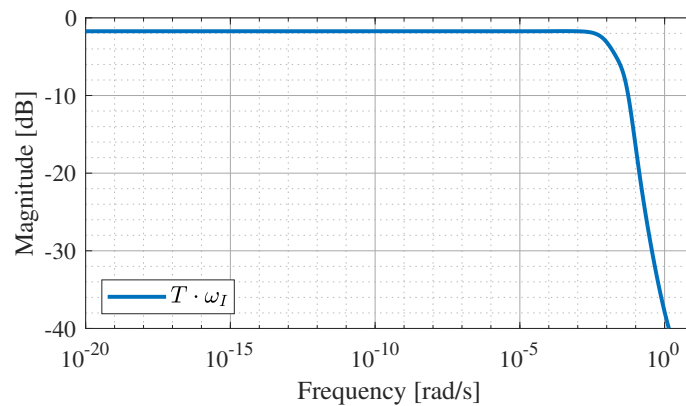


Figure 8.14. Robust stability: $|\omega_I \cdot T|_\infty = 0.82$ (-1.71 dB)

Table 8.5. Relative stability margins and bandwidth

(a) Test scenario 1 - "Winter day"

	GM	PM	BW
$G_c(s) \cdot G(s)$	61.71 dB	91.69 deg	17.96×10^{-4} rad/s
$G_c(s) \cdot G_{P,1}(s)$	64.44 dB	90.01 deg	8.45×10^{-4} rad/s
$G_c(s) \cdot G_{P,2}(s)$	67.43 dB	93.58 deg	30.02×10^{-4} rad/s
$G_c(s) \cdot G_{P,3}(s)$	67.48 dB	87.63 deg	4.12×10^{-4} rad/s

(b) Test scenario 2 - "Summer day"

	GM	PM	BW
$G_c(s) \cdot G(s)$	60.47 dB	87.16 deg	183.02×10^{-4} rad/s
$G_c(s) \cdot G_{P,1}(s)$	62.92 dB	98.57 deg	79.66×10^{-4} rad/s
$G_c(s) \cdot G_{P,2}(s)$	63.76 dB	83.01 deg	349.80×10^{-4} rad/s
$G_c(s) \cdot G_{P,3}(s)$	58.18 dB	94.60 deg	48.44×10^{-4} rad/s

Table 8.6. Disk margins for test scenario 2 - "Summer day"

	GM	PM	DM
$G_c(s) \cdot G(s)$	± 16.24 dB	± 72.47 deg	1.47
$G_c(s) \cdot G_{P,1}(s)$	± 22.76 dB	± 81.67 deg	1.73
$G_c(s) \cdot G_{P,2}(s)$	± 15.56 dB	± 71.07 deg	1.43
$G_c(s) \cdot G_{P,3}(s)$	± 27.05 dB	± 84.92 deg	1.83

As stated the PI controller has been designed to ensure stability despite additional time delay of approximately 100 s. This is verified by deriving the closed loop transfer function for the classical SPC structure. The classical SPC structure is visualized in Figure 7.6 in Chapter 7. Doing block diagrams reduction, the closed loop transfer function becomes [10]:

$$G_{SPC,CL} = \frac{G_c \cdot G \cdot e^{-s \cdot t_p}}{1 + G_c \cdot G - G_c \cdot G \cdot e^{-s \cdot t_m} + G_c \cdot G \cdot e^{-s \cdot t_p}} \quad (8.6)$$

Here it is assumed that $G = G_m = G_p$. Stability is investigated for SPC scheme 1, thus the closed loop transfer function can be stated as:

$$G_{SPC1,CL} = \frac{G_c \cdot G_{T_{4,1}} \cdot e^{-s \cdot t_{p,exp}} \cdot G_f}{1 + G_c \cdot G_{T_{4,1}} - G_c \cdot G_{T_{4,10}} + G_c \cdot G_{T_{4,1}} \cdot G_{padé}} \quad (8.7)$$

As it is not possible to plot a step response for a transfer function with an exponential function in the denominator, a 3rd order padé approximation of a delay has been used [15].

$$G_{padé} = \frac{120 - 60(T_{p,padé} \cdot s) + 12(T_{p,padé})^2 - (T_{p,padé})^3}{120 + 60(T_{p,padé} \cdot s) + 12(T_{p,padé} \cdot s)^2 + (T_{p,padé} \cdot s)^3} \quad (8.8)$$

As the padé approximation is less accurate, a standard time delay has been used in the numerator in combination with a filter G_f . The filter is stated below.

$$G_f = \frac{0.0004}{s^2 + 0.04 \cdot s + 0.0004} \quad (8.9)$$

For the exponential term and the padé approximation it apply that $T_{p,exp} = t_p - 140$ and $T_{p,padé} = t_p - 40$, where t_p is the original time delay for the *upper worst case* summer scenario. The offsets in terms of -140 and -40 are given to $T_{p,exp}$ and $T_{p,padé}$ respectively to have each delay representation match the delay behavior of T_4 . It applies that $t_p = 375 + t_{extra}$ where t_{extra} is the additional time delay and 375 is the calculated delay time for the *upper worst case* summer scenario. In Figure 8.15 the comparison between the different delay representations can be seen.

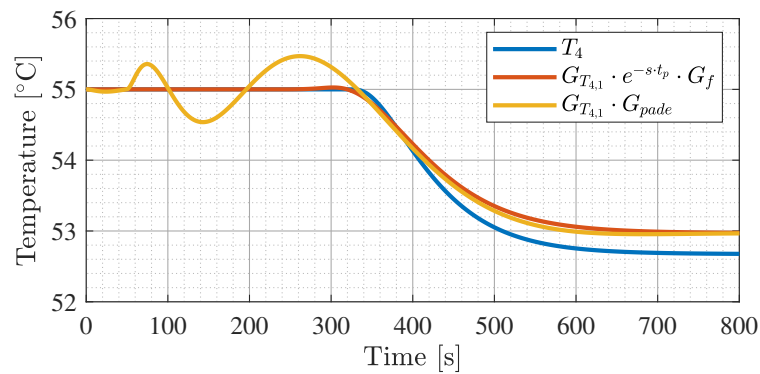


Figure 8.15. Comparison of delay representations

With the designed closed loop transfer function it can be observed from Figure 8.16 that the system remains stable for an additional delay time of $t_{extra} = 120$ s. If $t_{extra} = 130$ s the plant goes unstable corresponding to the analysis. As a result the system requirement with the designed PI controller is fulfilled.

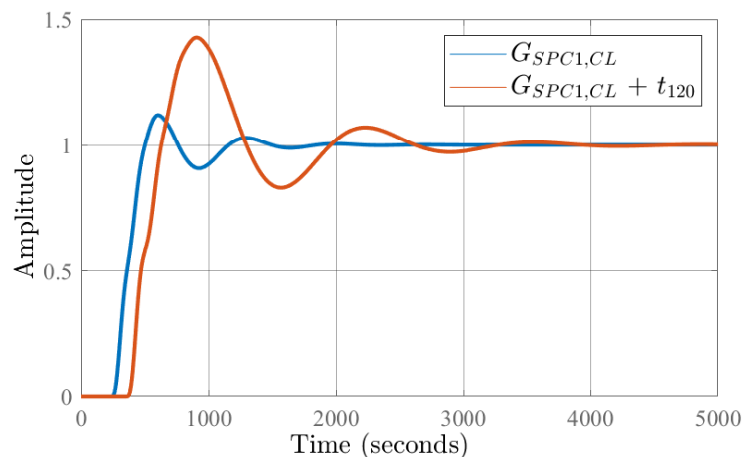


Figure 8.16. SPC scheme 1 closed loop step response for $t_{extra} = 0$ and $t_{extra}=120$

This concludes the design of the controller which will be used in the SPC schemes. In Chapter 9 the temperature tracking performance of the proposed SPC schemes will be compared to the tracking performance of the classical control solution.

Temperature Tracking Results 9

In this chapter the temperature tracking result for the classical control solution and the three Smith Predictor Control schemes are showcased.

The temperature tracking performance of the four control solution has been tested for the *upper worst case* summer scenario and the *standard* winter scenario. For each scenario the controllers are set to track a constant reference temperature as this would be the main purpose of the control solutions in the low temperature zone. This way it is possible to identify how well each control solution handles the disturbances coming from the variations in the temperature T_2 and T_9 . For the summer scenario the temperature reference is set to 55 °C and for the winter scenario the reference is set to 65 °C. In order to compare the control solutions the root mean square (RMS) error and maximum absolute error are found. In table 9.1 and 9.2 the tracking results for the summer and winter scenario are shown.

Table 9.1. Simulation tracking results

Upper Worst Case Summer Scenario		
	RMS Error [°C]	Max Error [°C]
Classical Control Solution	0.109	0.387
SPC Scheme 1	0.113	0.391
SPC Scheme 2	0.084	0.288
SPC Scheme 3	0.125	0.429

Table 9.2. Simulation tracking results

Standard winter scenario		
	RMS Error [°C]	Max Error [°C]
Classical Control Solution	0.414	1.190
SPC Scheme 1	0.462	1.422
SPC Scheme 2	1.150	2.146
SPC Scheme 3	0.351	0.960

Comparing the summer - and winter result of the classical control solution (benchmark) it can be seen that the RMS error is four times greater in the winter scenario. This is due to the plant having a lower gain at lower frequencies in this

scenario compared to the gain at low frequencies in the summer scenario. As a result the control system is overly conservative in the winter scenario and will not be able to react as well to the disturbances as it will in the summer scenario. Overall the results from Table 9.1 and 9.2 show that the idea of using a Smith Predictor Control strategy does not improve the systems ability to reject disturbances and hence achieve a better temperature tracking performance. A better tracking result is only achieved with scheme 2 in the summer scenario and with scheme 3 in the winter scenario. In next section it will be described why the designed SPC schemes does not lead to the desired performance. An explanation will be given to each of the schemes.

9.1 Result Explanation

SPC Scheme 1

For reference the block diagram of SPC scheme 1 can be seen in Figure 9.1.

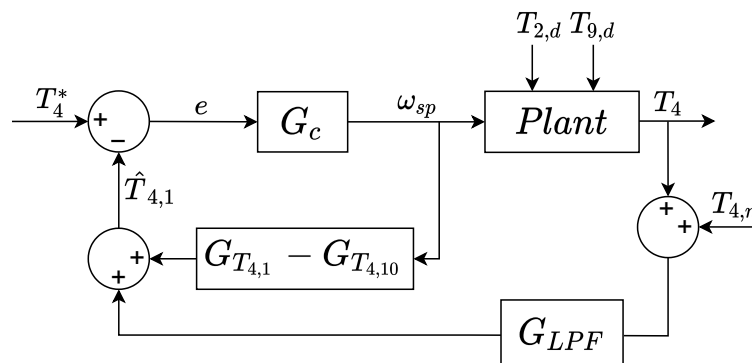


Figure 9.1. Block diagram of SPC scheme 1

Compared to the classical control solution, scheme 1 leads to a worse tracking performance for both test scenarios. In Figure 9.2 and 9.3 the simulation results for scheme 1 are presented.

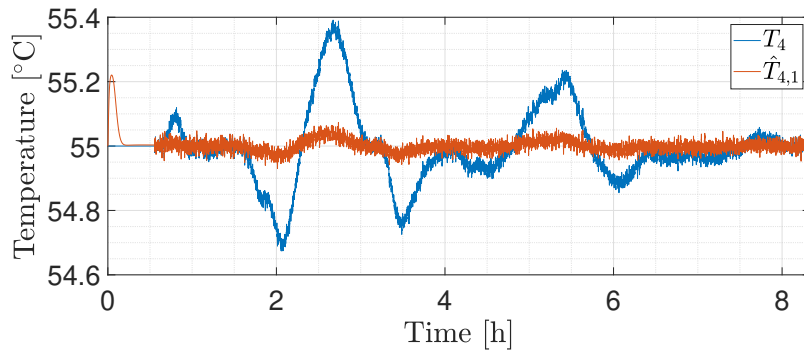


Figure 9.2. Scheme 1 simulation results for the *upper worst case* summer scenario

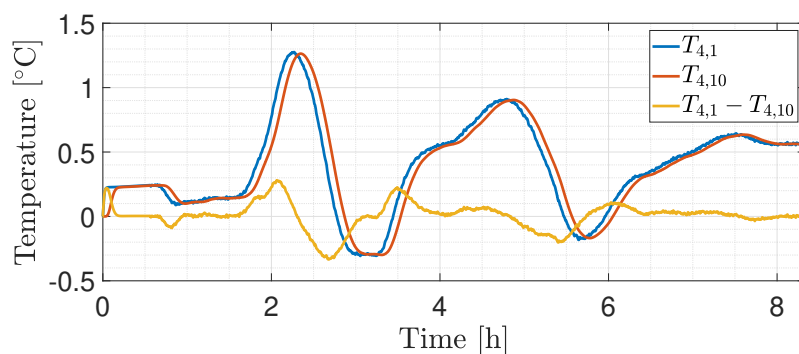


Figure 9.3. Scheme 1 simulation results for the *upper worst case* summer scenario

The first thing to notice from the figure is the initialisation period, where $\hat{T}_{4,1}$ increases and then decreases again. This is due to the equilibrium point used in the linear model not being equal to the equilibrium point used for the nonlinear system. This is a consequence of the simplifications made for the linear model. Therefore the linear system is given a small step in the beginning, however the consequence is small as $\hat{T}_{4,1}$ finds the reference value before the disturbances are initialized at 2000 s = 0.56 h. This initialization time is the same for all cases. The unimproved disturbance rejection using SPC scheme 1 comes down to the fact that the compensation term ends up cancelling the temperature measurement. This is in fact a result of the compensation term trying to remove the delay from T_4 . In Figure 9.3, the yellow line represents the output of the compensation term. This value will be added to T_4 and then result in $\hat{T}_{4,1}$, which is compared to the reference temperature. As seen $\hat{T}_{4,1}$ has a much lower amplitude and therefore a smaller error will be generated for the controller to react on. If the delay compensation would have been less accurate, then $T_{4,1}$ and $T_{4,10}$ would have been closer to each other resulting in the yellow line being closer to zero. In Appendix L the winter result can be found for scheme 1. The explanation made above also applies for the winter scenario.

SPC scheme 2

For reference the block diagram of SPC scheme 2 can be seen in Figure 9.4.

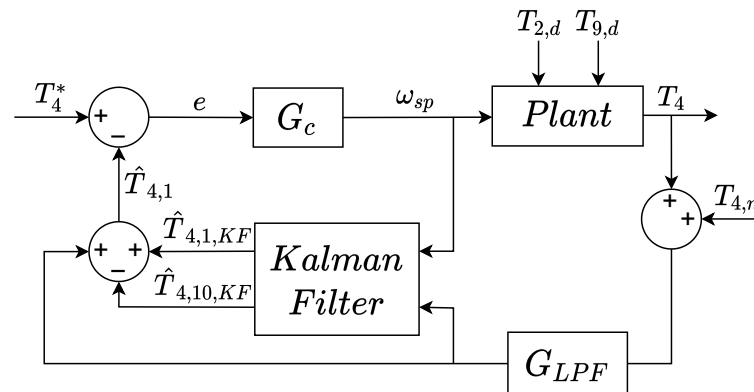


Figure 9.4. Block diagram of SPC scheme 2

SPC scheme 2 is the only scheme which seemingly manages to improve the disturbance rejection for the summer scenario. At the same time this scheme results in the worst tracking performance for the winter scenario. Compared to the other schemes, scheme 2 uses a Kalman Filter in order to estimate T_4 and the delay free T_4 . In the simulation model the delay free T_4 is the input value to the transport delay used in control volume 2. In Figure 9.5 and 9.6 the estimation results can be seen.

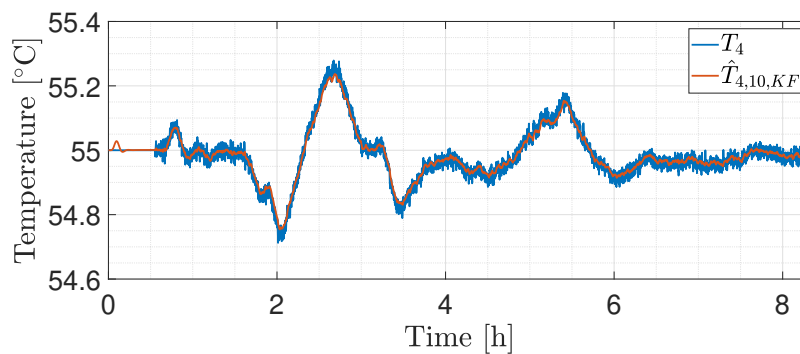


Figure 9.5. SPC scheme 2 estimation result for the *upper worst case* summer scenario

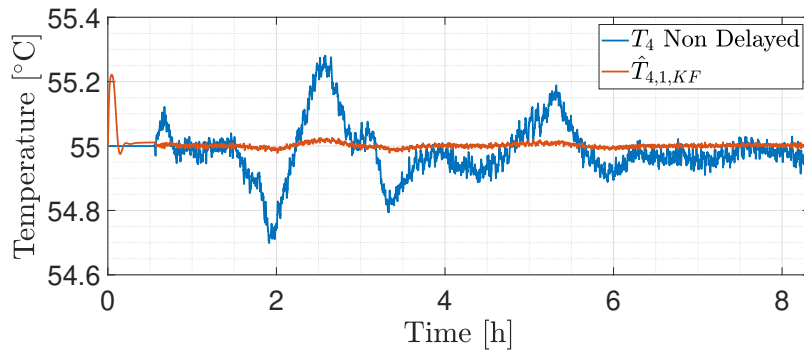


Figure 9.6. SPC scheme 2 estimation result for the *upper worst case* summer scenario

From the figures it is seen that the Kalman Filter estimates T_4 well as $\hat{T}_{4,10,KF}$ follows T_4 accurately. On the contrary the Kalman Filter lacks ability tracking " T_4 Non Delayed". The lack in ability to track " T_4 Non Delayed" results in a similar behavior as seen in Figure 9.2 and 9.3 for scheme 1. Figure 9.7 and 9.8 show the simulation results for scheme 2.

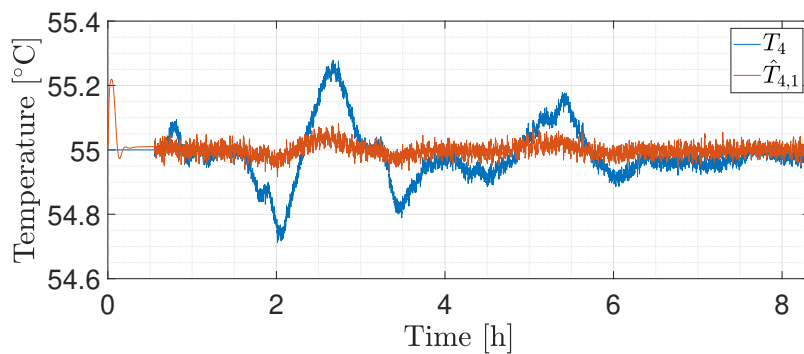


Figure 9.7. Scheme 2 simulation results for the *upper worst case* summer scenario

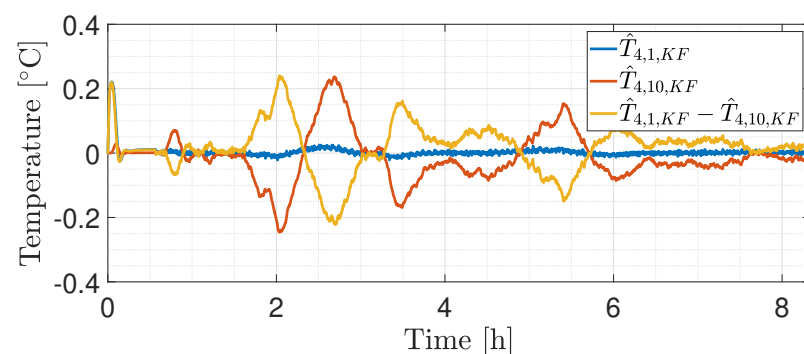


Figure 9.8. Scheme 2 simulation results for the *upper worst case* summer scenario

Just as for scheme 1, the output of the Kalman Filter ends up reducing the measured temperature T_4 signal, which results in a lower error for the controller to react on.

Compared to scheme 1, scheme 2 on the other hand does improve the disturbance rejection. This is possibly a result of $\hat{T}_{4,1}$ having a slight higher amplitude compared to the generated $\hat{T}_{4,1}$ value in scheme 1. For the winter scenario the worst result is obtained using scheme 2. This is a consequence of the estimation becoming worse, due to the winter scenario being far away from the working point which the Kalman Filter is based on. The estimation result for the winter scenario is illustrated in Figure 9.9 and 9.10.

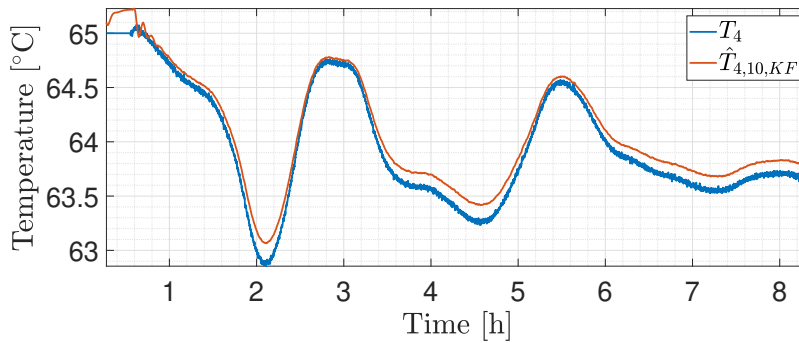


Figure 9.9. Scheme 2 estimation result for the *standard* winter scenario

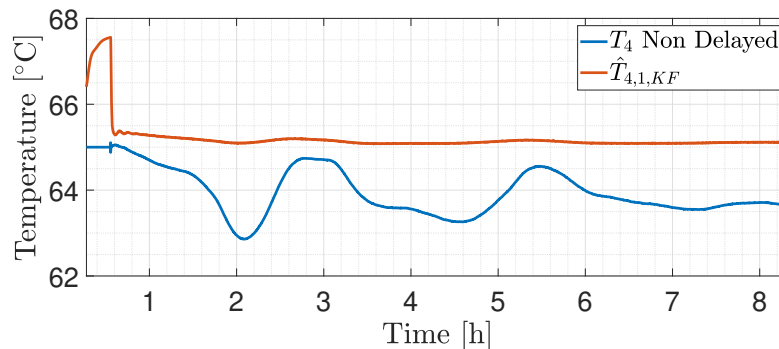


Figure 9.10. Scheme 2 estimation result for the *standard* winter scenario

Here the main thing to notice is the value for $\hat{T}_{4,1,KF}$ before the disturbance is initialized at $t = 0.56$ h. This shows that the Kalman Filter only manages to keep $\hat{T}_{4,1,KF}$ inside a distance of about 2°C to the true value of "T₄ Non Delayed". This is especially due to the difference in pump velocity for the linear - and nonlinear model equilibrium point.

SPC Scheme 3

For reference the block diagram of SPC scheme 3 can be seen in Figure 9.11.

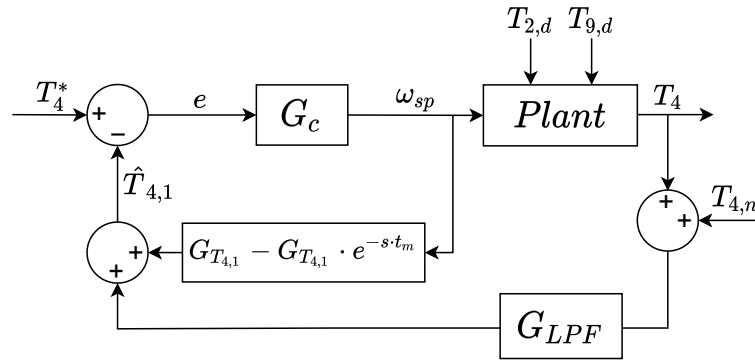


Figure 9.11. Block diagram of SPC scheme 3

SPC scheme 3 is the only control solution which improves the tracking result for the winter scenario. For the summer scenario the tracking result is slightly worse compared to scheme 1. The simulation results for the summer scenario are almost identical to the simulation results for scheme 1. Thus the summer simulation results for scheme 3 will not be shown here, but can be found in Appendix L. In Figure 9.12, 9.13, and 9.14 the simulation results for the winter scenario can be seen.

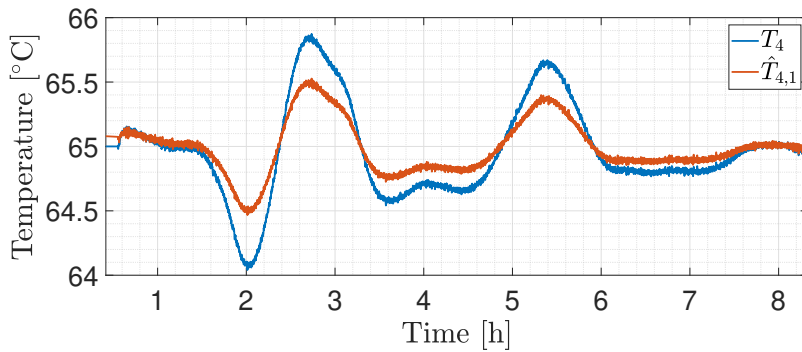


Figure 9.12. Scheme 3 simulation results for the *standard* winter scenario

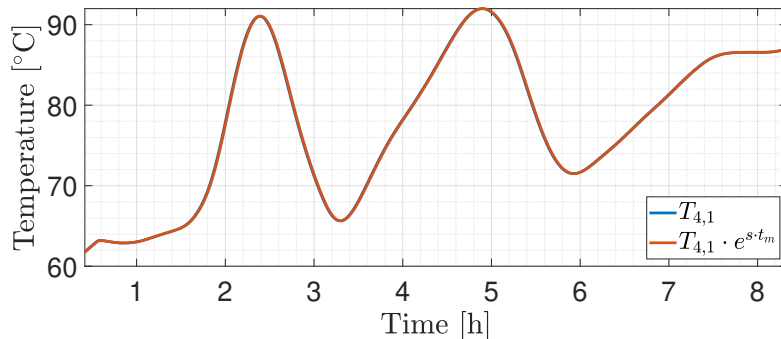


Figure 9.13. Scheme 3 simulation results for the *standard* winter scenario

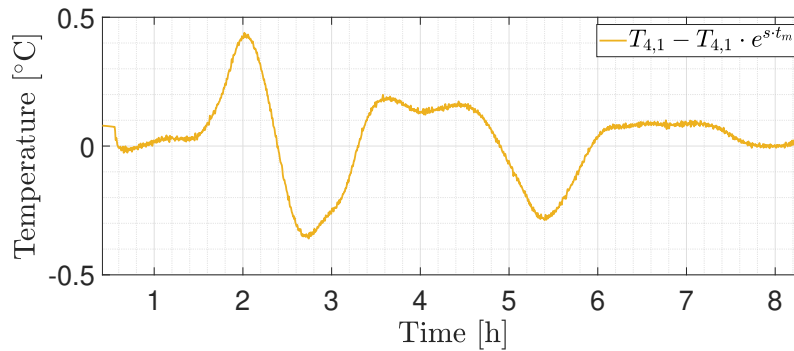


Figure 9.14. Scheme 3 simulation results for the *standard* winter scenario

From the figure it is seen that the control solution manages to generate a $\hat{T}_{4,1}$ value that comes close to T_4 . This is a consequence of the compensation term achieving a better delay compensation as this means that the value for $T_{4,1}$ and $T_{4,1} \cdot e^{s \cdot t_m}$ is closer to each other. This means a greater error signal is generated. Despite the generated error still being smaller than the true error, a better disturbance rejection is obtained due to the more aggressive controller being used in the SPC scheme, compared to the classical control solution. In the end this means that a better tracking performance is obtained.

9.2 Final Thoughts

On the basis of the results presented above it can be concluded that a SPC solution is not the way to go for this kind of system. The SPC solutions that has been investigated can help to compensate for the delay in T_4 when the system operates close to the working point, but fails to do so when far away. This is evident from the estimation results presented in Chapter 7. However being able to compensate for the delay does not help against the disturbances as this will require the control system to know disturbances ahead of time. From the results, the reason why the system does not turn unstable for the summer scenario is most likely due to the error generated being greatly reduced compared to the true error. As a result the controller will react less aggressively. Therefore the SPC solutions counteract themselves and becomes irrelevant. SPC scheme 3 does however manage to improve the tracking performance for the winter scenario. This is caused by a combination of the aggressive controller and the compensation term managing together with T_4 to generate a large error signal.

However in stead of using a SPC solution a better way may be to use a classical feedback loop where the controller is able to tune itself such that it is more aggressively tuned in winter periods and more conservatively tuned in summer periods.

Conclusion 10

The purpose of this report is to investigate how a temperature control solution for a low temperature zone in a district heating grid can be designed to improve the temperature tracking performance of the water temperature sent to the consumers. The flow dependent transport delay of the system limits how aggressively a classical control loop can be designed, and this affects the control system's ability to reject disturbances. As a result the proposed control solution seeks to reduce the effect of the flow dependent transport delay, to allow for a more aggressively tuned control system and thereby improve the disturbance rejection. Furthermore, since this study focuses on a general solution for a low temperature zone, the proposed control solution must be robust stable to parameter variations and seasonal changes.

The report proposes three variations of a Smith Predictor Control scheme to compensate for the flow dependent transport delay. The compensation terms used in the three schemes all build on the derived linear model and prove to be sensitive to a change in the system dynamics.

For the three Smith Predictor Control variations, a Proportional Integral controller which ensures robust stability has been designed. The robust stability is analysed for a summer - and winter day scenario and is based on an uncertainty model, which include parameter variations for the length and diameter of the pipelines. From the robustness analysis it is concluded that the summer scenario needs the most conservative controller, as this scenario yields the most significant transport delay, and the Proportional Integral controller is therefore designed for this case.

The three Smith Predictor Control variations are compared to a classical feedback control solution to verify if the temperature tracking performance has been improved when following a constant reference temperature while exposed to temperature disturbances. Variations in pressure also disturb the performance of the control system, however these variations are neglected and are therefore not taken into account in the control design process.

Based on the simulation results it is concluded that the use of the designed Smith Predictor Control schemes do not improve the disturbance rejection and hereby obtain a better temperature tracking performance. This is a consequence of the compensation terms used in the schemes not being able to compensate for the delay in the disturbances. As the proposed control solution does not help achieve the improved tracking performance, another solution can be to use a classical control

loop with a controller that is able to update its control parameters automatically. The aim will be for the controller to tune itself more conservatively in periods where the system gain is high, and more aggressively in periods where the system gain is low. This way the impact of the transport delay is indirectly reduced as it is not necessary to design the controller based on a worst case scenario. Lastly, it must be emphasized that for any future solution it is highly relevant to include the pressure variations, as these constitute a great disturbance factor for the control system and must be taken care of.

Bibliography

- [1] Henrik Lund, Sven Werner, Robin Wiltshire, Svend Svendsen, Jan Eric Thorsen, Frede Hvelplund, and Brian Vad Mathiesen. 4th generation district heating (4gdh) integrating smart thermal grids into future sustainable energy systems. *Energy*, 68:1–11, 2014. doi: <http://dx.doi.org/10.1016/j.energy.2014.02.089>.
- [2] Dansk Fjernvarme. *Fjernvarmen har aldrig været grønnere*, 2022. URL <https://www.mynewsdesk.com/dk/dansk-fjernvarme/pressreleases/fjernvarmen-har-aldrig-vaeret-groennere-3150842>. 22-02.
- [3] News European Parliament. *What is carbon neutrality and how can it be achieved by 2050?*, 2021. URL <https://www.europarl.europa.eu/news/en/headlines/society/20190926ST062270/what-is-carbon-neutrality-and-how-can-it-be-achieved-by-2050>. 8/4 2022.
- [4] Dietrich Schmidt, Anna Kallert, Markus Blesl, Svend Svendsen, Hongwei Li, Natasa Nord, and Kari Sipilä. Low temperature district heating for future energy systems. *Energy Procedia*, 116:26–38, 2017. doi: <https://doi.org/10.1016/j.egypro.2017.05.052>.
- [5] *Information gathered from conversations with Brian Kongsgaard Nielsen from Grundfos*.
- [6] Charles L. Phillips and John M. Parr. *Feedback Control Systems Fifth Edition*. Pearson Education, 2011. ISBN 978-93-325-0760-9.
- [7] Anders Hedegaard Hansen. *Fluid Power Systems DRAFT Revision - Version 0.4*. FPMS Department of Energy Technology Aalborg University, 2019.
- [8] Grundfos Research and Technology. *The Centrifugal Pump*.
- [9] Werner Bech Madsen. *Data from GEV*, 2022.
- [10] A. Bahill. A simple adaptive smith-predictor for controlling time-delay systems: A tutorial. *IEEE Control Systems Magazine*, 3(2):16–22, 1983. doi: 10.1109/MCS.1983.1104748.
- [11] Per Johansen. *Multi Variable and Non-linear Control Methods*, 2021. URL https://www.moodle.aau.dk/pluginfile.php/2249212/mod_resource/content/0/Lec12.pdf. Course held at Aalborg University on the 8th semester of the Mechatronic Control Engineering master.

- [12] LOGSTOR. *Industry calculator*, 2022. URL <https://designtool.logstor.com/Tool/Form.aspx?ApplicationId=48459a6c-9636-44a9-91c1-b3a8757240cf&CloneUpdate=1&Act=Edit&RecordID=50>. 14/03/2022.
- [13] Ian Postlethwaite and Sigurd Skogestad. *Multivariable Feedback Control: Analysis and Design*. John Wiley And Sons Ltd, 2005. ISBN 978-0-470-01168-3.
- [14] Henrik Clemmensen Pedersen. *Fundamental Control Theory*, 2019. URL https://www.moodle.aau.dk/pluginfile.php/1496899/mod_resource/content/3/MM12_slides.pdf. Course held at Aalborg University on the 4th semester of the Energy Engineering bachelor.
- [15] Vladimir Hanta and Aleš Procházka. *RATIONAL APPROXIMATION OF TIME DELAY*, 2009. URL https://www.researchgate.net/publication/237396133_RATIONAL_APPROXIMATION_OF_TIME_DELAY. 30/05/2022.
- [16] Yunus A. Cengel, John Cimbala, and Robert H. Turner. *Fundamentals of Thermal-Fluis Sciences*. McGraw-Hill Education, 2017. ISBN 978-9-814-72095-3.
- [17] Danfoss. *Radiator Valves, RA-N, Normal flow, DN 20, Straight, D 013G0036*, 2022. URL <https://store.danfoss.com/is/en/Climate-Solutions-for-heating/Radiator-Thermostats/Radiator-Valves/Build-on-valves/Radiator-Valves%2C-RA-N%2C-Normal-flow%2C-DN-20%2C-Straight%2C-D/p/013G0036>. 17/4.
- [18] Robert R. Ross Val S. Lobanoff. *Centrifugal Pumps: Design and Application, Second Edition*. Gulf Professional Publishing, 1992. ISBN 978-0-08-050085-0.
- [19] Jesper Carl Corfitzen. *Se jordtemperaturen i Danmark måned for måned*, 2022. URL <https://www.bolius.dk/se-jordtemperaturen-i-danmark-maaned-for-maaned-35105>. 7/04/2022.
- [20] Sebastian Pelt. *Januar blev den syvende varmeste målt i Danmark*, 2022. URL <https://vejrv2.dk/2022-02-01-januar-blev-den-syvende-varmeste-maalt-i-danmark#:~:text=I%20henhold%20til%20den%2C%20er%20den%20normale%20middeltemperatur,temperaturstigning%20i%201%3%B8bet%20af%20de%20sidste%2030%20%3%A5r>. 7/04/2022.
- [21] Alexander Boye Boes og Christian Holmstedt Hansen. *Renovering af ledningsnet: Dimensionering, ledningstab og konkurrenceevne*. Grøn Energi, 2019.

Appendices

Efficiency Analysis



An analysis has been made to investigate if a low temperature zone makes it possible to lower the thermal losses and hence increase the energy efficiency in the defined district heating grid. The energy efficiency analysis is carried out for the *standard* summer scenario. The grid efficiency η is defined in Equation (A.1).

$$\eta = \frac{q_{6,loss}}{q_1 - q_{11}} \quad (\text{A.1})$$

- η - Efficiency [%]
- $q_{6,loss}$ - Heat flow transferred to consumer [W]
- q_1 - Heat flow entering control volume 1 [W]
- q_{11} - Heat flow leaving control volume 10 [W]

The efficiency is analysed by varying the volume flow through the shunt pump and the volume flow through the bypass section. The volume flow through the bypass section is swept for values equal to 0.0 %, 2.5 %, 5 %, 10 %, 25 %, 35 % and 40 % of the volume flow through control volume 4. For each of these bypass flows the volume flow through the shunt pump is swept for values in the interval [0 L/s - 1.0 L/s]. Figure A.1 shows the result of the analysis.

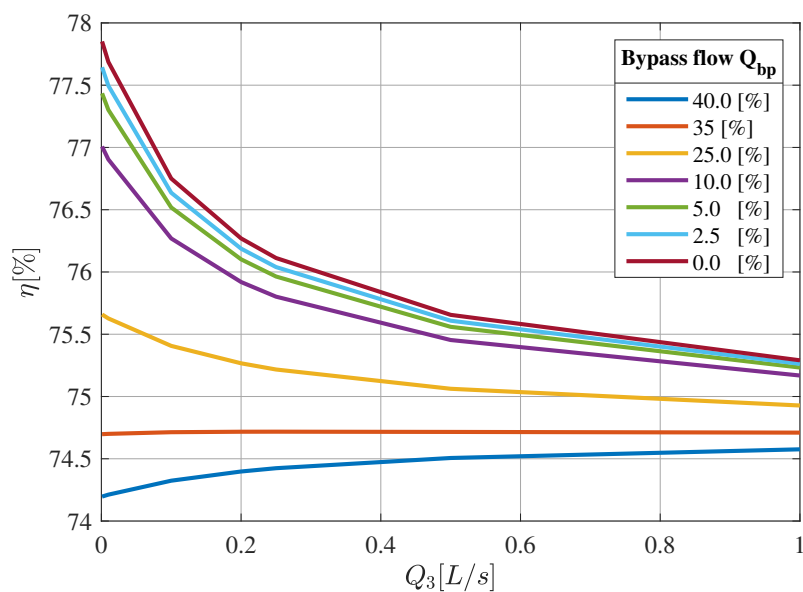


Figure A.1. Efficiency plot for 70 °C supply temperature

From the figure it is seen that the highest efficiency is obtained when both the volume flow through the shunt pump and the bypass section is zero. As a result the interplay between the shunt pump and the bypass section cannot contribute to lower thermal losses, and hence a higher energy efficiency. However, from the figure it can be seen that an increase in volume through the shunt pump does have an positive impact on the efficiency if the volume flow through the bypass section is above 35 %.

Doing the same analysis with a supply temperature equal to 60 °C shows that the energy efficiency will increase. However it is still true that the highest efficiency is obtained when both the volume flow through the shunt pump and the bypass section are zero. Figure A.2 shows the analysis result when the supply temperature equals 60 °C.

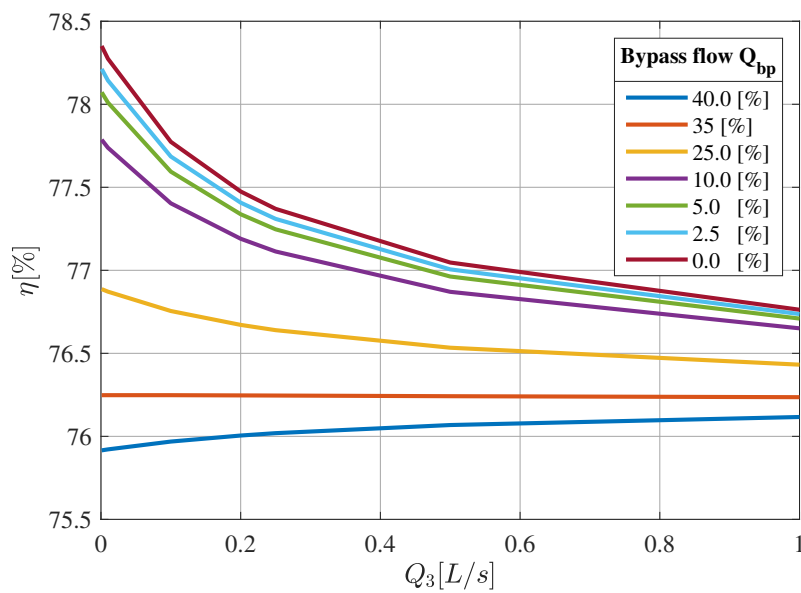


Figure A.2. Efficiency plot for 60 °C supply temperature

Determination of Flow Type **B**

Reynolds number is calculated to determine whether the water flow in the district heating pipes are laminar or turbulent. For the flow to be fully laminar, Reynolds number must be below 2000 and for the flow to be fully turbulent Reynolds number must be above 2400 [7].

Reynolds number is calculated using Equations (B.1)

$$RE = \frac{u \cdot d}{\nu} \quad (\text{B.1})$$

where u is the mean fluid velocity, d is the hydraulic diameter and ν is the kinetic viscosity [7].

For the calculation of Reynolds number $d = 60 \text{ mm}$, $\nu = 0.8007 \times 10^{-6} \text{ m}^2/\text{s}$ which is the kinetic viscosity of water at 30°C . If $v = 0.1 \text{ m/s}$ then $RE = 7494$, thus the flow is turbulent. The chosen scenario is considered being close to worst case, thus Reynolds number will in reality be even higher. Furthermore the kinetic viscosity will change to a lower value when the temperature increases. This will also contribute to a higher Reynolds number.

As a result it is deemed acceptable to consider the flow as turbulent at all times.

Model Parameters



In this appendix the parameters used for the standard winter and summer scenario are listed.

PARAMETERS			
Symbol	Description	Value	Unit
β^*	Bulk modulus of water	2.3243e9	Pa
ρ_w	Density of water at 55 °C	985.2 [16]	$\frac{kg}{m^3}$
ρ_{air}	Density of air	1.2754 [16]	$\frac{kg}{m^3}$
ν	Kinematic viscosity of water at 55 °C	5.1090e-07 [16]	$\frac{m^2}{s}$
a_{h0}	Centrifugal pump coefficient	21.9635	$\frac{s^2}{m}$
a_{h1}	Centrifugal pump coefficient	-829.8199	$\frac{s^2}{m^3}$
a_{h2}	Centrifugal pump coefficient	5.8103e4	$\frac{s^2}{m^5}$
A_{house}	Area of one consumer house	200	m^2
$c_{p,air}$	Specific heat capacity of air	1006 [16]	$\frac{J}{kg \cdot K}$
c_w	Specific heat capacity of water	4183 [16]	$\frac{J}{kg \cdot K}$
$d_1 = d_2 = d_4 = d_8 = d_{10}$	Hydraulic pipe diameter	0.0603	m
d_6	Hydraulic pipe diameter	0.03015	m
$D_1 = D_2 = D_4 = D_8 = D_{10}$	Diameter of casing	0.125	m
g	Acceleration of gravity	9.82	$\frac{m}{s^2}$
H_{house}	Height of one house	2.5	m
K_v	Valve constant	2.7778e-5 [17]	$\frac{m^3}{s \cdot Pa}$
$L_1 = L_{10}$	Pipe length	500	m
$L_4 = L_8$	Pipe length	250	m
L_6	Pipe length	30	m
L_3	Pipe length	10	m
L_2	Pipe length	30	m
L_9	Pipe length	1	m
n_{house}	Number of houses	50	—

* Bulk modulus of water is calculated for 1.5 bar and 3.5 bar using the Equation for K_s found in Appendix "Vibrations and Noise in Pumps" in [18]. The value used in the system is the average of bulk modulus at 1.5 and 3.5 bar.

Dynamic Model Equations D

The district heating grid which the model is based on is illustrated in Figure D.1.

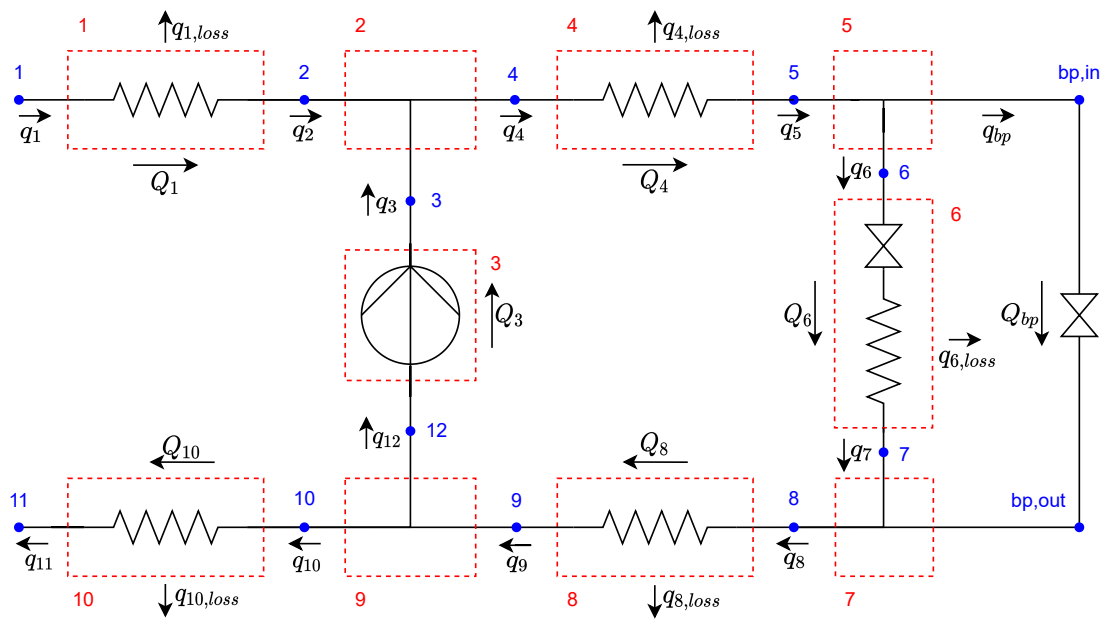


Figure D.1. District heating grid divided into control volumes and nodes

D.1 Control Volume Equations

Control Volume 1

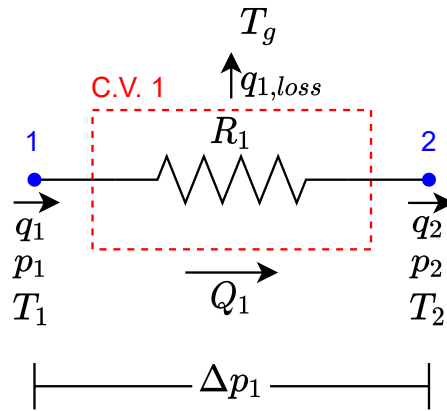


Figure D.2. Control volume 1

Determination of \dot{Q}_1 :

$$\dot{Q}_1 = \frac{A_1 \cdot (p_1 - p_2 - \Delta p_1)}{\rho_w \cdot L_1} \quad (\text{D.1})$$

where

$$\Delta p_1 = \lambda \cdot \frac{L_1}{d_1} \cdot \rho_w \cdot \frac{u_1^2}{2} \quad \text{where} \quad u_1 = \frac{Q_1}{A_1} = \frac{Q_1}{\pi \cdot \left(\frac{d_1}{2}\right)^2} \quad (\text{D.2})$$

λ is given by Equation (D.3).

$$\lambda = 0.3164 \cdot \frac{1}{Re^{\frac{1}{4}}} \quad \text{where} \quad Re = \frac{d_1 \cdot u_1}{\nu} \quad (\text{D.3})$$

Determination of T_2 :

$$q_1 = q_2 + q_{1,loss} + q_{1,w} \quad (\text{D.4})$$

where

$$q_1 = Q_1 \cdot \rho_w \cdot c_{p,w} \cdot T_1 \quad (\text{D.5})$$

$$q_2 = Q_1 \cdot \rho_w \cdot c_{p,w} \cdot T_2 \quad (\text{D.6})$$

$$q_{1,loss} = \frac{1}{R_1} \cdot \left(\frac{T_1 + T_2}{2} - T_g \right) \quad (\text{D.7})$$

$$q_{1,w} = c_{p,w} \cdot m_1 \cdot \dot{T}_2 \quad \text{where} \quad m_1 = A_1 \cdot L_1 \cdot \rho_w \quad (\text{D.8})$$

By inserting Equation (D.5) - (D.8) into Equation (D.4), then \dot{T}_2 can be isolated for, and T_2 can be determined through integration of \dot{T}_2 .

Control Volume 2

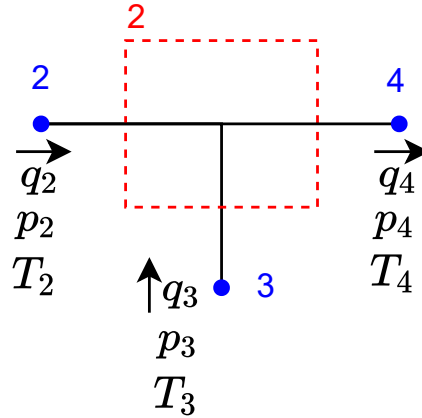


Figure D.3. Control volume 2

Determination of \dot{p}_2 :

$$\dot{p}_2 = \frac{\beta}{\frac{V_1}{2} + \frac{V_2}{2}} \cdot (Q_1 + Q_3 - Q_4) \quad (\text{D.9})$$

where

$$V_1 = A_1 \cdot L_1 = \pi \cdot \left(\frac{d_1}{2}\right)^2 \cdot L_1 \quad (\text{D.10})$$

$$V_2 = A_2 \cdot L_2 = \pi \cdot \left(\frac{d_2}{2}\right)^2 \cdot L_2 \quad (\text{D.11})$$

Determination of T_4 :

$$q_2 + q_3 = q_4 \quad (\text{D.12})$$

where

$$q_2 = Q_1 \cdot \rho_w \cdot c_{p,w} \cdot T_2 \quad (\text{D.13})$$

$$q_3 = Q_3 \cdot \rho_w \cdot c_{p,w} \cdot T_3 \quad (\text{D.14})$$

$$q_4 = Q_4 \cdot \rho_w \cdot c_{p,w} \cdot T_4 \quad (\text{D.15})$$

By inserting Equation (D.13) - (D.15) into Equation (D.12), then T_4 can be isolated for.

Transport delay time to delay T_4 :

$$t_d = \frac{L_2 \cdot A_2}{Q_4} - t_{transition} \quad (\text{D.16})$$

Control Volume 3

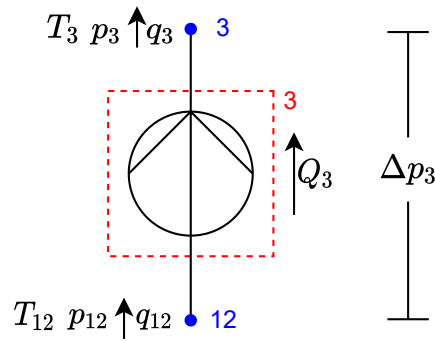


Figure D.4. Control Volume 3

Volume flow through centrifugal pump:

$$Q_3 = \frac{a_{h1} \cdot \omega_{sp} + \sqrt{4 \cdot a_{h0} \cdot a_{h2} \cdot \omega_{sp}^2 + a_{h1}^2 \cdot \omega_{sp}^2 - 4 \cdot \frac{p_3 - p_8}{\rho \cdot g} \cdot a_{h2}}}{2 \cdot a_{h2}} \quad (D.17)$$

Determination of T_3 :

$$q_{12} = q_3 + q_w \quad (D.18)$$

where

$$q_{12} = Q_3 \cdot \rho_w \cdot c_{p,w} \cdot T_{12} \quad (D.19)$$

$$q_3 = Q_3 \cdot \rho_w \cdot c_{p,w} \cdot T_3 \quad (D.20)$$

$$q_{3,w} = c_{p,w} \cdot m_3 \cdot \dot{T}_3 \quad \text{where} \quad m_3 = A_3 \cdot L_3 \cdot \rho_w = \pi \cdot \left(\frac{d_3}{2}\right)^2 \cdot L_3 \cdot \rho_w \quad (D.21)$$

By inserting Equation (D.19) - (D.21) into Equation (D.18), then \dot{T}_3 can be isolated for, and T_3 can be determined through integration of \dot{T}_3 .

Control Volume 4

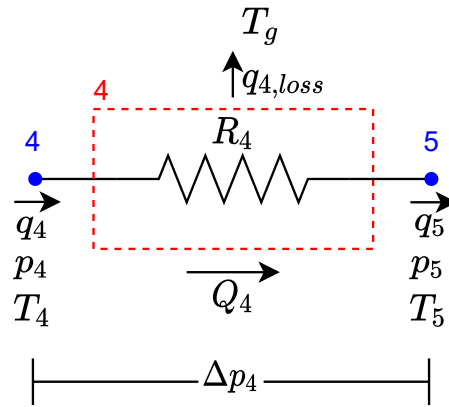


Figure D.5. Control volume 4

Determination of \dot{p}_5 :

$$\dot{p}_5 = \frac{\beta}{\frac{V_4}{2} + \frac{V_6}{2}} \cdot (Q_4 - Q_5) \quad (\text{D.22})$$

where

$$V_4 = A_4 \cdot L_4 = \pi \cdot \left(\frac{d_4}{2}\right)^2 \cdot L_4 \quad (\text{D.23})$$

$$V_6 = A_6 \cdot L_6 = \pi \cdot \left(\frac{d_6}{2}\right)^2 \cdot L_6 \quad (\text{D.24})$$

Determination of \dot{Q}_4 :

$$\dot{Q}_4 = \frac{A_4 \cdot (p_4 - p_5 - \Delta p_4)}{\rho_w \cdot L_4} \quad (\text{D.25})$$

where

$$\Delta p_4 = \lambda \cdot \frac{L_4}{d_4} \cdot \rho_w \cdot \frac{u_4^2}{2} \quad \text{where} \quad u_4 = \frac{Q_4}{A_4} \quad (\text{D.26})$$

λ is given by Equation (D.27)

$$\lambda = 0.3164 \cdot \frac{1}{Re^{\frac{1}{4}}} \quad \text{where} \quad Re = \frac{d_4 \cdot u_4}{\nu} \quad (\text{D.27})$$

Conservation of energy:

$$q_4 = q_5 + q_{4,loss} + q_{4,w} \quad (\text{D.28})$$

where

$$q_4 = Q_4 \cdot \rho_w \cdot c_{p,w} \cdot T_4 \quad (\text{D.29})$$

$$q_5 = Q_4 \cdot \rho_w \cdot c_{p,w} \cdot T_5 \quad (\text{D.30})$$

$$q_{4,loss} = \frac{1}{R_4} \cdot \left(\frac{T_4 + T_5}{2} - T_g \right) \quad (\text{D.31})$$

$$q_{4,w} = c_{p,w} \cdot m_4 \cdot \dot{T}_5 \quad \text{where} \quad m_4 = A_4 \cdot L_4 \cdot \rho_w \quad (\text{D.32})$$

By inserting Equation (D.29) - (D.32) into Equation (D.28), then \dot{T}_5 can be isolated for, and T_5 can be determined through integration of \dot{T}_5 .

Control Volume 5

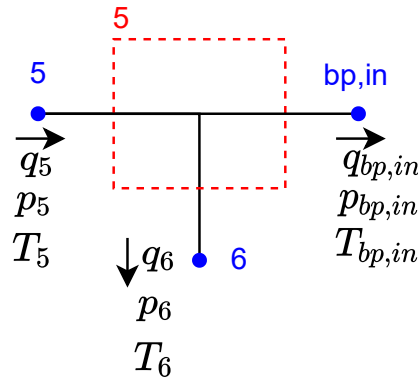


Figure D.6. Control volume 5

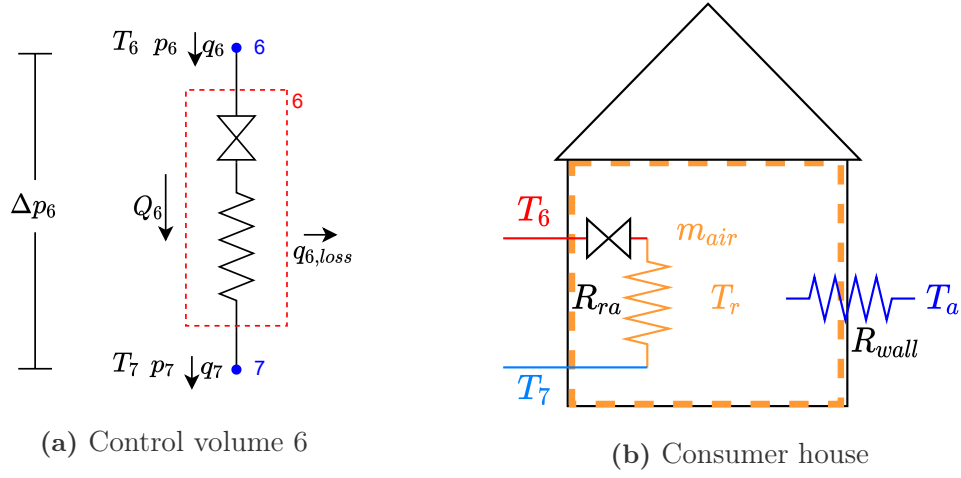
The temperature and pressure in node 5, 6, and bp, in are identical.

The volume flow through the bypass pipe section is given by Equation (D.33).

$$Q_{bp,in} = Q_4 \cdot f_{bp} \quad (\text{D.33})$$

where f_{bp} is a factor deciding the percentage of volume flow Q_4 that runs through the bypass section.

Control Volume 6



Determination of \dot{p}_7 :

$$\dot{p}_7 = \frac{\beta}{\frac{V_6}{2} + \frac{V_8}{2}} \cdot (Q_6 + Q_{bp} - Q_8) \quad (\text{D.34})$$

where

$$V_8 = A_8 \cdot L_8 = \pi \cdot \left(\frac{d_8}{2}\right)^2 \cdot L_8 \quad (\text{D.35})$$

Determination of \dot{Q}_5 :

$$\dot{Q}_6 = \frac{A_6 \cdot (p_6 - p_7 - \Delta p_6)}{\rho_w \cdot L_6} \quad (\text{D.36})$$

where

$$\Delta p_6 = \left(\frac{Q_6}{K_v \cdot x_{valve}}\right)^2 \quad \text{and} \quad x_{valve} = G_{PI} \cdot (T_r^* - T_r) \quad (\text{D.37})$$

Determination of T_r :

$$q_{6,loss} = q_r + q_a \quad (\text{D.38})$$

where

$$q_{6,loss} = \frac{1}{R_{ra}} \cdot \left(\frac{T_6 + T_7}{2} - T_r\right) \quad (\text{D.39})$$

$$q_r = c_{air} \cdot m_{air} \cdot \dot{T}_r \quad \text{where} \quad m_{air} = H_{house} \cdot A_{house} \cdot \rho_{air} \cdot n_{house} \quad (\text{D.40})$$

$$q_a = \frac{1}{R_{wall}} \cdot (T_r - T_a) \quad (\text{D.41})$$

The room temperature T_r is determined by inserting Equation (D.39) - (D.41) into Equation (D.38) and isolating for \dot{T}_r to obtain T_r through integration of \dot{T}_r .

Determination of T_7 :

$$q_6 = q_7 + q_{6,loss} + q_{6,w} \quad (D.42)$$

where

$$q_6 = Q_6 \cdot \rho_w \cdot c_w \cdot T_6 \quad (D.43)$$

$$q_7 = Q_6 \cdot \rho_w \cdot c_w \cdot T_7 \quad (D.44)$$

$$q_{6,loss} = \frac{1}{R_{ra}} \cdot \left(\frac{T_6 + T_7}{2} - T_r \right) \quad (D.45)$$

$$q_{6,w} = c_{p,w} \cdot m_6 \cdot \dot{T}_7 \quad \text{where} \quad m_6 = A_6 \cdot L_6 \cdot \rho_w = \pi \cdot \left(\frac{D_6}{2} \right)^2 \cdot L_6 \cdot \rho_w \quad (D.46)$$

By inserting Equation (D.43) - (D.46) into Equation (D.42), then \dot{T}_7 can be isolated for, and T_7 can be determined through integration of \dot{T}_7 .

Control Volume 7

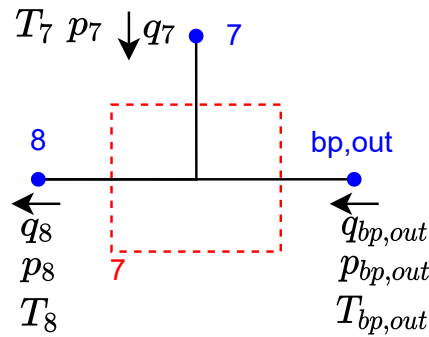


Figure D.8. Control volume 7

Pressure in node 6, 7, and bp, out are identical.

Determination of T_8 :

$$q_7 + q_{bp,out} = q_8 \quad (D.47)$$

where

$$q_7 = Q_6 \cdot \rho_w \cdot c_w \cdot T_7 \quad (D.48)$$

$$q_{bp,out} = Q_{bp} \cdot \rho_w \cdot c_w \cdot T_{bp,out} \quad (D.49)$$

$$q_8 = Q_8 \cdot \rho_w \cdot c_w \cdot T_8 \quad (D.50)$$

Note that $T_{bp,out} = T_5$.

By inserting Equation (D.48) - (D.50) into Equation (D.47), then \dot{T}_8 can be isolated for, and T_8 can be determined through integration of \dot{T}_8 .

Control Volume 8

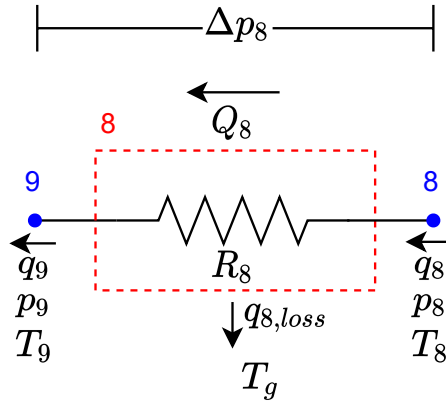


Figure D.9. Control volume 8

Determination of \dot{p}_9 :

$$\dot{p}_9 = \frac{\beta}{\frac{v_8}{2} + \frac{v_{10}}{2}} \cdot (Q_8 - Q_{10} - Q_3) \quad (\text{D.51})$$

where

$$V_{10} = A_{10} \cdot L_{10} = \pi \cdot \left(\frac{d_{10}}{2}\right)^2 \cdot L_{10} \quad (\text{D.52})$$

Determination of \dot{Q}_8 :

$$\dot{Q}_8 = \frac{A_8 \cdot (p_8 - p_9 - \Delta p_8)}{\rho_w \cdot L_8} \quad (\text{D.53})$$

where

$$\Delta p_8 = \lambda \cdot \frac{L_8}{d_8} \cdot \rho_w \cdot \frac{u_8^2}{2} \quad \text{where} \quad u_8 = \frac{Q_8}{A_8} \quad (\text{D.54})$$

λ is given by Equation (D.55)

$$\lambda = 0.3164 \cdot \frac{1}{Re^{\frac{1}{4}}} \quad \text{where} \quad Re = \frac{D_8 \cdot u_8}{\nu} \quad (\text{D.55})$$

Determination of T_9 :

$$q_8 = q_9 + q_{8,loss} + q_{8,w} \quad (\text{D.56})$$

where

$$q_8 = Q_8 \cdot \rho_w \cdot c_w \cdot T_8 \quad (\text{D.57})$$

$$q_9 = Q_8 \cdot \rho_w \cdot c_w \cdot T_9 \quad (\text{D.58})$$

$$q_{8,loss} = \frac{1}{R_8} \cdot \left(\frac{T_8 + T_9}{2} - T_g \right) \quad (\text{D.59})$$

$$q_{8,w} = c_{p,w} \cdot m_8 \cdot \dot{T}_9 \quad \text{where} \quad m_8 = A_8 \cdot L_8 \cdot \rho_w \quad (\text{D.60})$$

By inserting Equation (D.57) - (D.60) into Equation (D.56), then \dot{T}_9 can be isolated for, and T_9 can be determined through integration of \dot{T}_9 .

Control Volume 9

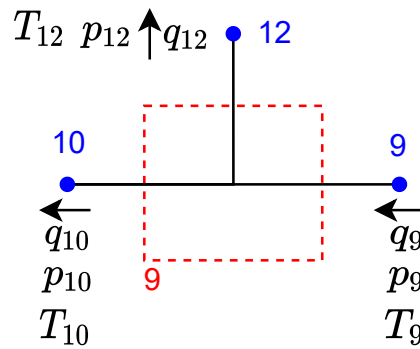


Figure D.10. Control volume 9

The temperature and pressure in node 9, 10, and 12 are identical.

Control Volume 10

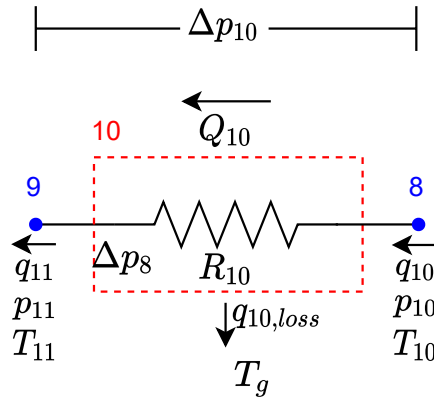


Figure D.11. Control volume 10

Determination of \dot{Q}_{10}

$$\dot{Q}_{10} = \frac{A_{10} \cdot (p_{10} - p_{11} - \Delta p_{10})}{\rho_w \cdot L_{10}} \quad (\text{D.61})$$

where

$$\Delta p_{10} = \lambda \cdot \frac{L_{10}}{d_{10}} \cdot \rho_w \cdot \frac{u_{10}^2}{2} \quad \text{where} \quad u_{10} = \frac{Q_{10}}{A_{10}} = \frac{Q_{10}}{\pi \cdot \left(\frac{d_{10}}{2}\right)^2} \quad (\text{D.62})$$

λ is given by Equation (D.63)

$$\lambda = 0.3164 \cdot \frac{1}{Re^{\frac{1}{4}}} \quad \text{where} \quad Re = \frac{d_{10} \cdot u_{10}}{\nu} \quad (\text{D.63})$$

Determination of T_{11}

$$q_{10} = q_{11} + q_{10,loss} + q_{10,w} \quad (\text{D.64})$$

where

$$q_{10} = Q_{10} \cdot \rho_w \cdot c_w \cdot T_{10} \quad (\text{D.65})$$

$$q_{11} = Q_{10} \cdot \rho_w \cdot c_w \cdot T_{11} \quad (\text{D.66})$$

$$q_{10,loss} = \frac{1}{R_{10}} \cdot \left(\frac{T_{10} + T_{11}}{2} - T_g \right) \quad (\text{D.67})$$

$$q_{10,w} = c_{p,w} \cdot m_{10} \cdot \dot{T}_{11} \quad \text{where} \quad m_{10} = A_{10} \cdot L_{10} \cdot \rho_w \quad (\text{D.68})$$

By inserting Equation (D.65) - (D.68) into Equation (D.64), then \dot{T}_{11} can be isolated for, and T_{11} can be determined through integration of \dot{T}_{11} .

Thermal Resistances

E

In this appendix, the thermal resistances for the pipe sections, used in the model derivation in Chapter 4, are estimated based on assumptions for the pipe isolation material, - type, and - dimensions. Thermal resistances used to determine heat transfer at the consumer are also determined.

Thermal Resistance - Pipes

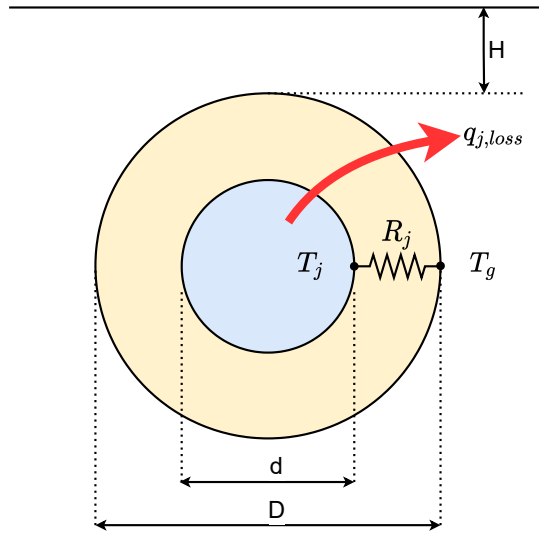


Figure E.1. Pipe cross-section

The heat loss from the water to the surroundings in control volume j is modeled as conduction, given by the formula:

$$q_{j,loss} = \frac{1}{R_j} \cdot (T_j - T_g) = \frac{1}{R_j} \cdot \left(\frac{T_i + T_{i+1}}{2} - T_g \right) \quad (\text{E.1})$$

where the thermal resistance for the pipe in control volume j , R_j , is given by Equation (E.2) [16].

$$R_j = \frac{\ln\left(\frac{D}{d}\right)}{2 \cdot \pi \cdot L_j \cdot k} \quad (\text{E.2})$$

- d - Hydraulic diameter [m]
- D - Diameter of casing [m]
- L_j - Length of control volume j [m]
- k - Thermal conductivity of pipe [W/m · K]
- R_j - Thermal resistance of control volume j [K/W]

A calculator from LOGSTOR [12] is utilized in order to determine the thermal resistance per meter for a given pipe with isolation. The pipe that is used for the calculation has the specifications listed in Table E.1.

Table E.1

Pipe Specification	
Service pipe material	P235GH
Service pipe material type	Welded EN 1021
Insulation type	PUR
Insulation series	Series 1
d	60.03 mm
D	125 mm

Calculation of the thermal resistance is based on a mean grid temperature of 55 °C as it is expected for the grid temperature to vary between 80 °C and 30 °C. Furthermore it is assumed that the pipes are buried 1 m below the surface. The thermal resistance is calculated for a winter day meaning that the ground temperature equals 3.6 °C which is the average ground temperature for January [19], and the surface temperature equals 1.6 °C as this is the average air temperature for January [20].

From the calculator a U value of 0.211 W/m · K is given, which correspond to $U = 1/R$ for one meter. As a result $R_{1m} = 4.7393 \text{K} \cdot \text{m}/\text{W}$. With this value the thermal conductivity for a pipe of one meter can be determined using Equation (E.3).

$$k_{1m} = \frac{\log\left(\frac{D/2}{d/2}\right)}{2 \cdot \pi \cdot R_{1m}} \quad (\text{E.3})$$

For the model, k_{1m} is calculated for two scenarios. In the first one $d = 60.03$ & $D = 125$ and in the second one $d = 88.9$ & $D = 160$. Each k_{1m} value is used when its respective set of diameters are used in the model. The values for k_{1m} are then used to calculate the thermal resistance for the different pipe sections using Equation (E.2).

Thermal Resistance - Consumer House

Two thermal resistances are defined at the consumer. R_{ra} is the first resistance which describes the thermal resistance between the water and the equivalent house

room. R_{wall} is the second resistance which describes the thermal resistance between the equivalent house room and the surrounding air.

A value for each resistance is determined for both the *standard* winter scenario and the *standard* summer scenario. The thermal resistances are found based on the boundary conditions stated in Table G.1.

For each scenario R_{ra} can be determined using Equation E.4.

$$q_{6,loss} = \frac{1}{R_{ra}} \cdot \left(\frac{T_6 + T_7}{2} - T_r \right) \quad (\text{E.4})$$

For the the *standard* summer scenario $R_{ra} = 7.1553 \times 10^{-4}$ K/W, and for the *standard* winter scenario $R_{ra} = 1.1627 \times 10^{-4}$ K/W.

Furthermore for each scenario R_{wall} can be determined using Equation E.5.

$$q_{6,loss} = \frac{1}{R_{wall}} \cdot (T_r - T_{air}) \quad (\text{E.5})$$

For the *standard* summer scenario $R_{wall} = 8.8726 \times 10^{-5}$ K/W, and for the *standard* winter scenario $R_{wall} = 6.5829 \times 10^{-5}$ K/W.

Volume Flow Gradient Derivation

F

The derivation of the volume flow gradient is based on Figure F.1.

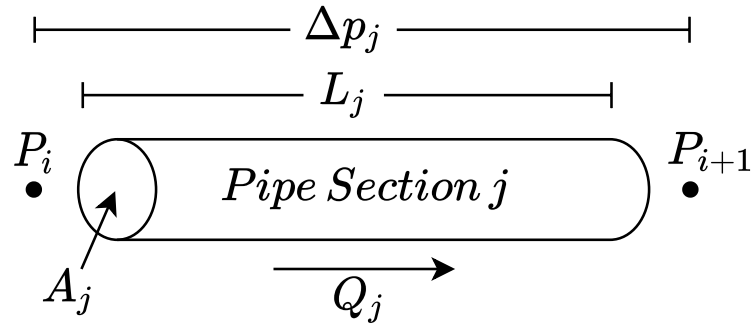


Figure F.1. Pipe Section with constant and variables denoted

Newton's second law for a fluid flowing in a pipe is stated in Equation (F.1).

$$\ddot{x} \cdot m = (p_i - p_{i+1} - \Delta p_j) \cdot A_j \quad (\text{F.1})$$

From Equation (F.1) the acceleration of the fluid can be determined.

$$\ddot{x} = \frac{(p_i - p_{i+1} - \Delta p_j) \cdot A_j}{m} = \frac{(p_i - p_{i+1} - \Delta p_j) \cdot A_j}{L_j \cdot A_j \cdot \rho_w} \quad (\text{F.2})$$

As it is of interest to describe the change in volume flow rather than the change in mass flow each side of Equation (F.2) is multiplied with A_j as shown in Equation (F.3).

$$\ddot{x} \cdot A_j = \frac{(p_i - p_{i+1} - \Delta p_j) \cdot A_j}{L_j \cdot A_j \cdot \rho_w} \cdot A_j \quad (\text{F.3})$$

This results in the final equation which describes the volume flow gradient.

$$\dot{Q}_j = \frac{(p_i - p_{i+1} - \Delta p_j) \cdot A_j}{L_j \cdot \rho_w} \quad (\text{F.4})$$

When the pressure on each side of the pipe section equals the pressure loss across the pipe section the volume flow gradient will be zero.

Test Scenarios Parameter

Choice



Table G.1 shows the parameters used for the two test scenarios. In this appendix an explanation of why these parameter values have been chosen is given.

	Test Scenario 1 "Winter day"	Test Scenario 2 "Summer day"
Parameter Description	Value	Value
Air temperature [T_{air}]	1.6 °C	16.9 °C
Ground temperature [T_g]	3.6 °C	15.1 °C
Room temperature reference [T_{ref}]	20 °C	20 °C
Supply temperature [T_1]	80 °C	70 °C
Supply pressure [p_1]	3.5 bar	3 bar
Return pressure [p_{11}]	1.5 bar	1.5 bar
Consumer inlet temperature [T_6]	65 °C	55 °C
Consumer outlet temperature [T_7]	40 °C	35 °C
Consumer power [$q_{6,loss}$]	279.51 kW	34.94 kW
Fluid velocity [u_4]	1 m/s	0.16 m/s
Bypass flow [f_{bp}]	5%	5%

Table G.1. Boundary conditions for test scenario 1 and 2

Temperatures

The winter day is based on a day in January and the Summer day is based on a day in July. As a result the chosen air - and ground temperature represent the mean air - and ground temperature for January and July respectively. A room temperature of 20 °C is chosen to make sure that heat leaves the consumer regardless of the test scenario. A supply temperature of 80 °C and 70 °C for winter and summer respectively are chosen, as these temperature are reasonable for the given periods. This is the same reason for why the given consumer inlet and - outlet temperatures are chosen.

Pressures

The centrifugal pump that has been utilized in this report is limited to a load pressure of around 2.5 bar. The pressure in the district heating grid spans from

1.5- 6 bar, where 6 bar is the maximum supply pressure and 1.5 bar is the return pressure [21]. Therefore is it deemed reasonable to use the chosen supply - and return pressure.

Fluid Velocity and Consumer Power

For the winter day a fluid velocity of 1 m/s is chosen as this is a reasonable velocity during winter periods [5]. In winter periods the fluid velocity is highest as the consumer power is at its peak level. The consumer power for the winter day is a result of the chosen fluid velocity and inlet/outlet consumer temperature.

Equation (G.2) is used to calculate the consumer power.

$$q_{6,loss} = Q_6 \cdot \rho_w \cdot c_{p,w} \cdot (T_{in} - T_{out}) \quad (G.1)$$

$$= A_4 \cdot u_4 \cdot (1 - f_{bp}) \cdot \rho_w \cdot c_{p,w} \cdot (T_6 - T_7) \quad (G.2)$$

It is reasonable to say that the consumer power for the summer day is an eighth of the winter consumer power [5]. Based on this knowledge the fluid velocity for the summer day can be found by using the respective inlet/outlet consumer temperature and isolating for u_4 in Equation G.2.

Linear Model Validation for the Summer Scenario

H

In Chapter 6 a linear model has been derived and validated by comparing the linear model to the nonlinear model for the *standard* winter day scenario. In this Appendix, the validation is carried out for the *upper worst case* summer day scenario. Figure H.1 shows the dynamic response of the temperature T_4 , volume flow Q_c , and the pressure p_2 when a positive step is given to the pump velocity.

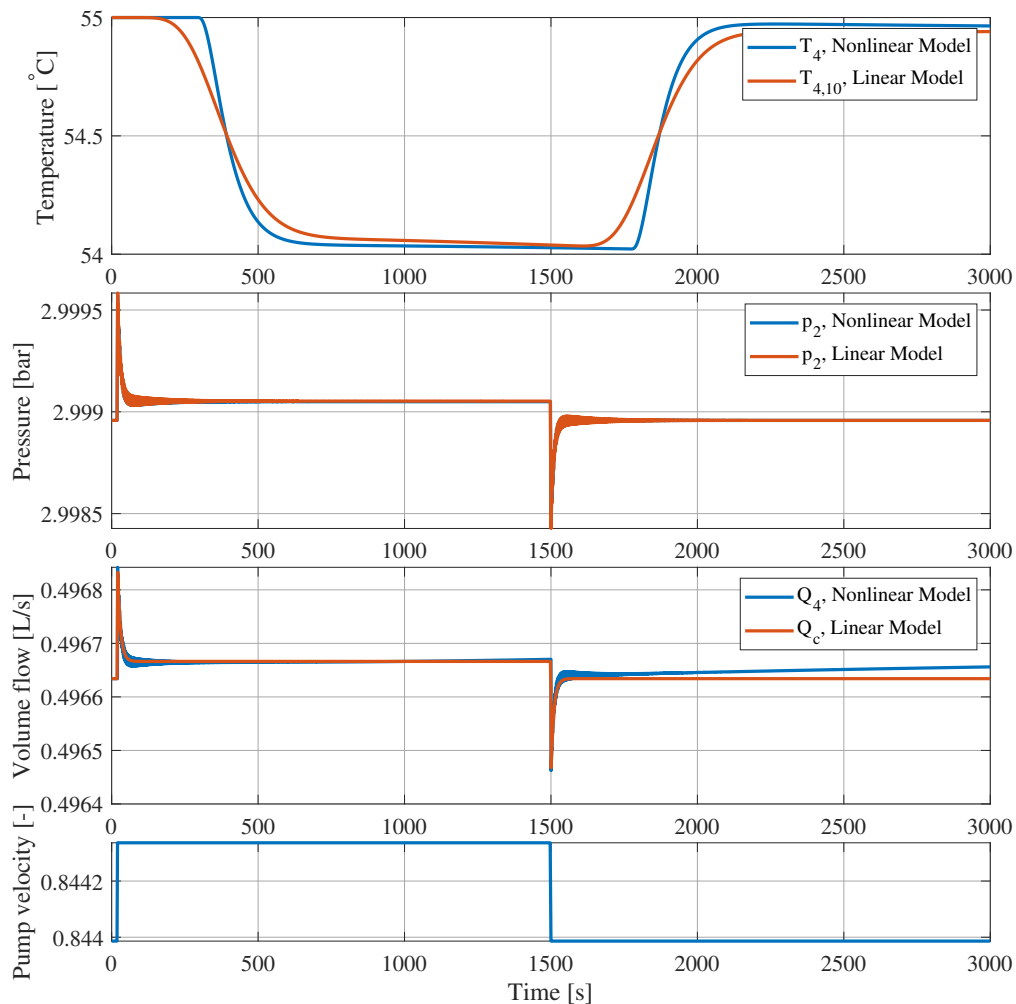


Figure H.1. Comparison of linear - and nonlinear model in the summer scenario

For this comparison, the volume flow and pressure is set to start at the same point, despite the equilibrium point for the nonlinear and simplified linear model differ slightly. There is an offset for the pressure p_2 of 4.32 Pa and an offset of -12.5×10^{-3} L/s for the volume flow Q_c .

From the figure it can be observed that there is some difference in the transient response for the temperature. This is expected and it is caused by the difference in how the transport delay for each model is modelled. For the nonlinear model, an ideal transport delay is utilized in combination with a filter, whereas in the linear model the transport delay is obtained by dividing control volume 2 up into ten minor control volumes. The filter used for the nonlinear model is given in (H.1) and the flow dependent transport delay is given in Equation (H.2).

$$G_{f,summer} = \frac{0.0004}{s^2 + 0.04 \cdot s + 0.0004} \quad (\text{H.1})$$

$$t_{d,summer} = \frac{L_2 \cdot A_2}{Q_4} - t_{tr} \quad (\text{H.2})$$

where $t_{tr} = 100$. The filter, $G_{f,summer}$, and transition time, t_{tr} , are designed such the transition of T_4 in the nonlinear model lies between the response of $T_{4,10}$ in the linear model and the ideal transport delay.

The difference in the way to obtain the transport delay becomes more profound when the volume flow, decreases, and the transport delay as a result increases. Since the linear - and nonlinear model in general show a similar dynamic behaviour, the linear model is deemed acceptable for the further analysis.

Filter Design

I

This appendix include the filter design for the disturbances and noise used in the simulation model.

For this report real measurement data has been collected from a low temperature zone [9]. The raw data includes measurements of p_2 , p_9 , T_2 and T_9 . The mean value has been removed form each signal, to obtain the variations of the states.

I.1 Filters for Simulation Model

As the raw data includes noise from the sensors the data is filtered to obtain a more realistic disturbance signal. To achieve the desired signal a low pass filter is designed. Figure I.1, I.2, I.3 and I.4 show the raw signals and the filtered signals of each state. The designed filters are stated in the figure titles.

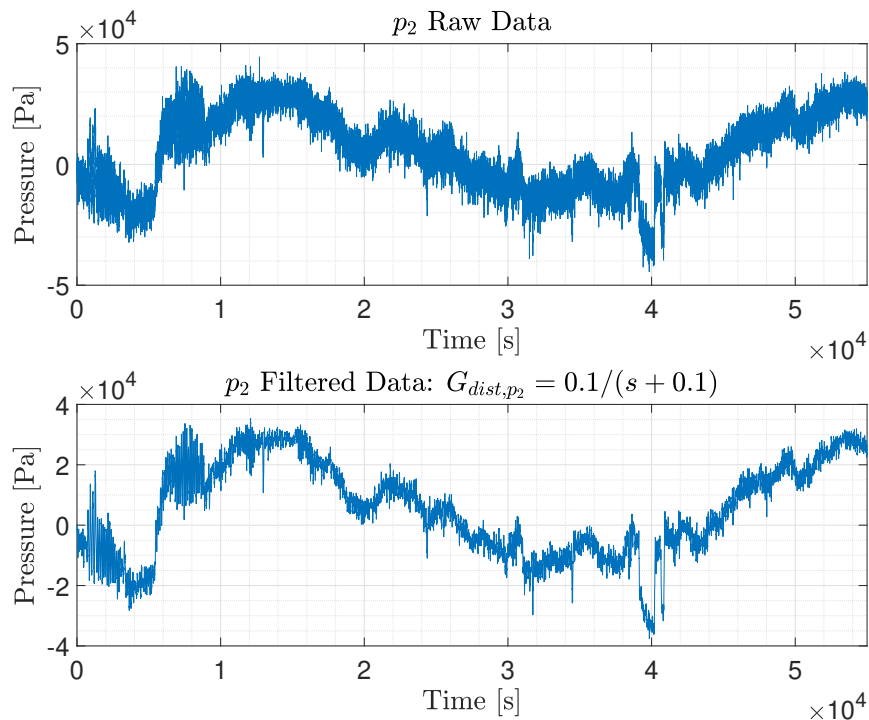
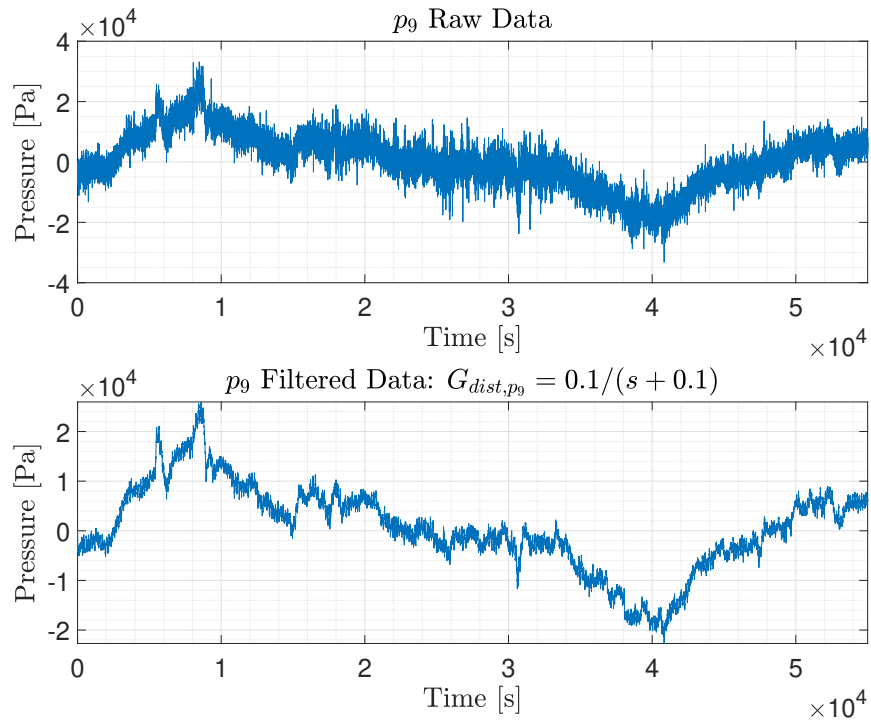
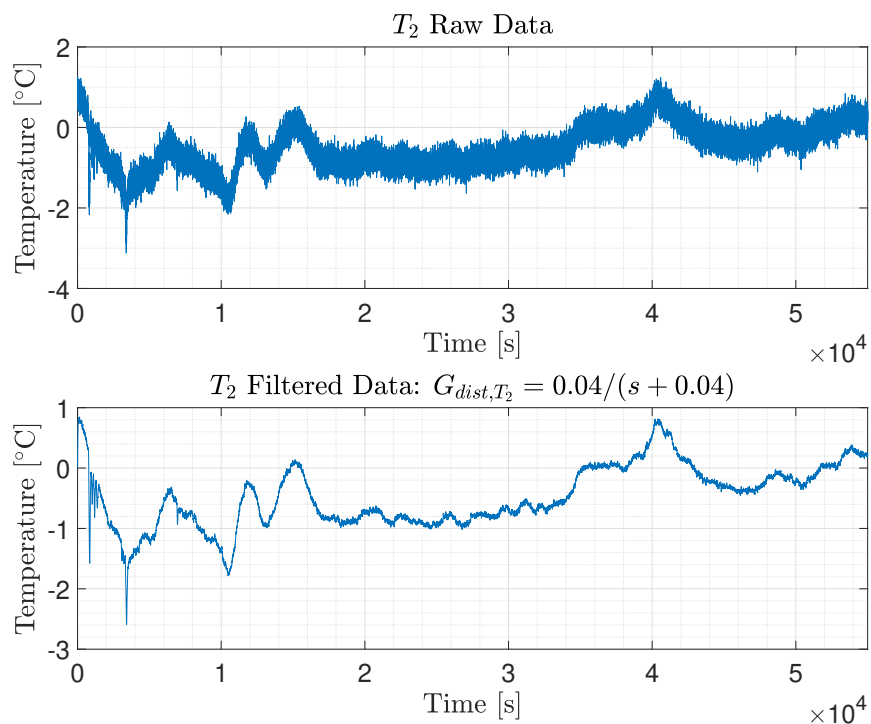


Figure I.1. Raw and filtered p_2 data

Figure I.2. Raw and filtered p_9 dataFigure I.3. Raw and filtered T_2 data

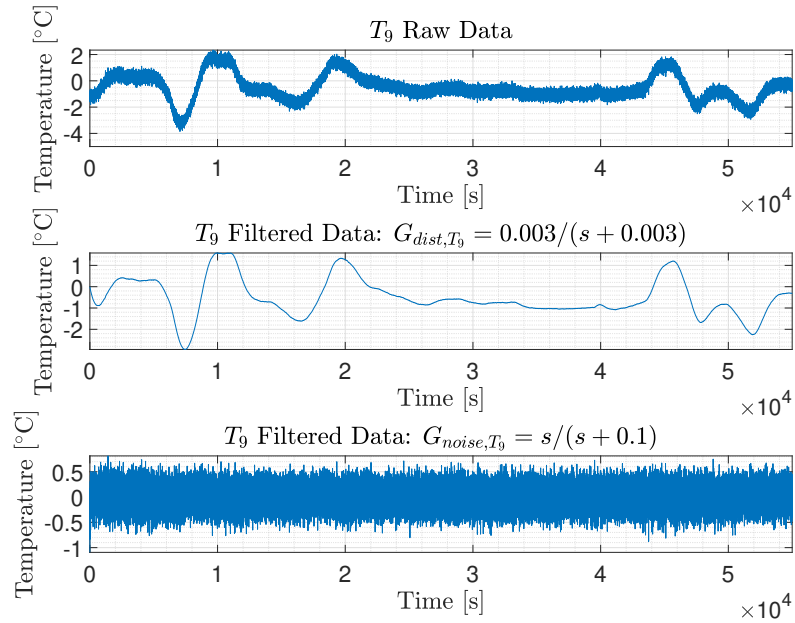


Figure I.4. Raw and filtered T_9 data

To obtain a more realistic T_4 output signal, noise is added based on the sensor noise seen in the data signal of T_9 . Sub Figure 3 in Figure I.4 shows the filter result. As it is not desired to feed back the noisy signal, $T_{4,noise}$ is fed through a low pass filter, G_{LPF} . In Figure I.5 the result of using G_{LPF} to filter $T_{4,noise}$ is visualized.

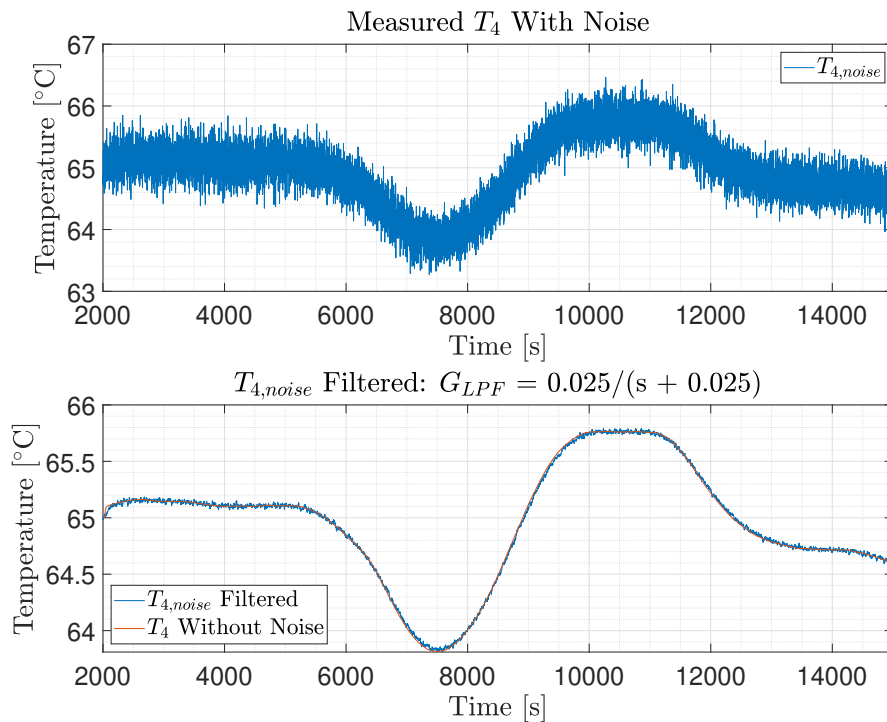


Figure I.5. T_4 with and without noise and $T_{4,noise}$ filtered

Parameter Sensitivity Analysis J

In this appendix, the system's sensitivity to parameter variations is shown to investigate how different variations effect the system dynamic. The analysis is based on the uncertainty model presented in Chapter 8 for the winter scenario, where one parameter is set as an uncertain parameter at a time and varied.

In Figure J.1a, the length of the pipe in control volume 1 and 10 is varied, and from the figure it can be observed that the length primarily impact the system gain. The parameters L_1 and L_{10} have an influence on the inertia of the water and pressure drop across control volume 1 and 10 respectively, and thereby the pressure difference across the shunt pump. In the same manner, the parameter variation of L_4 and L_8 shown in Figure J.1b influence the inertia of the water on the consumer side, which has an impact on the phase at frequencies below 1 rad/s. Variations at faster frequencies are irrelevant for the system. Comparing the two figures, it can be seen that all four length have an impact on the system dynamics at lower frequencies, and the variations will therefore be included in the robustness analysis.

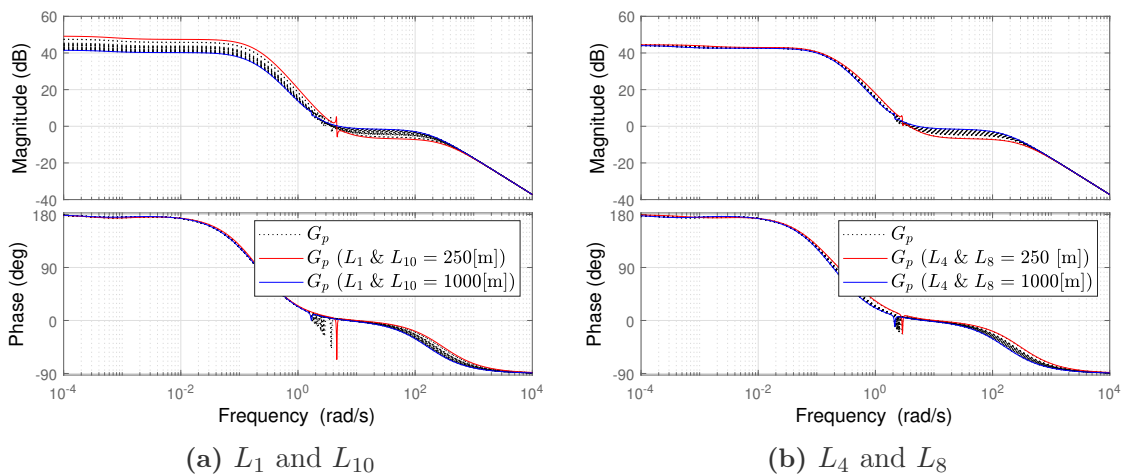


Figure J.1. Parameter variations

The influence of the length for the pipe in control volume 3 and in control volume 6 are shown in Figure J.2b and J.2a respectively. From the figures, it can be concluded that these parameter are not influencing the system dynamics

significantly, and therefore will not be included in the robustness analysis.

Figure J.2c shows how the diameter impact the system, where d is the diameter for control volume 1, 2, 3, 4, 8, 9, and 10. The diameter impact the flow velocity of the fluid, along with the inertia of the fluid and pressure drop in the pipes. From the figure it is clear that the system gain and phase is significantly impacted by the diameter variation, and therefore the diameter will be included in the robustness analysis.

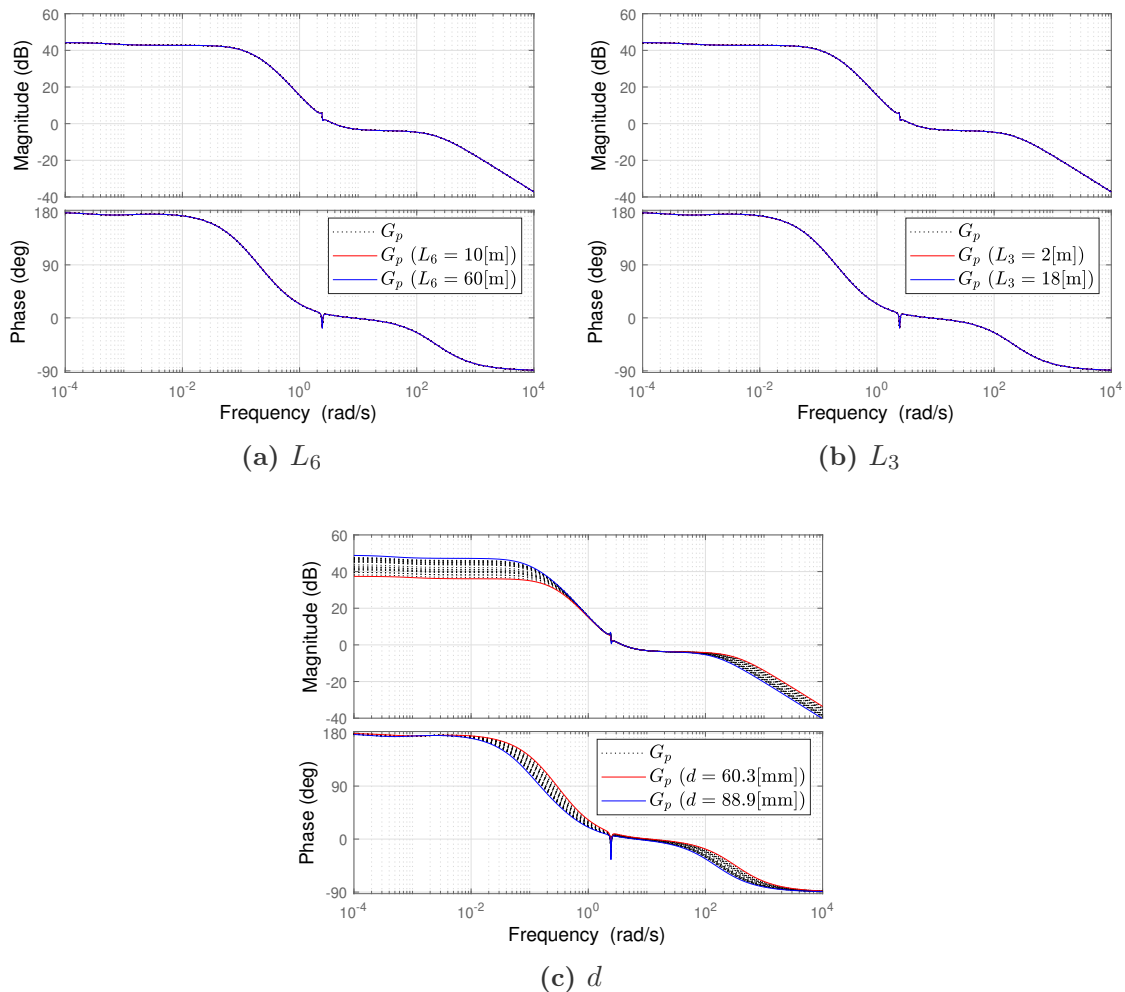


Figure J.2. Parameter variations

J.1 Pressure Influence

Not only do the parameters influence the system dynamics. It has also been observed that the boundary condition for the pressures has an effect on the system dynamics. However, the analysis throughout this report is based on a specific centrifugal pump provided by Grundfos and as shown below this pump can handle a maximum load pressure of approximately 2 bar. This means the analysis in the report is limited to scenarios where the load pressure is below this value. Therefore it is relevant to take into account variations in load pressure before a final control solution is implemented in a real district heating grid.

The volume flow through the shunt pump is approximately 1.08 L/s in the *standard* winter scenario and 0.18 L/s in the *standard* summer scenario. Based on this, the maximum pressure difference across the pump can be calculated, based on a normalized pump velocity of 1. The maximum pressure difference is calculated with Equation (4.23) and (4.24), and is visualized in Figure J.3. In the figure, the maximum pump velocity is used, and the volume flow is swept from 0.0 L/s to 13.5 L/s, to calculate the pressure difference across the pump.

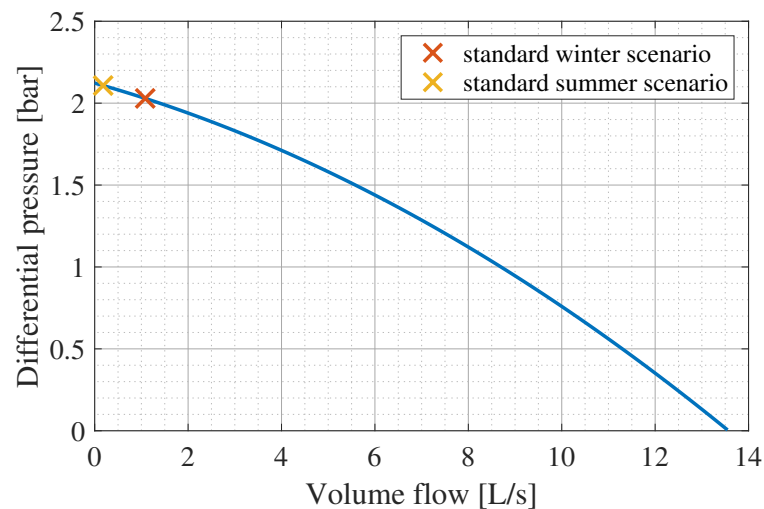


Figure J.3. Pressure characteristics of used pump

Weight Functions K

In this appendix, the designed weight function for $T_{4,10}$ in the summer scenario is showcased along with the expressions for both designed weight functions.

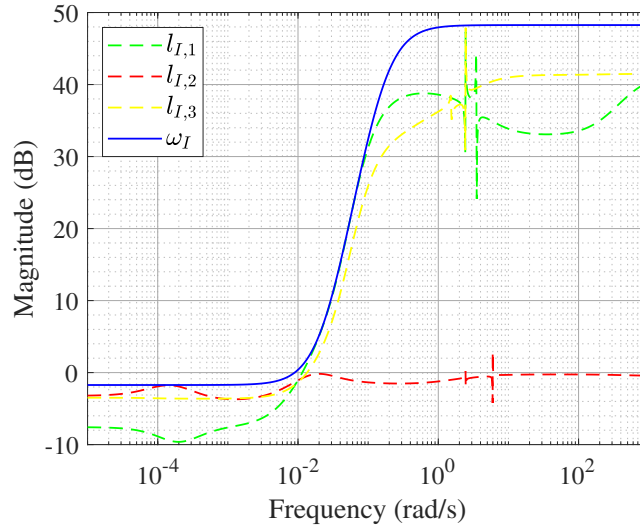


Figure K.1. Weight function for $T_{4,10}$ - A summer day

In Figure K.1 the weight function for $T_{4,10}$ is visualized. Note that the relative uncertainty is only shown for the three specified perturbed plant models. This is due to computational error, where it has not been possible to show the relative uncertainty for the entire set of possible perturbed plants. However, as the weight function is above the relative uncertainty for the three specified perturbed plants, it is assumed that the weight function will be above all possible relative uncertainties.

The weight function for $T_{4,1}$ and $T_{4,10}$ are given in Equation (K.1) and (K.2) respectively.

$$\omega_I = \frac{7.69 \cdot s + 0.82}{0.55 \cdot s + 1} \quad (\text{K.1})$$

$$\omega_I = 0.82 \cdot \left(\frac{s + 2.35 \cdot 10^{-2}}{2.35 \cdot 10^{-2}} \right)^3 \cdot \left(\frac{1.6 \cdot 10^{-1}}{s + 1.6 \cdot 10^{-1}} \right)^3 \quad (\text{K.2})$$

Simulation Result Figures

L

In this appendix the simulation figures which are not shown in Chapter 9 can be found.

Simulation results for SPC scheme 1 for the *standard* winter scenario:

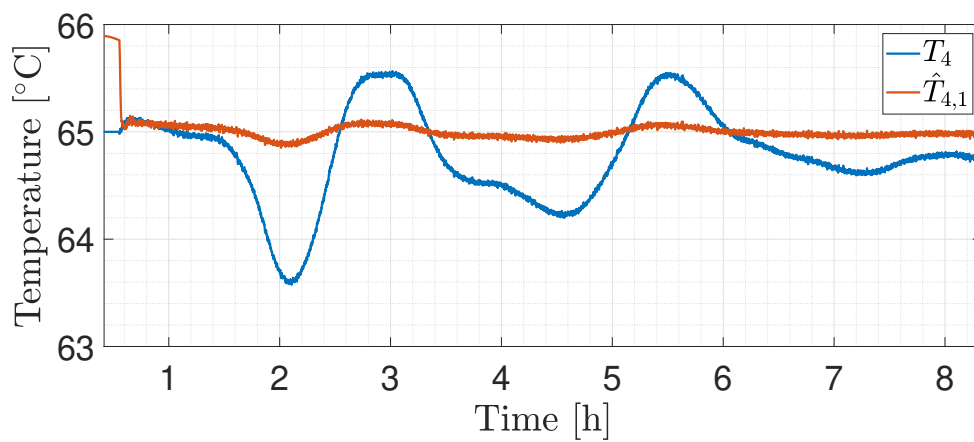


Figure L.1. Scheme 1: Simulation results of T_4 and $\hat{T}_{4,1}$

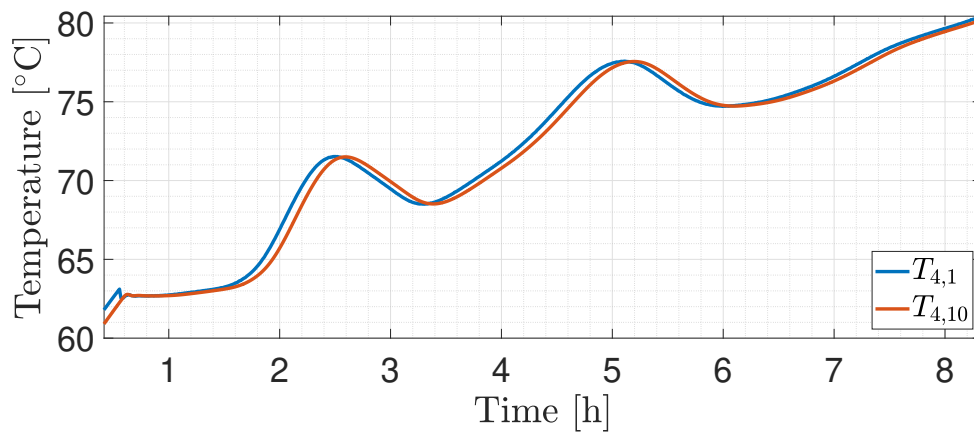


Figure L.2. Scheme 1: Simulation results of $T_{4,1}$ and $T_{4,10}$

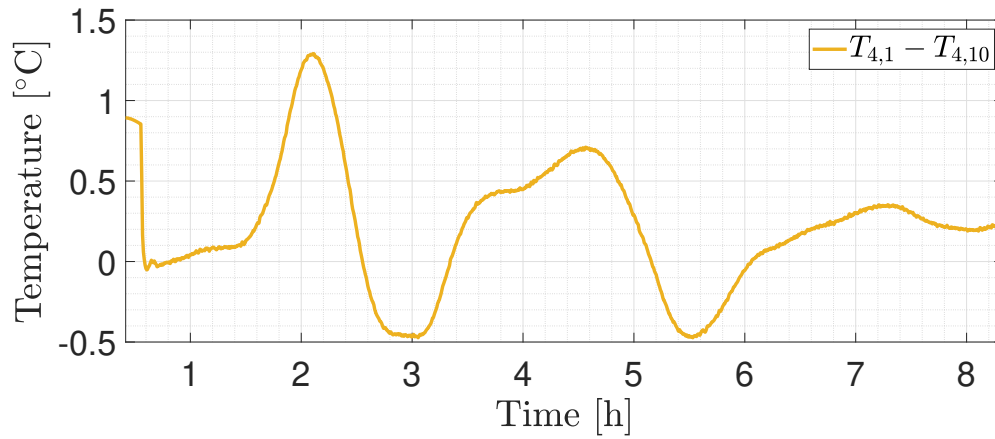


Figure L.3. Scheme 1: Simulation results of $T_{4,1} - T_{4,10}$

Simulation results for SPC scheme 2 for the *standard* winter scenario:

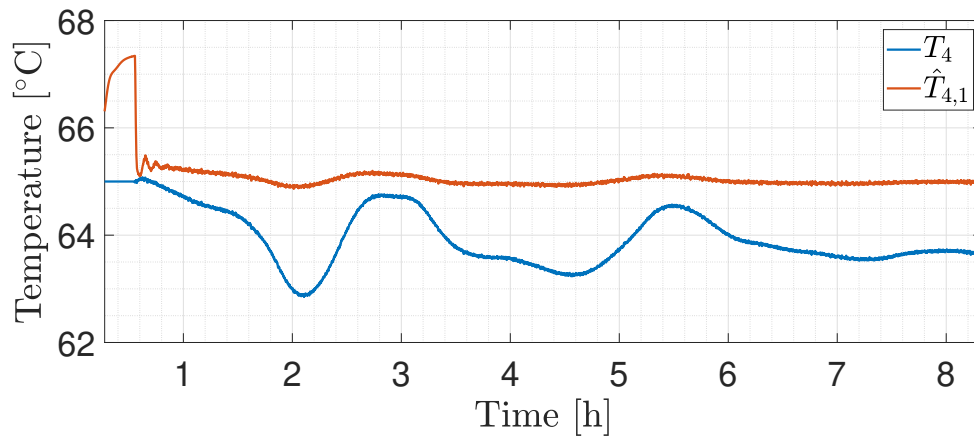


Figure L.4. Scheme 2: Simulation results of T_4 and $\hat{T}_{4,1}$

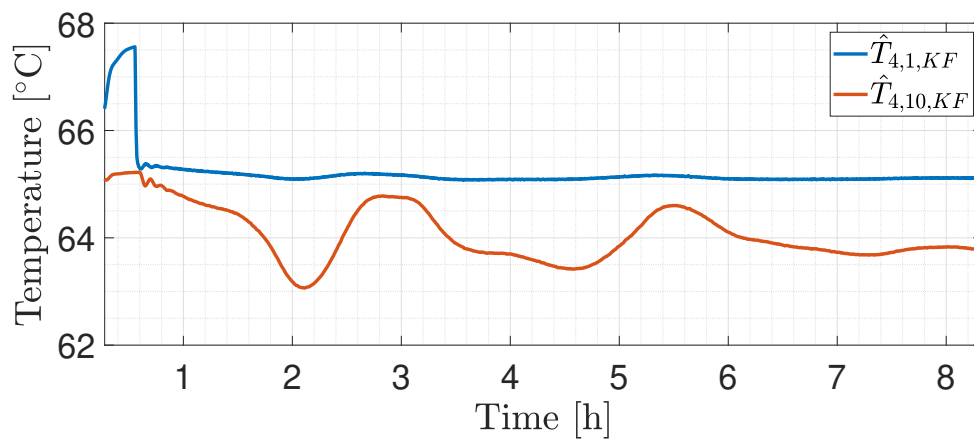


Figure L.5. Scheme 2: Simulation results of $\hat{T}_{4,1,KF}$ and $\hat{T}_{4,10,KF}$

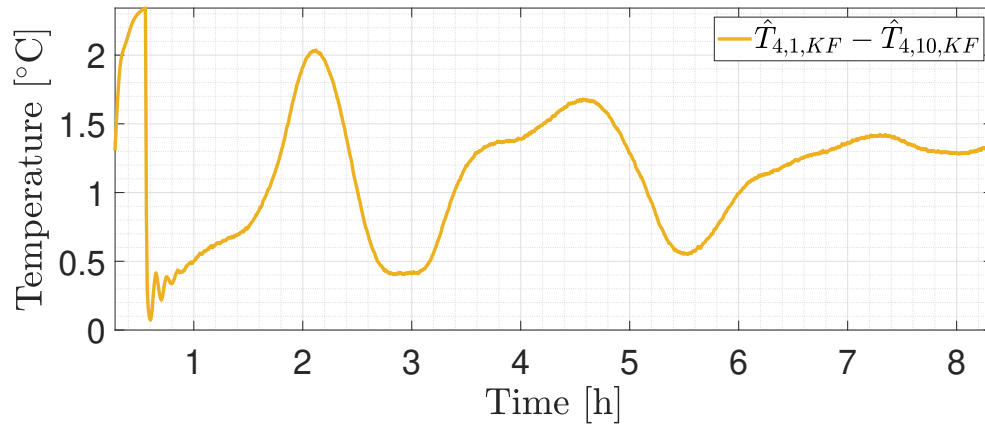


Figure L.6. Scheme 2: Simulation results of $\hat{T}_{4,1,KF} - \hat{T}_{4,10,KF}$

Simulation results for SPC scheme 3 for the *upper worst case* summer scenario:

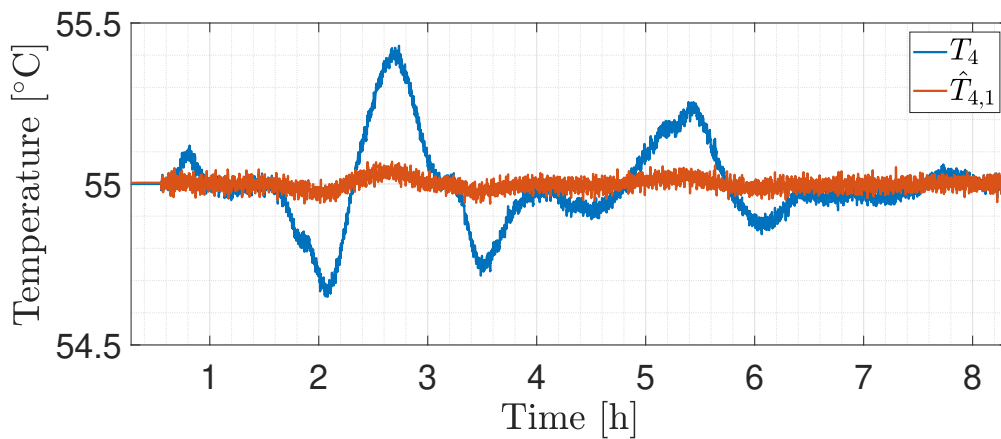


Figure L.7. Scheme 3: Simulation results of T_4 and $\hat{T}_{4,1}$

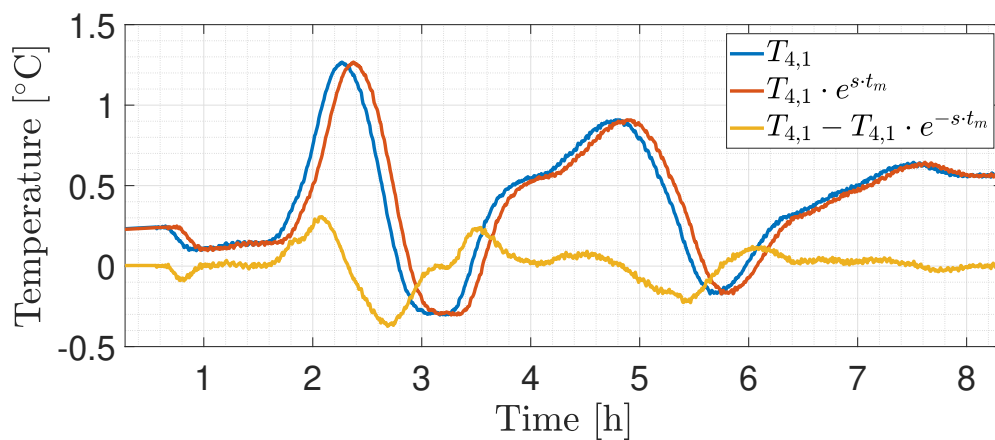


Figure L.8. Scheme 3: Simulation results of $T_{4,1}$, $T_{4,1} \cdot e^{s \cdot t_m}$, and $T_{4,1} - T_{4,1} \cdot e^{s \cdot t_m}$

